DEPARTAMENTO DE INGENIERÍA TÉRMICA Y DE FLUIDOS
Escuela Politécnica Superior

Reduced-Kinetic Mechanisms for Hydrogen and Syngas Combustion Including Autoignition

Autor
Pierre Boivin

Directores de Tesis
Carmen Jiménez Sánchez
Antonio Luis Sánchez Pérez

Leganés, diciembre 2011

À Nicolas

Tesis doctoral

Reduced-Kinetic Mechanisms for Hydrogen and Syngas Combustion Including Autoignition

Autor: Pierre Boivin

Directores de Tesis: Carmen Jiménez Sánchez y Antonio Luis Sánchez Pérez

Firma del Tribunal Calificador:

Firma

Presidente: D. Forman Arthur Williams
Vocal: D. Amable Liñán Martínez
Vocal: D. Paul Clavin
Vocal: Da. Bénédicte Cuenot
Secretario: D. Vadim Kourdioumov
Suplente: D. Pedro Luis García Ybarra
Suplente: D. Eduardo Antonio Fernández Tarrazo

Calificación:

Leganés, 15 de diciembre de 2011

Chaque fois qu'on fait semblant de comprendre,
on perd une occasion d'apprendre ...

Acknowledgements

En primer lugar, me gustaría agradecerle a Carmen su paciencia infinita, y a Antonio su apoyo y confianza incondicional, a los cuales debo el éxito de esta tesis.

I would also like to thank Prof. Forman Williams, whose contribution to this thesis extends to so much more than his role as the president of the defense committee. My three extended summer stays at UCSD were very instructive, and his availability made them very efficient too. In particular I would like to thank him for his quality in being so accessible to young researchers despite his international stature in the field of combustion.

Je voudrais également remercier Antoine et Bénédicte, ainsi que les amis de Toulouse pour leur aide précieuse durant les quatre mois que j'ai pu passer en France.

También quiero darles las gracias a mis compañeros de trabajo, tanto en el Ciemat como en la Universidad Carlos III.

During these three years, I have been given the opportunity to assist and participate in a number of conferences, spend four months in Toulouse, another four in San Diego. This would not have been possible without the funding of the EU, through the MyPlanet FP7 project.

Enfin, je souhaite remercier toute ma famille pour son soutien. La phrase de la page précédente m'a été répétée et rerépétée par mon papa des années durant, éveillant petit à petit une grande curiosité, partie intégrante de mon caractère.

Ma pensée du cœur est sans hésitation pour Nicolas, sans qui je ne serais probablement pas à ce niveau aujourd'hui. Je lui attribue en particulier une partie importante de ma réussite au concours d'entrée à l'École Polytechnique, point de départ de mon éducation supérieure. Tu es parti trop tôt, Nicolas. Cette dissertation t'est dédiée. Merci.

Abstract

Reduced chemical-kinetic mechanisms are investigated for hydrogen and syngas combustion to fill the need for simplified chemistry able to describe with accuracy both premixed and diffusion flames and also autoignition, necessitated for instance in computational work that addresses turbulent combustion or the transition from deflagration to detonation. The reduced descriptions incorporate steady-state assumptions for O and OH, which are found to be reasonably accurate for flames but much less accurate for high-temperature autoignition. A detailed description of ignition histories, both above and below the second explosion limit, provides explicit analytic expressions for the ignition time of hydrogen-air mixtures, valid in a wide range of pressure, temperature, and equivalence ratios, and also leads to a correction for the rates of the reduced chemistry that improves accuracy of predicted high-temperature ignition times while keeping the simplification associated with the steady-state assumptions for O and OH. The resulting reduced mechanisms, which consist of three overall steps for hydrogen combustion and one additional CO-oxidation step for syngas combustion, possess reasonable accuracy for most computational purposes, as is demonstrated through extensive validation exercises including comparisons with detailed-chemistry computations and experimental measurements of flame-propagation velocities, extinction strain rates, and ignition times. The three-step mechanism is used also to investigate a turbulent, supersonic, autoignition-stabilized, hydrogen-air lifted flame, enabling reduced-chemistry capabilities to be tested in a large scale simulation including turbulence modelling.

Resumen

En esta tesis se aborda el desarrollo de mecanismos cinéticos reducidos para la combustión de hydrógeno y gas de síntesis que sean capaces de describir con precisión tanto llamas de premezcla y difusión como procesos de autoignición. Este tipo de mecanismos multipropósito son necesarios, por ejemplo, para cálculos numéricos de combustión turbulenta o de transiciones de deflagración a detonación. En la reducción de la química se hace uso de las hipótesis de estado estacionario para las especies químicas O y OH. Aunque estas aproximaciones son adecuadas para llamas, se observa que no lo son tanto para el caso de la autoignición a temperaturas por encima de la denominada temperatura de cruce. Mediante el estudio analítico de los procesos de autoignición se deducen expresiones explícitas para el tiempo de ignición de mezclas de hidrógeno y aire para un amplio rango de presiones, temperaturas y composiciones, incluyendo condiciones por encima y por debajo de cruce. Además, el estudio proporciona una corrección para las velocidades de reacción de la química reducida que tiene en cuenta la evolución de O y OH fuera del estado estacionario durante la ignición a alta temperatura, mejorando sensiblemente la capacidad predictiva de la química reducida. Los mecanismos resultantes incluyen tres reacciones globales para la combustión de hidrógeno, a las que hay que añadir una reacción adicional de oxidación de monóxido de carbono para la combustión de gas de síntesis. La validación incluye comparaciones extensivas con cálculos numéricos con química detallada y medidas experimentales de velocidades de propagación de llamas, condiciones críticas de extinción aerodinámica de llamas de difusión y tiempos de ignición, dando resultados satisfactorios. El mecanismo global de tres pasos para la combustión de hidrógeno se utiliza también para investigar llamas turbulentas levitadas en una configuración supersónica con autoignición, lo que permite comprobar la capacidad de la química reducida en una simulación numérica a gran escala incluyendo modelado de la turbulencia.

Contents

CHAPTER 1

Introduction

“The study of combustion processes is in a sufficiently early stage so that there is no strong connection between combustion theory and the technology of combustion chamber development. To clarify such a connection is the principal task of workers engaged in establishing combustion as an engineering science.”

F.E. Marble, 1956 [1]

Combustion developed rapidly as an engineering science in the second half of the XXth century. The establishment of the needed mathematical formulation by Theodore Von Kármán and his co-workers was instrumental in addressing key problems in a rigorous manner. Of particular value for the early investigators were the monographs written by G. Millán (Aerothermochemistry, 1958 [2]) and F. A. Williams (Combustion Theory, 1965), the latter followed by a second edition in 1985 [3] that continues to be a reference book for theoretical investigators. Although truly outstanding progress has been made in many areas since Frank Marble’s 1956 statement, much remains to be learnt, with new challenges continuously emerging in connection with novel combustion applications and alternative fuels.

In the beginning, the main objective in designing combustion technologies was to obtain higher power outputs, as needed to meet the ever growing demands associated with faster cars, bigger airplanes, and increasing electricity consumption. The focus has shifted in the past few decades, because aircrafts will not likely be any bigger and there is no need for cars to go any faster. New challenges stem from the increasing number of end-users (e.g., over the last hundred years, the ratio of people per registered motor vehicle in the USA decreased from 19000 to nearly 1.2) and the associated increased emissions, with global warming standing as a prominent issue of great concern. Besides the environmental impact of combustion, with exhaustion of conventional fuels envisioned by the end of this century, efficiency has also become of primary importance, with the power output becoming a secondary objective. These new challenges call for refined combustion devices, based on improved design tools, including advanced numerical modeling.

Hydrogen combustion is the general topic of this dissertation. Although discussions of the utilization of hydrogen for zero-emission vehicles and power production usually revolve around fuel cells, combustion in reciprocating engines and gas turbines is potentially viable at least as cleanly, with water vapor emerging as the main product of oxidation, which proceeds according to the overall reaction $2H_2 + O_2 \rightarrow 2H_2O$. Although not readily available in nature, hydrogen can be obtained by different production methods, and it also appears in significant amounts as a component of syngas and other alternative fuels. Besides, because of its high reactivity, it finds application as an additive to conventional fuels, extending the range of flammable conditions to leaner mixtures, thereby enabling higher thermal efficiency and lower exhaust emissions to be achieved.

Because of the present and future relevance of hydrogen as a fuel and the role that hydrogen chemistry plays in the oxidation of any hydrocarbon, the elementary chemical reactions involved in the oxidation of hydrogen have been investigated in depth for quite some time. The associated detailed scheme, involving eight reactive species and 21 chemical reactions, is reasonably well known [4]. Uncertainties still exist, mainly in connection with reaction-rate constants and chaperon efficiencies of three-body collisions. Despite the relative simplicity of the underlying chemistry, combustion at high Reynolds numbers or in complex configurations excessively taxes computational capabilities even for hydrogen. This motivates the development of systematically reduced hydrogen-oxygen chemistry that has sufficient accuracy to yield reliable computational results, that being the ultimate objective of the work presented in this dissertation.

1.1 Numerical computation of combustion processes

The conservation equations for combustion are the Navier-Stokes equations of mass, momentum and energy supplemented with conservation equations for the N different reactive species present in the mixture, including source terms associated with the chemical reactions [3]. Consequently, for reactive flow computations, the number of differential equations to be integrated is 5+N. In hydrogen combustion, the detailed chemistry is fairly simple and includes only $N = 8$ reactive species, namely, H_2, O_2, H_2O, H, O, OH, HO_2 and H_2O_2, but for heavy hydrocarbons the number of elementary steps can be as high as a few thousand, involving hundreds of chemical species. Even for the simplest fuels, the resulting problem is highly nonlinear, thereby complicating the numerical integration. In the absence of analytic solutions, for many decades progress in understanding combustion relied heavily on theoretical analyses of canonical problems based on asymptotic methods, the only tool of universal applicability, requiring only the existence of a large parameter or coordinate for its foundation [5]. Initially rather limited to the “Russian school” in the 50s to 70s, with scientists as Semenov, Zel’dovich and Frank-Kamenetskii – the last being the author of the steady-state theory of spontaneous combustion, origin of activation-energy asymptotics [6] – the development of analytic methods progressively gained over the European and American schools, first introduced by Von Kármán and Hirshfelder [7–9], and later excelled by scientists like Liñán, Williams or Clavin, who have made over the past forty years extensive contributions to the field of combustion theory [10–14].

Asymptotic analyses increase understanding of the fundamental physical phenomena involved in combustion and often provide useful predictions for quantities of interest, such as ignition times, burning rates or critical conditions for flame extinction. They also serve to guide modeling efforts, needed in the computation of turbulent reactive flows. In most practical applications, the Reynolds number – the ratio of the inertial forces to the viscous forces – in the combustor takes values that may range from 10^6 to 10^9, so that the resulting flow is highly turbulent. Despite the continuous increase in computational power, direct numerical simulations of reactive flows in realistic configurations will not be feasible for many decades to come. As an alternative, large-eddy simulations including modeling of the sub-grid scales currently offer an excellent compromise between accuracy and computational cost, enabling for instance the simulations illustrated in Fig. 1.1 to be performed, which include the unsteady reactive flow in a multi-cycle piston engine [15, 16] and in an annular combustion chamber [17].

The success of the methods developed for turbulence modeling in cold flow simulations has promoted the development of similar closure models in the field of combustion [18]. However, the introduction of combustion brings in many new problems. The disparity between the discrete scales associated with the presence of the flame and the continuous scales of turbulence has important consequences for multi-scale modeling of turbulent combustion [19]. Unlike the small eddies in turbulence, which were shown to have a fairly homogeneous and isotropic behavior [20], providing the basis for turbulence modeling, the small scales introduced by the presence of a flame have no apparent coherence. A common illustration of the strong dependence between small and large scales in combustion is the flame stretch. Many large-scale

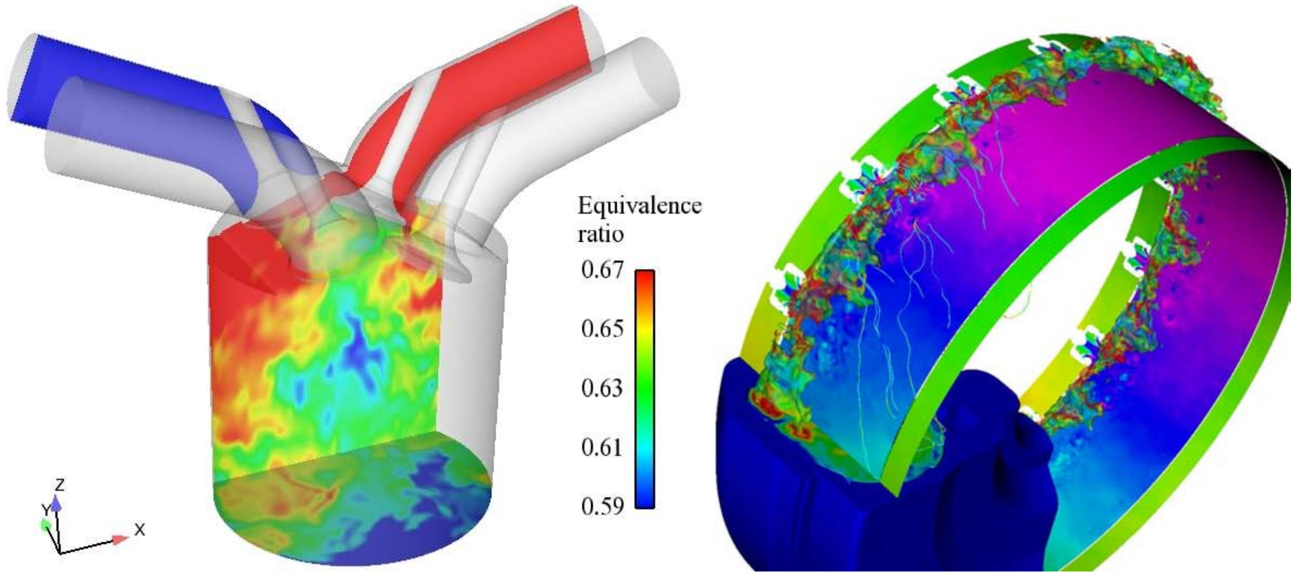

Figure 1.1: Examples of simulations of realistic industrial combustion processes : a piston engine (left), and an annular combustion chamber (right). Courtesy of CERFACS/IFPEN (left), and CERFACS (right).

characteristics of the flame, as its burning rate, propagation velocity or burnt-gas temperature, depend on the area of the flame. However, the flame typically has a very intricate shape, with curvatures which may or may not follow the smallest eddies of turbulence, depending on the regime. These flame scales need to be modeled because they are too small to be resolved at a reasonable cost in most simulations. In addition, the fuel and the oxidizer need to be mixed at the molecular level in combustion, and the mixing usually creates very steep gradients, where local fluctuations are intense. The current limitations in computer power clearly do not allow the use of grid cells sufficiently small to describe the mixing at molecular level, which then needs to be modeled as well.

The contributions of this dissertation to the modeling of reactive flows lie in the chemistry description. The time scales introduced by the kinetics are usually very small compared with those of the flow, especially in the hot zones of the burner. The resolution of these small chemical time scales limits the size of the time step to be employed in the integration and also affects the mesh size required, as time step and grid size are typically intimately bound by a Courant-Friedrichs-Lewy criterion [21]. Clearly, modeling strategies aimed at removing the numerical stiffness associated with these small time scales can be instrumental in enabling more efficient computations to be performed. This motivates the development of reduced chemical-kinetic mechanisms, subject of this dissertation.

1.2 Chemistry reduction: issues and techniques

Chemistry reduction aims at lowering the order of the system of differential conservation equations to be integrated by reducing the effective number of chemical species to be considered in the simulation. The number of species is, indeed, one of the main contributions to the cost of the chemistry integration in a reactive flow simulation. Even in the case of hydrogen oxidation, which consists only of eight reacting species, the potential savings associated with the reduction of the number of species are substantial. A number of additional factors influence the resulting computational costs. For instance, the number of chemical reactions considered also is of importance, because computing each Arrhenius rate has a non-negligible cost, since evaluating its exponential term requires many more CPU cycles than a simple addition or multiplication. The expressions for the rates of the overall chemical reactions of the reduced chemistry, typically more complicated than a simple Arrhenius term, may increase somewhat the associated computational times, so in reducing the chemistry it is important to keep these expressions as simple as possible, avoiding implicit representations. Care should also be exerted in connection with numerical stiffness. Depending on the specific reduction development, the resulting reduced system, although involving a smaller number of equations, may actually be stiffer than the complete one, and therefore less computationally efficient than the original system. It is also important to keep a certain level of simplicity in the model, in order for it to be easily accessible by the user, whether for analytical or numerical work. Facilitating the implementation of the mechanism increases the chances of it being used by the scientific community. Chemistry reduction is all about striking the right compromise, with account taken of the different contributions listed above, in order to obtain the highest level of accuracy for the simplest formulation.

There are a number of strategies for chemistry reduction, each one responding differently to the challenges listed above. Tabulated chemistry [22–24], for instance, consists of storing the chemical source terms in tables to avoid repeated calculations. There are numerous variants; some require computations prior to the simulation for the conditions expected to be encountered, while others evaluate chemical terms in run time. Common to all tabulated chemistry techniques is the need for a very optimized algorithm for storing and searching data in the table in order to be efficient.

An alternative reduction strategy stems from identifying automatically the fast and slow time scales of the chemical system in order to decouple them. Fast time scales in chemistry are typically much smaller than the transport time scales. It is then possible to avoid having to compute them, thus reducing the order of the system by the number of fast-time scales in the species conservation equations. This idea is the fundament of methods such as the Intrinsic Low-Dimensional Manifolds, published in 1992 [25], and the Computational Singular Perturbation (CSP), which appeared two years later [26]. Another recent method, the Rate-Controlled Constrained-Equilibrium [27], completes the reduction with a more accurate description of the chemical source term in the energy conservation equation.

The methods cited so far were developed specifically for use in numerical simulations. Their success relies on the fact that they are not fuel-specific, and the degree of reduction required is entered as a parameter, enabling the automatic reduction of the chemistry for complex fuels to be performed, including hundreds of species. However, the implementation of these methods is complex, and is to be done at the root of the solver, hindering implementation in commercial codes. Although they can be quite effective, their automatic character obscures physical understanding of the chemical interactions occurring in the flow field and make them unsuited for analytic studies. For these reasons, analytic methods for chemistry reduction employing rigorous approximations based on time disparities, such as the partial equilibrium assumption for fast chemical reactions or the quasi-steady-state approximation for intermediates [3], are more appropriate for many purposes, in particular when the starting detailed fuel chemistry is of moderate size, as occurs in the case of hydrogen, leading to reduced descriptions with a small number of overall reactions that can be readily implemented in existing numerical codes.

1.3 The quasi-steady-state approximation

The quasi-steady-state approximation, to be used below in reducing the hydrogen oxidation chemistry, is a simplification that applies to the description of reaction intermediaries when their effective production and consumption times are much smaller than the corresponding accumulation and transport times (by convection or diffusion). Under those conditions, the accumulation, convection and diffusion terms in the corresponding conservation equation are much smaller than the chemical terms, and can be neglected in the first approximation, thereby reducing the governing equation of the steady-state radical to a balance between chemical production and consumption. This algebraic equation replaces the corresponding differential equation in the flow-field description, thereby reducing by one the order of the system of differential equations to be integrated. In many instances, the chemical balance can be solved explicitly for the concentration of the steady-state species.

The term "quasi-steady-state" was coined in the original developments, dealing with transportless homogeneous systems, for which the approximation amounts to neglecting the time variation of the given intermediate species. To illustrate the approximation, it is of interest to consider a simple chemical system consisting of two elementary unimolecular reactions

$$\mathrm{A} \overset{1}{\to} \mathrm{B} \overset{2}{\to} \mathrm{C}, \tag{1.1}$$

where A is the reactant, B the intermediary species, and C the product. With C_i denoting the concentration of species i and k_j being the reaction-rate constant of reaction j, so that for instance $k_1 C_\mathrm{A}$ is the rate of reaction 1, the corresponding system of homogeneous balance equations can be written as

$$\frac{\mathrm{d}C_\mathrm{A}}{\mathrm{d}t} = -k_1 C_\mathrm{A}, \qquad \frac{\mathrm{d}C_\mathrm{B}}{\mathrm{d}t} = k_1 C_\mathrm{A} - k_2 C_\mathrm{B}, \quad \text{and} \quad \frac{\mathrm{d}C_\mathrm{C}}{\mathrm{d}t} = k_2 C_\mathrm{B}, \tag{1.2}$$

to be integrated with initial conditions $C_\mathrm{A} - C_0 = C_\mathrm{B} = C_\mathrm{C} = 0$ at $t = 0$.

For the unimolecular reactions considered, the reciprocal of the reaction-rate constants have dimensions of time. As can be seen in the first equation of (1.2), k_1^{-1} represents the characteristic time for reactant consumption, that is, the characteristic time required for the reactant concentration to decrease by an amount of the order of its initial value. The steady-state approximation for the intermediate B arises when the reaction-rate constant k_2 is much larger than k_1. To see this, note that at times of order k_1^{-1}, a simple order of magnitude analysis in the second equation of (1.2) yields $C_\mathrm{B}^*/(k_1^{-1})$, $C_0/(k_1^{-1})$, and $C_\mathrm{B}^*/(k_2^{-1})$ for the accumulation, production and consumption rates of the intermediate B, with C_B^* representing its unknown characteristic concentration. Clearly, if $k_2 \gg k_1$ the accumulation rate becomes negligibly small compared with the consumption rate, and can be neglected in the first approximation, so that the corresponding equation for the evolution of C_B reduces to $k_1 C_\mathrm{A} - k_2 C_\mathrm{B} = 0$. The physical interpretation is that in the limit $k_2 \gg k_1$, the consumption rate of B is so rapid that this intermediate is consumed as soon as it is created, without significant accumulation, thereby resulting in a small quasi-steady-state concentration

$$C_\mathrm{B} = \frac{k_1}{k_2} C_\mathrm{A} \tag{1.3}$$

changing slowly with time as the reactant is consumed. Note that $C_\mathrm{B} \ll C_\mathrm{A}$ because $k_1 \ll k_2$, indicating that intermediates in steady state appear in concentrations that are much smaller than those of the reactants. This characteristic is often used in realistic computations to identify radicals in steady state.

The solution for $k_2 \gg k_1$ therefore reduces to the integration of

$$\frac{dC_\mathrm{A}}{dt} = -k_1 C_\mathrm{A} \qquad \text{and} \qquad \frac{dC_\mathrm{C}}{dt} = k_1 C_\mathrm{A}, \tag{1.4}$$

where the second equation is obtained by substituting the steady-state expression (1.3) into the third equation of (1.2). The reduced problem (1.4) can be interpreted as the result of the equivalent chemical-kinetic scheme

$$\mathrm{A} \overset{k_1}{\to} \mathrm{B} \overset{k_2}{\to} \mathrm{C} \qquad \Longleftrightarrow \qquad \mathrm{A} \overset{k_1}{\to} \mathrm{C}, \tag{1.5}$$

indicating that in the limit $k_2 \gg k_1$ the system of two elementary reactions is replaced by a single overall "apparent" reaction A → C with a rate equal to $k_1 C_\mathrm{A}$.

Integration of (1.4) with initial conditions $C_\mathrm{A} - C_0 = C_\mathrm{C} = 0$ at $t = 0$ yields

$$C_\mathrm{A} = C_0 e^{-k_1 t}, \qquad C_\mathrm{C} = C_0(1 - e^{-k_1 t}). \tag{1.6}$$

The reader can check that (1.3) and (1.6) represent the limiting form of the exact solution of the complete problem

$$\begin{aligned} C_\mathrm{A} &= C_0 e^{-k_1 t} \\ C_\mathrm{B} &= C_0 \frac{k_1}{k_2 - k_1}(e^{-k_1 t} - e^{-k_2 t}) \\ C_\mathrm{C} &= C_0\Big(1 + \frac{k_1 e^{-k_2 t} - k_2 e^{-k_1 t}}{k_2 - k_1}\Big) \end{aligned} \tag{1.7}$$

in the limit $k_2 \gg k_1$ for $t \gg k_2^{-1}$, whereas for small times $t \sim k_2^{-1}$ the steady-state solution for C_B does not represent accurately that given in (1.7). This type of departures are also typically found in analyses of realistic chemical systems, for which the steady-state approximation for chain carriers is often inaccurate in the initial or final stages of a chain reaction [3], during which chain carriers are being produced or destroyed relatively rapidly through the predominance of initiation or termination steps. However, the rates of propagation steps often exceed those of initiation and termination so greatly during the major part of straight-chain reactions that the steady-state approximation is quite accurate for most of the reaction history (i.e., for $t \sim k_1^{-1}$ in the simple example analyzed above).

The analysis of realistic chemical kinetic schemes is in general significantly more complicated than that presented in this illustrative example, because there are many possible reaction paths, depending on the local conditions of composition and temperature. The expressions for the concentrations of the steady-state species become more complex than (1.3), and oftentimes cannot be expressed in closed explicit form, so that truncation is needed to provide additional simplification prior to implementation of the reduced kinetics.

1.4 Reduced chemical-kinetic mechanisms for hydrogen combustion

Reduced descriptions based on steady-state approximations are easier to develop for hydrogen-oxygen chemistry than for the oxidation of other fuels because fewer species and fewer elementary steps are involved for hydrogen. A number of systematic reductions of hydrogen-oxygen mechanisms have been derived in the past, each being restricted to one particular combustion process. There are, for example, separate reductions for autoignition [28] and for laminar deflagration [11, 29]. A one-step overall mechanism, systematically derived for sufficiently lean deflagrations, is accurate for many purposes [30, 31], including description of flame-ball structures and flammability limits [32, 33]. Reductions for laminar diffusion flames [34, 35] are much more similar to those for deflagrations than to those for autoignition, although even the reductions for these flames exhibit differences in detail. Reduced chemistry for detonations, on the other hand, would resemble that for autoignition more closely than that for flames, because the solution in the induction zone right behind the shock is essentially determined by a high-temperature branched-chain explosion.

What is needed for general computational approaches is sufficiently accurate reduced chemistry that encompasses all of these combustion processes because it is not known in advance, at the start of a calculation, in exactly what manner the combustion will develop. The purpose of the present dissertation is to derive a systematically reduced description of hydrogen-oxygen chemistry that can be applied to all of these combustion processes with acceptable accuracy.

1.5 Outline of the dissertation

The systematic reduction of the hydrogen-air chemistry is presented in Chapter 2. After introducing the detailed scheme of 21 steps and 8 reactive species that describes hydrogen combustion, the reduction starts by identifying the minimum subset of elementary reactions necessary for the description of ignition, deflagrations, nonpremixed flames and detonations, ensuring minimal loss of accuracy. The short mechanism of twelve steps that is identified may be used for computations [36], but does not reduce the number of conservation equations to be integrated, as the order of the system is identical to that of the 21-step detailed chemistry, involving also 8 reacting species. However, it is used as a basis for the chemistry reduction, derived next by introduction of steady-state approximations for the intermediary species O, OH, HO_2 and H_2O_2. The resulting reduced mechanism, consisting of two overall reactions between four reacting species (H_2, O_2, H_2O and H), is found to describe accurately premixed and non-premixed flames for a wide range of temperature and pressure conditions, extending previous works [30, 31] to high pressure conditions, of interest in gas turbine applications.

In hydrogen-air ignition, the slow initiation reaction

$$H_2 + O_2 \quad \rightarrow \quad HO_2 + H$$

is responsible for the generation of the first radicals, necessary to promote hydrogen oxidation. The H atoms can be consumed by the chain-branching elementary reaction

$$O_2 + H \quad \rightarrow \quad OH + O$$

or by the third-body elementary reaction

$$H + O_2 + M \quad \rightarrow \quad HO_2 + M,$$

in proportions that depend on the existing initial temperature and pressure. The competition between these two regimes is characterized by the so-called *crossover temperature* that defines the *2^{nd} explosion limit* of hydrogen-oxygen combustion [3]. Above crossover, chain branching becomes dominant, leading to rapid ignition events, which are investigated in Chapter 3 as part of the reduced-kinetics development. It is seen that the two-step mechanism derived previously for flame computations is inaccurate for ignition, in that it yields significant underpredictions of ignition times that become larger as the mixture becomes leaner. A first modification to the reduced kinetics, guided by previous investigations [37], involves taking HO_2 out of steady state, leading to a three-step reduced mechanism that improves somewhat predictive capabilities, but not to a satisfactory point. A study of the chain-branching explosion involving the time evolution of the radicals H, O and OH is then undertaken, leading to a correction for the rates of the three-step reduced mechanism that improves considerably predictions of autoignition times, even in fuel-lean conditions, by accounting in an approximate way for the identified failure of the O and OH steady-state approximations. The correction is then validated in different high-temperature autoignition configurations, including computations of homogeneous combustion, time-dependent mixing-layer ignition and structures of steady detonations.

The purpose of Chapter 4 is twofold. The first objective is to extend the validation exercises of the three-step chemistry by addressing turbulent autoignition. To this end, a supersonic lifted co-flowing hydrogen-air diffusion flame stabilized by autoignition is to be investigated. We shall see that the three-step mechanism successfully reproduces this challenging test case, involving autoignition, diffusion and premixed combustion regions under intensely fluctuating flow conditions.

Systematic post-processing of such unsteady three-dimensional lifted flame simulations to analyze flame stabilization is quite a challenging endeavor [38–43] because the instantaneous stabilization position typically fluctuates rapidly. While the Takeno flame index, introduced fifteen years ago [41], is widely employed in numerical computations of reactive turbulent flows to identify premixed and non-premixed combustion, identification of autoignition remains nowadays an active research subject [38], as the role of autoignition in flame stabilization is still uncertain [40]. The ability to identify in a systematic manner zones where autoignition originates is a crucial issue, to be addressed as the second objective of this chapter. A new explicit diagnostic procedure is proposed at the end of Chapter 4 as a means to identify regions where high-temperature autoignition is occurring, based on the joint use of quantities inspired by those introduced in Chapter 3 [38, 42]. The diagnostic procedure is fully explicit, which makes it computationally cheap and easily accessible both at the post-processing stage and in run time.

The development of IGCC technologies, involving gas-turbine combustion of syngas, derived for instance by air or O_2 gasification of pulverized coal, has recently promoted interest in studies of CO/H_2 combustion. Chapter 5 is an extension of Chapters 2 and 3, in which, by the addition of a fourth step accounting for the chemistry of CO to the three-step reduced chemistry of Chapter 3, a reduced mechanism is derived for computation of syngas combustion over a wide range of conditions that include, in particular, those typical of gas-turbine operation. The resulting four-step mechanism is validated through comparisons with experimental data of autoignition times and burning rates, giving very good agreement for most conditions of practical interest.

Chapter 6 addresses again autoignition events, extending the work of Chapter 3 to investigate the slow ignition events occurring for conditions below crossover, of relevance for instance in the operation of lean-premixed hydrogen gas turbines, where autoignition in the premixers upstream from the combustion chamber is an unwanted phenomenon to be avoided. The radicals O, OH and H are all seen to follow in this case a good steady state, thereby leading to a three-step mechanism that is further reduced by also introducing a steady-state assumption for HO_2, an excellent approximation at low temperatures. The resulting two-step mechanism is used for the theoretical analysis of the homogeneous ignition problem. It is shown that the two overall reaction rates possess very large effective activation energies that can be used to simplify the analytical treatment, yielding an explicit expression for the ignition time that is seen to provide excellent accuracy.

The reduced-chemistry results obtained in Chapters 2, 3, and 6 are revisited in Chapter 7, which explores the feasibility of multipurpose reduced chemistries able to describe with sufficient accuracy premixed and nonpremixed flames, detonations, high-temperature autoignition, and also low-temperature autoignition. A four-step mechanism with O and OH in steady state is thoroughly tested to give satisfactory results under all conditions. Utilization of a single radical representing either HO_2 for high-temperature ignition or H_2O_2 for low-temperature ignition is investigated with the objective of reducing further the number of relevant chemical species to be described. Integrations show promising results for different laminar test cases, although computations in turbulent environments are still needed for full validation.

The dissertation ends in Chapter 8 with a final summary of conclusions, along with a short account of problems that we believe should be investigated in the future.

CHAPTER 2

Chemistry descriptions for hydrogen-air combustion

This chapter presents an overview of chemistry descriptions for hydrogen combustion. After introducing the complete set of 21 elementary reactions of the detailed mechanism, it will be shown that a subset of twelve reactions suffices to describe combustion under all conditions of practical interest. Next, the chemistry will be further simplified through introduction of steady-state assumptions for intermediates, and the resulting reduced description will be tested under different combustion conditions. In particular, it will be shown that a two-step reduced mechanism with H as the only radical out of steady state is sufficiently accurate for describing premixed and nonpremixed flames. The corresponding overall rates are implicit and require in principle an iterative solution procedure, although a sufficiently accurate direct evaluation methodology is proposed. Although the two-step mechanism is sufficiently accurate for flame descriptions, consideration of HO_2 out of steady state will be seen in the following chapter to be essential for describing autoignition.

2.1 Detailed chemical-kinetic mechanism for hydrogen combustion

Among the various detailed mechanisms that are available, the following development will make use of the so-called San Diego mechanism [4], for describing hydrogen combustion. This mechanism has been tested recently and for most conditions was shown to give excellent predictions for laminar flame burning velocities, induction time, oxidizer stream temperature at autoignition and strain rate at extinction (see http://maeweb.ucsd.edu/∼combustion/cermech/hydrogen/). It consists of 21 reversible elementary reactions, involving 8 reacting species H_2, O_2, H_2O, H, O, OH, HO_2 and H_2O_2, listed in Tab. 2.1. The table contains, for each elementary reaction, the activation energy E and the constant A and temperature exponent n of the preexponential factor necessary to compute its reaction-rate constant

$$k = AT^n \exp(-E/R^oT), \tag{2.1}$$

where $R^o \simeq 8.314$ J K^{-1} mol^{-1} is the ideal gas constant and T is the temperature in Kelvin.

Note that, from a global-reaction viewpoint, the hydrogen oxidation chemistry is no more than a six-step mechanism, there being two atom (or element) conservation equations for the eight chemical species. In other words, although there are many more elementary chemical-kinetic reactions, there are only six independent differential equations for species conservation with nonzero chemical source terms. Various mechanisms that are reduced to fewer than six steps have been proposed and tested in the literature. The simplification follows in general from introducing steady-state assumptions for intermediates after shortening the chemical scheme by discarding those elementary reactions that contribute negligibly to the combustion process, a procedure to be followed below.

Reaction		A^{a}	n	E^{a}
$\mathrm{H + O_2 \rightleftharpoons OH + O}$		3.52×10^{16}	-0.7	71.42
$\mathrm{H_2 + O \rightleftharpoons OH + H}$		5.06×10^{4}	2.67	26.32
$\mathrm{H_2 + OH \rightleftharpoons H_2O + H}$		1.17×10^{9}	1.3	15.21
$\mathrm{H_2O + O \rightleftharpoons 2OH}$		7.06×10^{0}	3.84	53.47
$\mathrm{2H + M \rightleftharpoons H_2 + M^{b}}$		1.30×10^{18}	-1.0	0.0
$\mathrm{H + OH + M \rightleftharpoons H_2O + M^{b}}$		4.00×10^{22}	-2.0	0.0
$\mathrm{2O + M \rightleftharpoons O_2 + M^{b}}$		6.17×10^{15}	-0.5	0.0
$\mathrm{H + O + M \rightleftharpoons OH + M^{b}}$		4.71×10^{18}	-1.0	0.0
$\mathrm{O + OH + M \rightleftharpoons HO_2 + M^{b}}$		8.30×10^{14}	0.0	0.0
$\mathrm{H + O_2 + M \rightleftharpoons HO_2 + M^{c}}$	k_0	5.75×10^{19}	-1.4	0.0
	k_∞	4.65×10^{12}	0.44	0.0
$\mathrm{HO_2 + H \rightleftharpoons 2OH}$		7.08×10^{13}	0.0	1.23
$\mathrm{HO_2 + H \rightleftharpoons H_2 + O_2}$		1.66×10^{13}	0.0	3.44
$\mathrm{HO_2 + H \rightleftharpoons H_2O + O}$		3.10×10^{13}	0.0	7.20
$\mathrm{HO_2 + O \rightleftharpoons OH + O_2}$		2.00×10^{13}	0.0	0.0
$\mathrm{HO_2 + OH \rightleftharpoons H_2O + O_2}$		2.89×10^{13}	0.0	−2.08
$\mathrm{2OH + M \rightleftharpoons H_2O_2 + M^{d}}$	k_0	2.30×10^{18}	-0.9	−7.12
	k_∞	7.40×10^{13}	-0.37	0.0
$\mathrm{2HO_2 \rightleftharpoons H_2O_2 + O_2}$		3.02×10^{12}	0.0	5.8
$\mathrm{H_2O_2 + H \rightleftharpoons HO_2 + H_2}$		4.79×10^{13}	0.0	33.3
$\mathrm{H_2O_2 + H \rightleftharpoons H_2O + OH}$		1.00×10^{13}	0.0	15.0
$\mathrm{H_2O_2 + OH \rightleftharpoons H_2O + HO_2}$		7.08×10^{12}	0.0	6.0
$\mathrm{H_2O_2 + O \rightleftharpoons HO_2 + OH}$		9.63×10^{6}	2.0	16.7

Table 2.1: Rate coefficients in Arrhenius form $k = AT^n \exp\left(-E/R^oT\right)$ as given in [4].

[a] Units are mol, s, cm^3, kJ, and K.

[b] Chaperon efficiencies are 2.5 for H_2, 16.0 for H_2O, and 1.0 for all other species; Troe falloff with $F_c = 0.5$ [44]

[c] Chaperon efficiencies are 2.5 for H_2, 12.0 for H_2O, and 1.0 for all other species.

[d] Chaperon efficiencies are 2.5 for H_2, 6.0 for H_2O, and 1.0 for all other species;
$F_c = 0.265 \exp\left(-T/94\mathrm{K}\right) + 0.735 \exp\left(-T/1756\mathrm{K}\right) + \exp\left(-5182\mathrm{K}/T\right)$

2.2 Skeletal mechanism

The simplification begins by systematically comparing the structure of flames and the homogeneous autoignition histories obtained with the detailed chemistry and those obtained with different subsets of elementary reactions. The comparisons, performed for a wide range of conditions of initial temperature, composition and pressure, were instrumental in identifying elementary reactions that contribute negligibly to the reaction process and can be therefore discarded in the first approximation. As the final outcome of the analysis, it was found that the twelve elementary reactions shown in Table 2.2, of which only six are reversible, suffice to describe premixed and nonpremixed flames, autoignition and detonations under conditions of practical interest. Included in the table are the reaction constants for the forward (f) and backward (b) rates as well as the chaperon efficiencies involved in reactions $4f$, 8, 9 and $12f$ and the rate parameters for the non-Lindemann pressure dependence of reactions $4f$ and $12f$.

	Reaction		A[a]	n	E[a]
1	$H+O_2 \rightleftharpoons OH+O$	k_f	$3.52\ 10^{16}$	-0.7	71.42
		k_b	$7.04\ 10^{13}$	-0.26	0.60
2	$H_2+O \rightleftharpoons OH+H$	k_f	$5.06\ 10^{4}$	2.67	26.32
		k_b	$3.03\ 10^{4}$	2.63	20.23
3	$H_2+OH \rightleftharpoons H_2O+H$	k_f	$1.17\ 10^{9}$	1.3	15.21
		k_b	$1.28\ 10^{10}$	1.19	78.25
4	$H+O_2+M \rightarrow HO_2+M$[b]	k_0	$5.75\ 10^{19}$	-1.4	0.0
		k_∞	$4.65\ 10^{12}$	0.44	0.0
5	$HO_2+H \rightarrow 2OH$		$7.08\ 10^{13}$	0.0	1.23
6	$HO_2+H \rightleftharpoons H_2+O_2$	k_f	$1.66\ 10^{13}$	0.0	3.44
		k_b	$2.69\ 10^{12}$	0.36	231.86
7	$HO_2+OH \rightarrow H_2O+O_2$		$2.89\ 10^{13}$	0.0	-2.08
8	$H+OH+M \rightleftharpoons H_2O+M$[c]	k_f	$4.00\ 10^{22}$	-2.0	0.0
		k_b	$1.03\ 10^{23}$	-1.75	496.14
9	$2H+M \rightleftharpoons H_2+M$[c]	k_f	$1.30\ 10^{18}$	-1.0	0.0
		k_b	$3.04\ 10^{17}$	-0.65	433.09
10	$2HO_2 \rightarrow H_2O_2+O_2$		$3.02\ 10^{12}$	0.0	5.8
11	$HO_2+H_2 \rightarrow H_2O_2+H$		$1.62\ 10^{11}$	0.61	100.14
12	$H_2O_2+M \rightarrow 2OH+M$[d]	k_0	$8.15\ 10^{23}$	-1.9	207.62
		k_∞	$2.62\ 10^{19}$	-1.39	214.74

Table 2.2: Rate coefficients in Arrhenius form $k = AT^n \exp(-E/R^oT)$, for the skeletal mechanism.

[a] Units are mol, s, cm^3, kJ, and K.

[b] Chaperon efficiencies are 2.5 for H_2, 16.0 for H_2O, and 1.0 for all other species; Troe falloff with $F_c = 0.5$

[c] Chaperon efficiencies are 2.5 for H_2, 12.0 for H_2O, and 1.0 for all other species.

[d] Chaperon efficiencies are 2.5 for H_2, 6.0 for H_2O, and 1.0 for all other species;
$F_c = 0.265\exp(-T/94\mathrm{K}) + 0.735\exp(-T/1756\mathrm{K}) + \exp(-5182\mathrm{K}/T)$

Skeletal mechanisms that contain fewer reactions can be used for specific combustion conditions. For instance, the submechanism formed by selecting the three shuffle reactions 1–3, the recombination reaction 4f, and the HO_2 consuming reactions $5f$, $6f$ and $7f$, has been shown recently to describe accurately lean deflagrations [30]. The direct recombination reactions $8f$ and $9f$ need to be added if accuracy is required in describing stoichiometric and rich deflagrations as well as non-premixed flames. Another submechanism, formed by selecting the three shuffle reactions 1–3, the recombination reaction 4f, and the initiation step 6b, would describe accurately high-temperature autoignition [37, 45], as seen in the next chapter. Yet another submechanism, presented in Chapter 6, will be seen to describe low-temperature autoignition.

The twelve steps identified in this section, to be used as a basis for the chemistry-reduction analysis presented in the remainder of the chapter, describe accurately premixed and non-premixed combustion, as well as autoignition and detonations over the whole flammability range, from low to very high pressure. The following paragraphs present the reactions categorized according to their roles in the combustion process. The presentation uses the numbering introduced in Table 2.2 and includes in parentheses reactions of the original detailed mechanism of Table 2.1 that were discarded in developing the short mechanism.

Hydrogen-oxygen shuffle reactions

$$\begin{aligned}
\mathrm{H} + \mathrm{O_2} &\overset{1}{\rightleftharpoons} \mathrm{OH} + \mathrm{O} \\
\mathrm{H_2} + \mathrm{O} &\overset{2}{\rightleftharpoons} \mathrm{OH} + \mathrm{H} \\
\mathrm{H_2} + \mathrm{OH} &\overset{3}{\rightleftharpoons} \mathrm{H_2O} + \mathrm{H} \\
(\mathrm{H_2O} + \mathrm{O} &\rightleftharpoons 2\mathrm{OH})
\end{aligned}$$

These four rapid reactions describe the H-O-OH radical conversion in the radical pool. Although all four are in principle important, the first three shuffle reactions are sufficient to describe radical chain branching, in that neglecting the fourth reaction results in an erroneous balance between O and OH in very lean deflagrations, but it is otherwise inconsequential with respect to global flame characteristics, including burning velocities [30].

Recombination reactions

$$\begin{aligned}
\mathrm{H} + \mathrm{O_2} + \mathrm{M} &\overset{4}{\rightarrow} \mathrm{HO_2} + \mathrm{M} \\
\mathrm{H} + \mathrm{OH} + \mathrm{M} &\overset{8}{\rightleftharpoons} \mathrm{H_2O} + \mathrm{M} \\
\mathrm{H} + \mathrm{H} + \mathrm{M} &\overset{9}{\rightleftharpoons} \mathrm{H_2} + \mathrm{M} \\
(\mathrm{O} + \mathrm{O} + \mathrm{M} &\rightleftharpoons \mathrm{O_2} + \mathrm{M}) \\
(\mathrm{H} + \mathrm{O} + \mathrm{M} &\rightleftharpoons \mathrm{OH} + \mathrm{M}) \\
(\mathrm{O} + \mathrm{OH} + \mathrm{M} &\rightleftharpoons \mathrm{HO_2} + \mathrm{M})
\end{aligned}$$

Of the six recombination reactions, step 4 is by far the most important under all conditions. Inclusion of steps 8f and 9f improves accuracy of calculated deflagration velocities in stoichiometric and rich mixtures. On the other hand, the reverse steps 8*b* and 9*b* need to be retained if chemical equilibrium at high temperature is to be properly described, a key factor in accurate computations of detonations, for example. This is illustrated in Figure 2.1, which compares the evolution of mole fractions of H_2, O_2 and H_2O during an autoignition process in a homogeneous reactor obtained with three different mechanisms, namely, the complete 21-step San Diego mechanism, the subset of reactions 1–7 and the subset of reactions 1–9 including the two recombination reactions. Note that the species and temperature evolutions are better predicted when the recombination reactions are included, especially as equilibrium is approached.

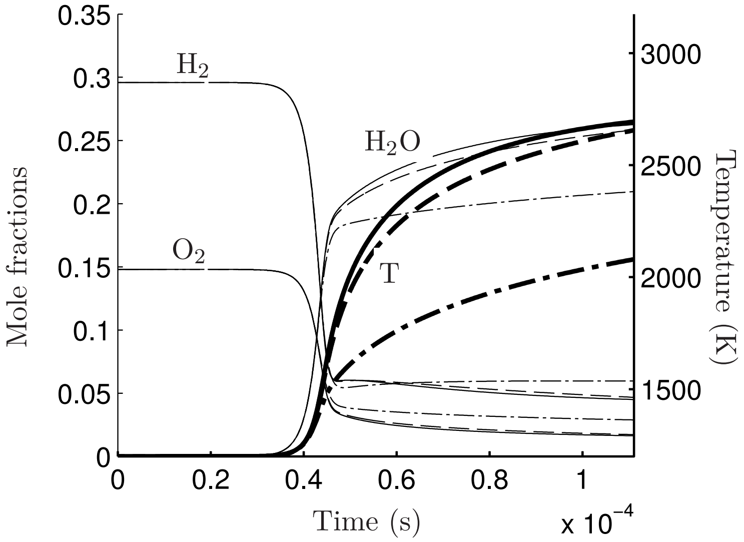

Figure 2.1: The evolution of the main species and temperature in a homogeneous reactor as obtained for $\phi = 1$ and $p = 1$atm with initial temperature $T = 1200$K with use made of the detailed 21-step San Diego chemistry (solid lines), the subset of reactions 1 to 9 (dashed lines), and the subset of reactions 1 to 7, i.e., neglecting the two recombination reactions 8 and 9 (dot-dashed lines).

Hydroperoxyl consuming reactions

$$\begin{aligned}
HO_2 + H &\overset{5}{\rightarrow} 2OH \\
HO_2 + H &\overset{6}{\rightleftharpoons} H_2 + O_2 \\
HO_2 + OH &\overset{7}{\rightarrow} H_2O + O_2 \\
(HO_2 + H &\rightleftharpoons H_2O + O) \\
(HO_2 + O &\rightleftharpoons OH + O_2)
\end{aligned}$$

Hydroperoxil radicals, created through $H + O_2 + M \overset{4}{\rightarrow} HO_2 + M$, are consumed mainly by reactions 5, 6, and 7, the latter being only significant in fuel-lean environments in which OH appears in concentrations that are much larger than that of H. The hydroperoxyl reaction with O and collisions with H leading to $H_2O + O$ were found to be always unimportant. When the conditions are not too fuel-lean, the most rapid removal of HO_2 is through the forward step 5, which serves to regenerate radicals. Its forward rate is about five times as fast as that of step 6, which is chain-terminating. The competition between both steps introduces a factor 1/6 in the effective radical-removal rate associated with step 4. Step 6 is important also because its reverse is by far the dominant initiation step in autoignition; only under fuel-rich high-temperature conditions can H_2 dissociation, the reverse of step 9, compete with the reverse of step 6 in producing radicals.

Hydrogen peroxide reactions:

$$\begin{aligned}
HO_2 + HO_2 &\overset{10}{\rightarrow} H_2O_2 + O_2 \\
HO_2 + H_2 &\overset{11}{\rightarrow} H_2O_2 + H \\
H_2O_2 + M &\overset{12}{\rightarrow} 2OH + M \\
(H_2O_2 + H &\rightleftharpoons H_2O + OH) \\
(H_2O_2 + OH &\rightleftharpoons H_2O + HO_2) \\
(H_2O_2 + O &\rightleftharpoons HO_2 + OH)
\end{aligned}$$

Hydrogen peroxide becomes important at high pressures and also in low-temperature regions of atmospheric-pressure flames. The backward rate of step 10 is always negligible, as is the backward rate of step 12, which is always much smaller than those of other recombination reactions. The species H_2O_2 is important at high pressures, when the HO_2 concentrations are sufficiently high for H_2O_2 production through step 10 to be significant. Radical regeneration by step 12 opens up an alternative chain-branching route, associated with the third explosion limit. To be able to describe high-pressure deflagrations near flammability limits, detonations, and also high-pressure autoignition with reasonable accuracy, it is therefore important to retain al least these two irreversible steps 10 and 12. Neglecting step 11 would lead to satisfactory results in all conditions, except for auto-ignition of very rich mixtures at high pressures, where HO_2 consumption would be underpredicted, leading to overpredictions of induction times. The increased accuracy associated with the inclusion of reaction 11 can be clearly appreciated in Figure 2.2, where the auto-ignition time obtained in a homogeneous reactor at high pressure and with an initial temperature of 1500K obtained using the 21-step San Diego mechanism is compared with that determined with the 12-step short mechanism, and with the same short description excluding step 11.

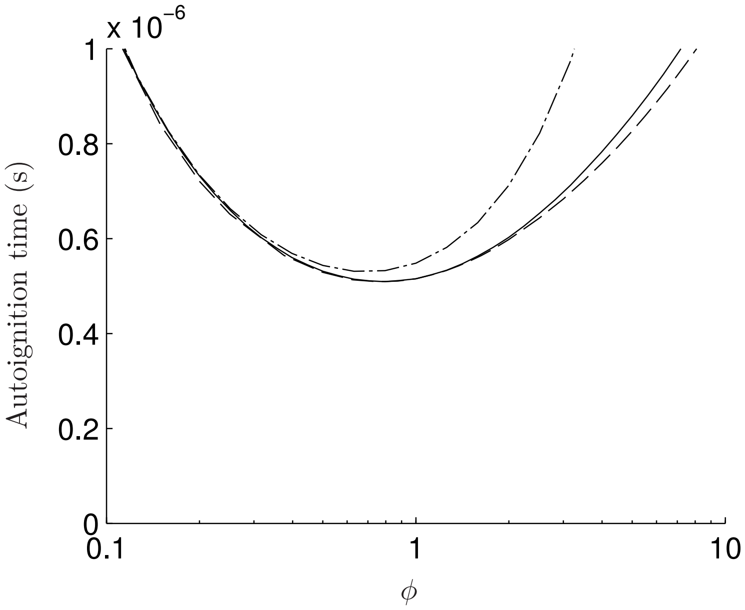

Figure 2.2: The variation with equivalence ratio of the induction time obtained with the inflection-point criterion in isobaric homogeneous combustion for an initial temperature $T = 1500$ K and a pressure $p = 10$ atm, as obtained with the detailed 21-step chemistry (solid curves), with the short 12-step chemistry (dashed curves) and with the 11-step description, i.e. neglecting step 11. (dot-dashed curves).

2.3 Steady-state approximations

The reduction continues by introducing steady-state assumptions for intermediates. The accuracy of this approximation and the number of intermediates that can be assumed to be in steady state without excessive loss of accuracy depend on the combustion conditions. Thus, in deflagrations, steady state approximations can be assumed for OH, O and HO_2 [30], while the same approximation for H atoms would be very poor except near the lean flammability limit. In diffusion flames, the steady state assumption for OH is more accurate than that for O for the purpose of calculating critical ignition and extinction strain rates in counterflow configurations, but even imposing both of these steady states leads to errors in critical strain rates only of about 20% [35]. Thus errors approaching 20% for certain results must be accepted in imposing the O and OH steady states to achieve the reduced chemistry. In autoignition processes, on the other hand, a steady state assumption for HO_2 results in a poor approximation [37] and a steady state approximation for H would apply only under extremely fuel-lean conditions, beyond normal flammability limits, while for O and OH it is accurate in fuel-rich systems [28]. As for the molecule H_2O_2, its concentration is always sufficiently small for the steady-state approximation to be a very accurate representation under the conditions explored below, the only exceptions being high-pressure deflagrations near flammability conditions and autoignition below crossover.

The above considerations indicate that steady-state assumptions for O, OH, HO_2, and H_2O_2 can be introduced in seeking a reduced description that describes with reasonable accuracy premixed and nonpremixed flames, except possibly high-pressure deflagrations near flammability limits. To identify the resulting reduced chemistry the equations expressing the production rate of the different chemical species $\dot{C}_i$ for the 12-step skeletal mechanism can be combined linearly to give

$$\begin{aligned}
\dot{C}_{\mathrm{H_2O}} + \dot{C}_{\mathrm{O}} + \dot{C}_{\mathrm{OH}} + 2\dot{C}_{\mathrm{H_2O_2}} &= 2\omega_{\mathrm{I}} \\
\dot{C}_{\mathrm{O_2}} + \dot{C}_{\mathrm{HO_2}} &= -\omega_{\mathrm{I}} \\
\dot{C}_{\mathrm{H_2}} - \dot{C}_{\mathrm{OH}} - 2\dot{C}_{\mathrm{O}} + \dot{C}_{\mathrm{HO_2}} - 2\dot{C}_{\mathrm{H_2O_2}} &= \omega_{\mathrm{II}} - 3\omega_{\mathrm{I}} \\
\dot{C}_{\mathrm{H}} + \dot{C}_{\mathrm{OH}} + 2\dot{C}_{\mathrm{O}} - \dot{C}_{\mathrm{HO_2}} + 2\dot{C}_{\mathrm{H_2O_2}} &= 2\omega_{\mathrm{I}} - 2\omega_{\mathrm{II}}
\end{aligned} \tag{2.2}$$

where the rates

$$\begin{aligned}
\omega_{\mathrm{I}} &= \omega_1 + \omega_{5f} + \omega_{10f} + \omega_{11f} \\
\omega_{\mathrm{II}} &= \omega_{4f} + \omega_8 + \omega_9 - \omega_{10f} - \omega_{11f}
\end{aligned} \tag{2.3}$$

are related to those of the elementary reactions. Here, ω_{if} and ω_{ib} represent the forward and backward rates of the i-th reaction in the skeletal mechanism. When neither f nor b is present as a subscript, $\omega_i = \omega_{if} - \omega_{ib}$ denotes the difference between the forward and backward rates. At steady state, the concentrations of the species O, OH, HO_2 and H_2O_2 are much smaller than those of the other species and their production rates $\dot{C}_{\mathrm{O}}$, $\dot{C}_{\mathrm{OH}}$, $\dot{C}_{\mathrm{HO_2}}$ and $\dot{C}_{\mathrm{H_2O_2}}$ can be correspondingly neglected above, indicating that with the approximations introduced, the chemistry reduces to the two overall steps

$$\begin{aligned}
3\mathrm{H_2} + \mathrm{O_2} &\overset{\mathrm{I}}{\rightleftharpoons} 2\mathrm{H_2O} + 2\mathrm{H} \\
\mathrm{H} + \mathrm{H} + \mathrm{M} &\overset{\mathrm{II}}{\rightleftharpoons} \mathrm{H_2} + \mathrm{M},
\end{aligned}$$

with overall rates given in (2.3). Note that, although the reduced chemistry can be expressed in terms of different alternative sets of overall reactions, the resulting formulations are all equivalent. The one selected here is written in an intuitive form that serves to identify the main chemical processes involved in hydrogen combustion: it includes a branching reaction I and a recombination reaction II.

The computation of the rates ω_{1b}, ω_{7f} and ω_{8f} requires knowledge of the concentrations of O and OH whereas the rates ω_{5f}, ω_{10f} and ω_{11f} involve the concentration of HO_2. These concentrations can be obtained by solving the corresponding steady-state equations $\dot{C}_{\mathrm{O}} = \omega_1 - \omega_2 = 0$, $\dot{C}_{\mathrm{OH}} = \omega_1 + \omega_2 - \omega_3 + 2\omega_{5f} - \omega_{7f} - \omega_8 + 2\omega_{12f} = 0$ and $\dot{C}_{\mathrm{HO_2}} = \omega_{4f} - \omega_{5f} - \omega_6 - \omega_{7f} - 2\omega_{10f} - \omega_{11f} = 0$, with $\omega_{12f} = \omega_{10f} + \omega_{11f}$ as corresponds to the molecule H_2O_2 being in steady state, to give

$$C_{\mathrm{OH}} = [(A_1^2 + 4A_0A_2)^{1/2} - A_1]/(2A_2), \tag{2.4}$$

$$C_{\mathrm{O}} = \frac{k_{1f}C_{\mathrm{H}}C_{\mathrm{O_2}} + k_{2b}C_{\mathrm{OH}}C_{\mathrm{H}}}{k_{1b}C_{\mathrm{OH}} + k_{2f}C_{\mathrm{H_2}}}, \tag{2.5}$$

where

$$\begin{aligned}
A_0 &= C_{\mathrm{H}_2} k_{2f} (2k_{1f} C_{\mathrm{H}} C_{\mathrm{O}_2} + k_{3b} C_{\mathrm{H}} C_{\mathrm{H}_2\mathrm{O}} + 2k_{5f} C_{\mathrm{H}} C_{\mathrm{HO}_2} \\
&\quad + 2k_{10f} C^2_{\mathrm{HO}_2} + 2k_{11f} C_{\mathrm{HO}_2} C_{\mathrm{H}_2} + k_{8b} C_{\mathrm{M}_8} C_{\mathrm{H}_2\mathrm{O}}), \\
A_1 &= +C_{\mathrm{H}_2} k_{2f} (k_{8f} C_{\mathrm{M}_8} C_{\mathrm{H}} + k_{7f} C_{\mathrm{HO}_2} + k_{3f} C_{\mathrm{H}_2}) \\
&\quad - k_{1b} (k_{3b} C_{\mathrm{H}} C_{\mathrm{H}_2\mathrm{O}} + 2k_{5f} C_{\mathrm{H}} C_{\mathrm{HO}_2} \\
&\quad + 2k_{10f} C^2_{\mathrm{HO}_2} + 2k_{11f} C_{\mathrm{HO}_2} C_{\mathrm{H}_2} + k_{8b} C_{\mathrm{M}_8} C_{\mathrm{H}_2\mathrm{O}}), \\
A_2 &= k_{1b} (2k_{2b} C_{\mathrm{H}} + k_{3f} C_{\mathrm{H}_2} + k_{7f} C_{\mathrm{HO}_2} + k_{8f} C_{\mathrm{M}_8} C_{\mathrm{H}}),
\end{aligned}$$

and

$$\begin{aligned}
C_{\mathrm{HO}_2} &= \frac{-B_1 + \sqrt{B_1^2 + 4B_0 B_2}}{2B_2}, \qquad (2.6) \\
B_0 &= k_{6b} C_{\mathrm{H}_2} C_{\mathrm{O}_2} + k_{4f} C_{\mathrm{H}} C_{\mathrm{O}_2} C_{\mathrm{M}_4}, \\
B_1 &= k_{5f} C_{\mathrm{H}} + k_{6f} C_{\mathrm{H}} + k_{7f} C_{\mathrm{OH}} + k_{11f} C_{\mathrm{H}_2}, \\
B_2 &= 2k_{10f}.
\end{aligned}$$

Equations (2.4) and (2.6) are coupled and need to be solved simultaneously. It is seen however that the additional computational cost involved is limited because no more than five iterations are needed for convergence when an iterative procedure similar to that proposed in [29] is established. Note that other proposals for reduced chemistry descriptions [29] use truncated expressions for C_{OH}, instead of Eq. (2.4). This however can result in significant errors in the computation of the flame speed. It is also worth pointing out that inclusion of reactions $10f$ and $11f$ in the rate expressions improves predictive capabilities at high pressure beyond those of previous two-step mechanisms [29].

2.4 Validation of the two-step mechanism for flame computations

Extensive computations of different H_2-air combustion configurations were performed to test the accuracy of the skeletal and 2-step reduced mechanisms. The COSILAB code [46] was used to compute steady planar deflagrations and nonpremixed counterflow flames with detailed transport descriptions accounting for thermal diffusion. The results, including those shown in Figs. 2.3, 2.4 and 2.5, indicate that the simplified mechanisms describe with sufficient accuracy burning rates and flammability limits in steady planar deflagrations as well as peak temperatures and extinction strain rates in nonpremixed counterflow flames. It can be seen in Fig. 2.3 that for the reduced chemistry, the largest errors in predictions of flame propagation velocities, on the order of 12 %, are found at atmospheric pressure, whereas at higher pressures the steady-state assumptions present in the reduced chemistry become more accurate and yield better burning-rate predictions, except near the flammability limits, with noticeable departures observed in particular in the computations for $p = 50$ atm as the rich limit is approached. The reduced chemistry also tends to overpredict peak temperatures in nonpremixed flames, giving departures on the order of 50 K for all strain rates, as seen in Fig. 2.4. Figure 2.5 exhibits profiles of H mass fraction and temperature across planar counterflow diffusion flames corresponding to three different values of the strain rate a, including conditions very close to extinction. As can be seen, excellent agreement is found for all conditions tested.

The above results clearly show that the two-step reduced mechanism provides a reasonably accurate description for both deflagrations and diffusion flames under varying conditions of temperature, pressure and composition. Further improvements associated with reduced computational times were sought by investigating procedures to avoid the iterative solution of (2.4) and (2.6). As an alternative explicit methodology we propose the introduction of the simplified truncated expression

$$C_{\mathrm{HO}_2} \simeq \frac{k_{4f} C_{\mathrm{O}_2}}{k_{5f} + k_{6f}}, \qquad (2.7)$$

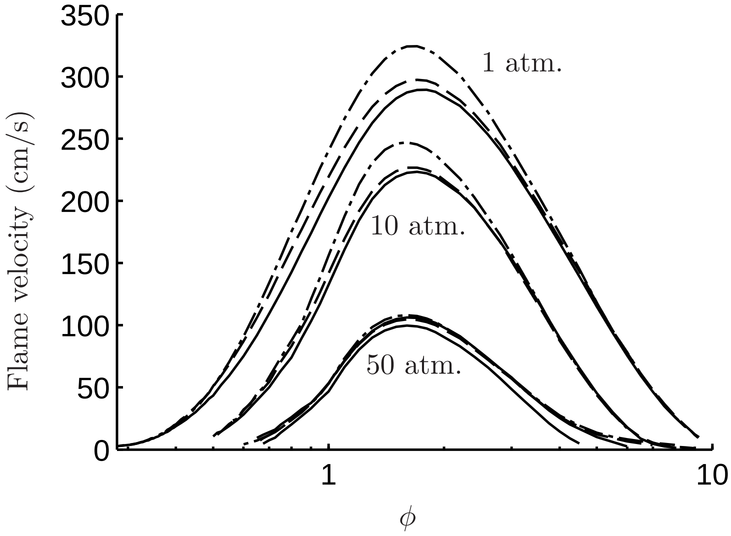

Figure 2.3: The variation with equivalence ratio of the laminar burning rate of hydrogen-air planar deflagrations with initial temperature $T_u = 300$ K and three different pressures as obtained with the detailed 21-step chemistry (solid curves), with the short 12-step chemistry (dashed curves) and with the 2-step reduced mechanism (dot-dashed curves).

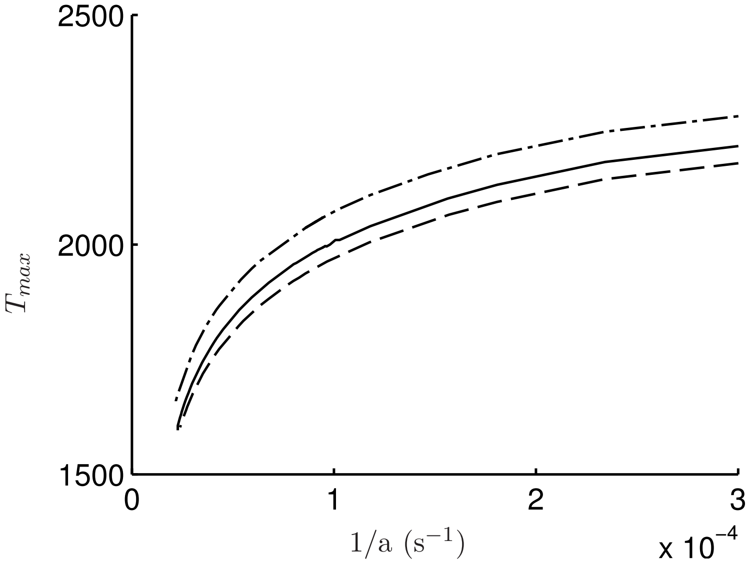

Figure 2.4: The variation with strain rate of the maximum temperature in a hydrogen-air planar counterflow at atmospheric pressure with feed-stream temperatures $T = 300$ K as obtained with the detailed 21-step chemistry (solid curves), with the short 12-step chemistry (dashed curves) and with the 2-step reduced mechanism (dot-dashed curves).

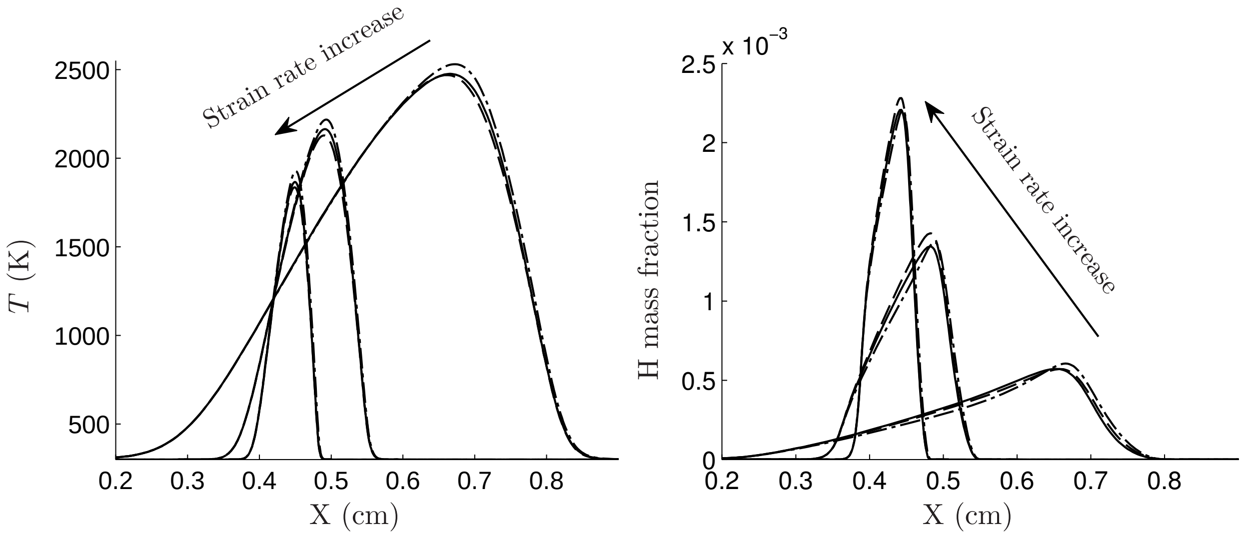

Figure 2.5: Temperature and H mass fraction profiles in a hydrogen-air planar counterflow diffusion flame at atmospheric pressure with feed-stream temperatures $T = 300$K, for $a = (400, 4000, 40000)$ s^{-1}, as obtained with the detailed 21-step chemistry (solid curves), with the short 12-step chemistry (dashed curves), and with the 2-step reduced mechanism (dot-dashed curves).

independent of C_{OH}, into (2.4) to compute C_{OH}, with C_{HO_2} calculated a posteriori using its complete expression (2.6) with use made of the value for C_{OH} previously computed. Figure 2.6 compares laminar burning velocities of steady planar flames obtained with the 21-step detailed chemistry with those obtained with the two-step mechanism including the iterative evaluation of the steady-state expressions and also with direct evaluation of C_{OH} with use made of (2.7). As can be seen, the direct evaluation methodology does not degrade appreciably the accuracy of the reduced chemistry.

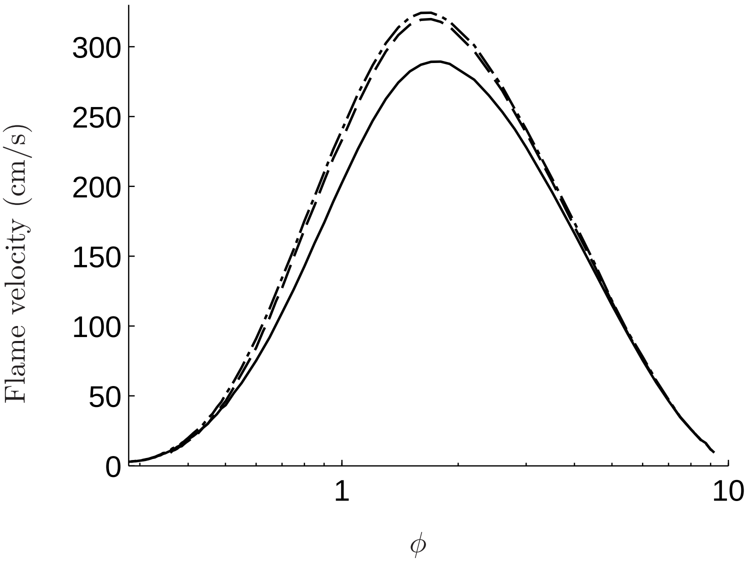

Figure 2.6: The variation with equivalence ratio of the laminar burning rate of hydrogen-air planar deflagrations with initial temperature $T_u = 300$ K at atmospheric pressure as obtained with the detailed 21-step chemistry (solid curves) and with the 2-step chemistry with iterative computation of steady-state radicals (dot-dashed curves) and with the simplified direct evaluation procedure (dashed curves).

2.5 Conclusions

We have seen that twelve elementary steps selected from the 21-step detailed chemistry suffice to describe accurately hydrogen combustion under all conditions of practical interest. This skeletal mechanism represents a contribution on its own, which can be seen as an extension of a previously proposed 9-step skeletal mechanism [29, 30] widening the domain of applicability of the short chemistry to high-pressure conditions, of interest in gas-turbine applications. The 12-step skeletal mechanism has been extensively validated to give solid grounds for additional simplifications. Steady-state approximations for O, OH, HO_2 and H_2O_2 were seen to hold with reasonable accuracy in premixed and non-premixed flames, leading to a two-step reduced chemistry description. We shall see in the next chapter that this two-step mechanism is however unable to describe autoignition processes with reasonable accuracy. A three-step reduced chemistry description obtained by including HO_2 out of steady state will be seen to improve predictions of high-temperature autoignition times, in agreement with previous studies [37], with consideration of O and OH departures from steady state needed for increased accuracy, especially in fuel-lean mixtures.

CHAPTER 3

High-temperature autoignition

The study of autoignition processes is of interest for safety reasons associated with the handling and transport of hydrogen. Besides, autoignition is responsible for combustion stabilization in high-velocity burners, as those employed for supersonic propulsion, and is to be avoided upstream from the combustion chamber in lean-premixed gas turbines. Because of all these different applications, there is interest in reduced chemistry mechanisms that can accurately describe the process.

In the past, separate specific reduced mechanisms were used for flames and for autoignition. The derivation of a single mechanism that accurately describes both phenomena is of interest for computations of the complex reactive flows often found in burners. This is the purpose of this chapter, which builds upon the reduced mechanism derived in the previous chapter. It will be shown that the two-step mechanism with H as the only radical out of steady state, which is sufficiently accurate for flames, predicts however ignition times that are much too short because of failure of steady states during the chain-branching explosion above the second explosion limit. It will also be shown that a three-step mechanism, obtained by relaxing the HO_2 steady-state assumption, improves accuracy somewhat above crossover, but for many purposes the resulting underpredictions in high-temperature induction times are still excessive. A correction for these underpredictions, accounting for failure of the O and OH steady-state approximations during radical build-up in lean environments, is to be proposed.

3.1 Computations of autoignition histories with two-step chemistry

The two-step reduced chemistry description derived in Chapter 2 was tested in different high-temperature autoignition configurations including homogeneous reactors and a nonpremixed mixing layer. Figure 3.1 shows the variation of the ignition time t_i with the equivalence ratio ϕ for homogeneous adiabatic combustion in an isobaric reactor obtained with the COSILAB code [46] with detailed, short and two-step reduced chemistry descriptions (and also with a three-step reduced mechanism, to be derived below). The ignition time t_i is defined in the computations by the temperature-inflection criterion, i.e., the time at which the temperature derivative, or heat release, is maximum. As can be seen, the 12-step short scheme gives results that are virtually indistinguishable from those obtained with detailed chemistry. By way of contrast, induction-time predictions obtained with the two-step mechanism contain significant errors that are larger for leaner mixtures. In particular, the reduced chemistry is not able to predict a minimum in the curve of $t_i-\phi$. That is, with both O and OH in steady state, the mixture becomes more reactive for decreasing hydrogen concentrations, whereas with detailed and skeletal chemistries a minimum ignition time, corresponding to the most reactive mixture, is reached for $\phi \simeq 0.8$. This has implications concerning non-premixed ignition, as shown below.

Effects of molecular transport become important in describing autoignition in nonpremixed mixing layers [47], of interest in high-speed propulsion applications for example. To investigate the associated ignition process, the transient evolution of a one-dimensional mixing layer formed by putting into contact at a given

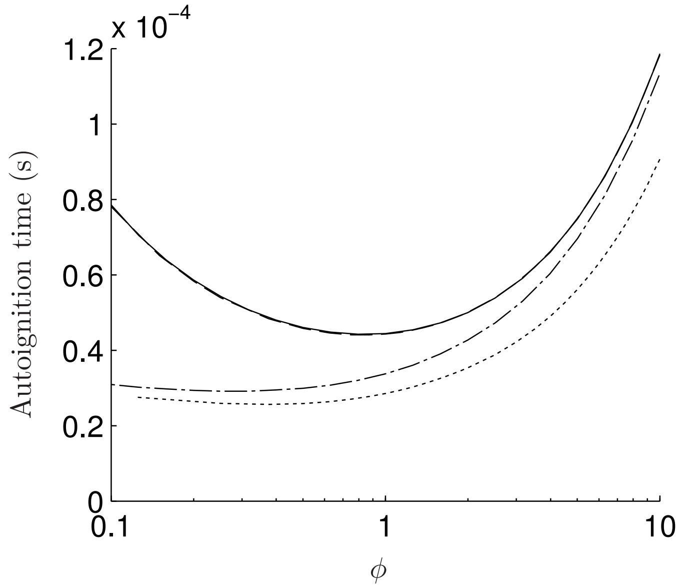

Figure 3.1: The variation with equivalence ratio of the induction time as obtained in an isobaric homogeneous reactor for $T = 1200$ K and $p = 1$ atm with the detailed 21-step chemistry (solid curves), with the short 12-step chemistry (dashed curves), with the 2-step reduced mechanism (dotted curves), and with the 3-step reduced mechanism (dot-dashed curves).

instant of time two semi-infinite spaces of hydrogen and air was investigated with use made of the NTMIX code [48, 49]. If the initial temperature is sufficiently large, chemical reaction occurs as the reactants mix, giving rise to autoignition and to the formation of two premixed fronts that leave behind a trailing diffusion flame [10]. The resulting triple-flame structure can be observed in the plots of heat release rate shown in Fig. 3.2, corresponding to a H_2-air mixing layer at atmospheric pressure with initial temperature $T = 1200$ K. As can be seen by comparing the results of the 21-step mechanism shown in the left-hand-side plot with those of the two-step reduced chemistry shown in the central plot, the errors in autoignition time present in Fig. 3.1 can also be observed here. This reduced chemistry predicts ignition to occur considerably earlier and at a point located farther into the air side of the mixing layer, in agreement with previous theoretical predictions [47].

3.2 Three-step mechanism for hydrogen combustion

In view of the above results, it is clear that the two-step mechanism, although sufficiently accurate for describing flames, fails to describe autoignition processes and therefore needs to be improved. Given the excellent accuracy of the short mechanism employed as a basis for the derivation of the reduced chemistry, the predictive limitations must be associated with the different steady-state assumptions introduced. In particular, the HO_2 steady state is known to be inaccurate during the initial stages of the chain-branching explosion [37] and must be therefore reconsidered in seeking improved accuracy. With both H and HO_2 out of steady state, the overall reactions of the resulting reduced mechanism can be seen to become

$$\begin{aligned} 3\mathrm{H}_2 + \mathrm{O}_2 &\overset{\mathrm{I}}{\rightleftharpoons} 2\mathrm{H}_2\mathrm{O} + 2\mathrm{H} \\ \mathrm{H} + \mathrm{H} + \mathrm{M} &\overset{\mathrm{II}}{\rightleftharpoons} \mathrm{H}_2 + \mathrm{M} \\ \mathrm{H}_2 + \mathrm{O}_2 &\overset{\mathrm{III}}{\rightleftharpoons} \mathrm{HO}_2 + \mathrm{H}, \end{aligned}$$

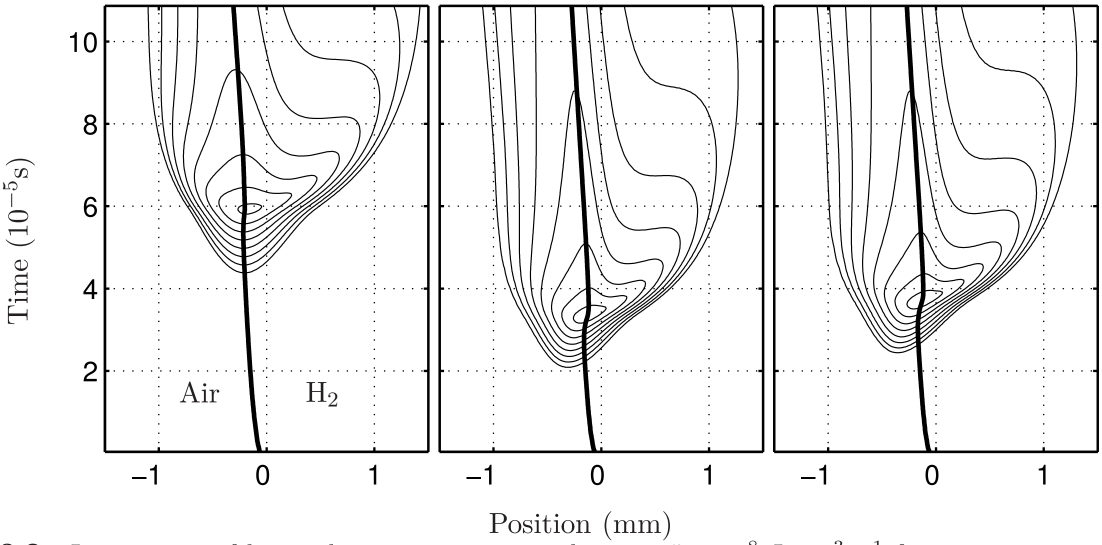

Figure 3.2: Isocontours of heat-release rate corresponding to $2^n \times 10^8$ J m^{-3}s^{-1} for $n = 1$ up to $n = 8$ in the transient one-dimensional H_2/air mixing layer at atmospheric pressure and initial temperature 1200K as obtained with the 21-step chemistry (left plot), with the 2-step reduced chemistry (centered plot) and with the 3-step reduced chemistry (right plot); the black line indicates the location where the mixture is stoichiometric.

with rates given by

$$\begin{aligned} \omega_{\rm I} &= \omega_1 + \omega_{5f} + \omega_{10f} + \omega_{11f} \\ \omega_{\rm II} &= \omega_{4f} + \omega_8 + \omega_9 - \omega_{10f} - \omega_{11f} \\ \omega_{\rm III} &= \omega_{4f} - \omega_{5f} - \omega_6 - \omega_{7f} - 2\omega_{10f} - \omega_{11f}. \end{aligned} \tag{3.1}$$

The expressions given in (2.4) and (2.5) for the steady-state concentrations of OH and O continue being valid, but with the HO_2 concentration calculated as one of the transported species, $C_{\rm OH}$ can be now evaluated explicitly from (2.4), thereby simplifying the computation of the overall rates.

The three-step mechanism was used also in the autoignition computations displayed in Figs. 3.1 and 3.2. In particular, the results shown in Fig. 3.1 indicate that the three-step mechanism improves considerably predictions of ignition times for rich mixtures, with the curve of $t_i - \phi$ asymptotically approaching that obtained with detailed chemistry for $\phi \to \infty$. However, the resulting underpredictions are still significant for stoichiometric mixtures and become larger as the mixture becomes leaner. Similar inaccuracies are observed in the mixing-layer computation shown in 3.2. Ignition is predicted to occur too early and at a location erroneously displaced towards the oxidizer side. As can be seen, the improvement achieved in this case by incorporating HO_2 in the reduced mechanism is only marginal.

The three-step reduced chemistry was also employed for the description of the induction region found downstream from the leading shock wave in detonations. In particular, Fig. 3.3 shows the variation of the pressure, temperature, and selected species mole fractions in a steady Chapman-Jouguet detonation. As can be seen, while the short 12-step mechanism provides excellent accuracy for main reactants, H atoms, temperature, and pressure and also a reasonably accurate representation for HO_2, the three-step mechanism leads to much larger errors that affect both the resulting profiles and the final equilibrium conditions. The length of the induction region is clearly underpredicted, with errors comparable to those obtained in isobaric ignition histories (see Fig. 3.1).

Clearly, the underpredictions of ignition times seen in Figs. 3.1 and 3.2 and that of induction length observed in Fig. 3.3 are too large for the associated reduced mechanisms to provide an acceptable combustion description in the presence of autoignition above the second explosion limit. The errors are associated with

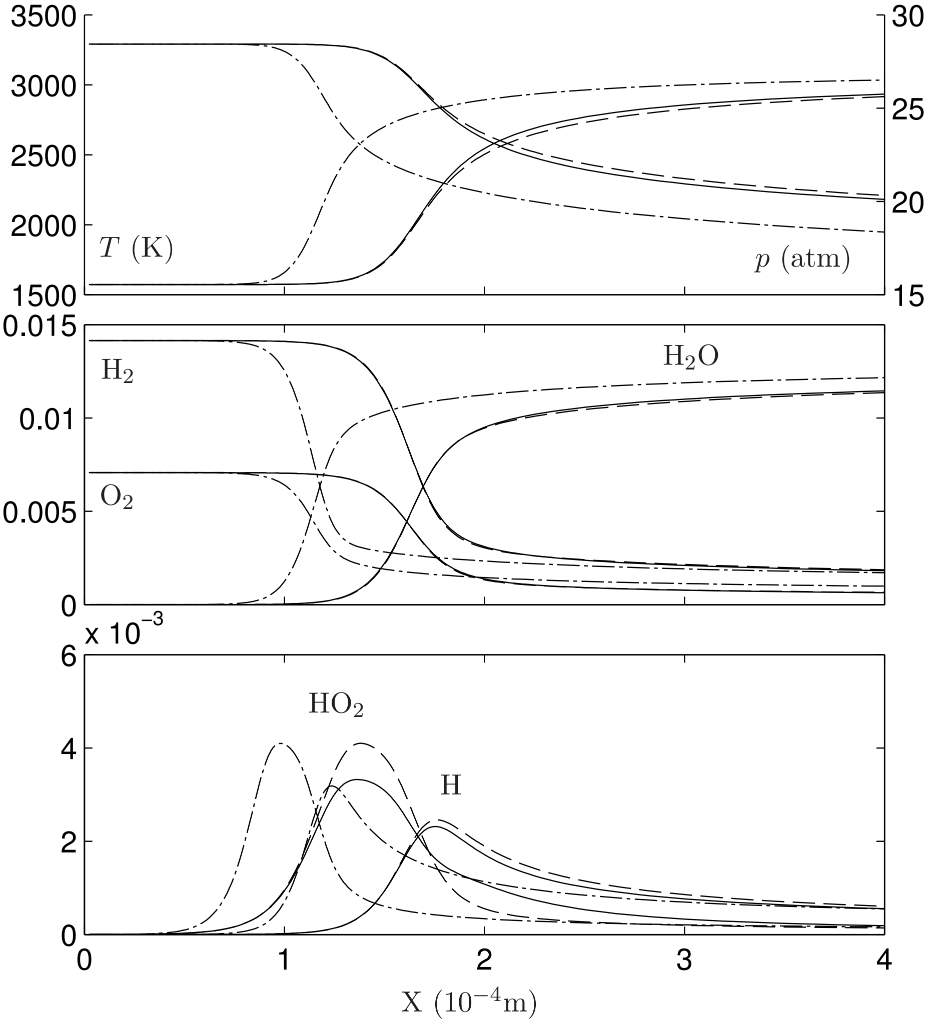

Figure 3.3: The variation with the distance from the shock of the pressure, temperature and species mole fractions in a Chapman-Jouguet detonation propagating in a stoichiometric hydrogen-air mixture with $p = 1$ atm and T=300K as obtained with the detailed 21-step chemistry (solid curves), with the short 12-step chemistry (dashed curves), and with the 3-step reduced mechanism (dot-dashed curves).

the lack of accuracy of the steady-state assumptions for O and OH in the initial period of radical branching [37]. These assumptions are, however, excellent approximations when a sufficient radical pool has formed, e.g., within the reaction layer that controls the burning rate of premixed and non-premixed flames. It is therefore of interest to seek ways to improve the description of autoignition with the reduced chemistry, without giving up the simplification associated with the steady-state assumptions of O and OH.

3.3 Analytical description of high-temperature autoignition

In autoignition events at temperatures above crossover, the competition between the chain-branching reactions $1f$ and $2f$ with the chain-carrying reaction $3f$ and the terminating reaction $4f$ controls the autocatalytic radical growth after a short initial period in which the initiation reaction $6b$ creates the first radicals through collisions between the reactants [37, 45]. Therefore, autoignition above the second explosion limit is determined by the five elementary reactions

$$
\begin{aligned}
H + O_2 &\xrightarrow{1f} OH + O\\
H_2 + O &\xrightarrow{2f} OH + H\\
H_2 + OH &\xrightarrow{3f} H_2O + H\\
H + O_2 + M &\xrightarrow{4f} HO_2 + M\\
H_2 + O_2 &\xrightarrow{6b} HO_2 + H.
\end{aligned}
$$

The corresponding branched-chain explosion can be described with the effects of reactant consumption and heat release neglected in the first approximation [37, 45, 50] by integrating the conservation equations for the radicals H, O and OH. With constant temperature and constant reactant concentrations, these conservation equations may be linearized to give

$$
\frac{d}{dt}\bar{C} = \mathbf{A}.\bar{C} + \bar{\epsilon} \quad \text{where} \quad \bar{C} = \begin{bmatrix} C_{\mathrm{H}} \\ C_{\mathrm{O}} \\ C_{\mathrm{OH}} \end{bmatrix}, \tag{3.2}
$$

with initial conditions $\bar{C}(t = 0) = 0$. The components of the 3x3 matrix

$$
\mathbf{A} = \begin{bmatrix} -(k_{1f}C_{\mathrm{O_2}} + k_{4f}C_{\mathrm{O_2}}C_{\mathrm{M_4}}) & k_{2f}C_{\mathrm{H_2}} & k_{3f}C_{\mathrm{H_2}} \\ k_{1f}C_{\mathrm{O_2}} & -k_{2f}C_{\mathrm{H_2}} & 0 \\ k_{1f}C_{\mathrm{O_2}} & k_{2f}C_{\mathrm{H_2}} & -k_{3f}C_{\mathrm{H_2}} \end{bmatrix} \tag{3.3}
$$

represent the reciprocal of the characteristic times associated with reactions 1–4. The constant

$$
\bar{\epsilon} = \begin{bmatrix} k_{6b}C_{\mathrm{O_2}}C_{\mathrm{H_2}} \\ 0 \\ 0 \end{bmatrix} \tag{3.4}
$$

corresponds to the initial production of radicals through the initiation step $6b$, essential to trigger the branched-chain explosion.

The solution of this linear system can then be expressed as

$$
\bar{C} = C_1\bar{V}_1e^{\lambda_1 t} + C_2\bar{V}_2e^{\lambda_2 t} + C_3\bar{V}_3e^{\lambda_3 t} + \bar{C}_0, \tag{3.5}
$$

where $\bar{V}_i$ are the eigenvectors associated with the eigenvalues λ_i of the matrix $\mathbf{A}$, C_i are constants of integration, and $\bar{C}_0$ is the particular solution obtained from $\mathbf{A} \cdot \bar{C}_0 + \bar{\epsilon} = 0$. The eigenvalues λ_i are determined as the solution of the characteristic equation

$$
\det(\lambda\mathbf{I} - \mathbf{A}) = \lambda^3 + l_2\lambda^2 + l_1\lambda - l_0 = 0, \tag{3.6}
$$

where

$$\begin{aligned} l_2 &= k_{1f}C_{\mathrm{O}_2} + k_{2f}C_{\mathrm{H}_2} + k_{3f}C_{\mathrm{H}_2} + k_{4f}C_{\mathrm{O}_2}C_{\mathrm{M}_4}, \\ l_1 &= k_{2f}k_{3f}C_{\mathrm{H}_2}^2 + (k_{2f}+k_{3f})k_{4f}C_{\mathrm{H}_2}C_{\mathrm{O}_2}C_{\mathrm{M}_4}, \\ l_0 &= (2k_{1f}C_{\mathrm{O}_2} - k_{4f}C_{\mathrm{O}_2}C_{\mathrm{M}_4})k_{2f}k_{3f}C_{\mathrm{H}_2}^2. \end{aligned} \tag{3.7}$$

It should be remarked that $l_0 = 0$ at crossover, where $2k_{1f}C_{\mathrm{O}_2} = k_4C_{\mathrm{O}_2}C_{\mathrm{M}_4}$, making the matrix singular. Above crossover, **A** has three real eigenvalues, λ_1, λ_2 and λ_3, only one of which is positive, λ_1. It is shown in Appendix A that λ_2 and λ_3 have always a negative real part, such that $|\lambda_3| \gg |\lambda_2| \gg \lambda_1$, which implies that after a very short time the solution for the radical pool is approximately given by

$$\bar{C} = C_1\bar{V}_1e^{\lambda_1 t} + \bar{C}_0. \tag{3.8}$$

Appendix A also shows that the cubic term in (3.6) can be neglected in the first approximation when evaluating λ_1, leading to the approximate expression

$$\lambda_1 \approx \lambda = \frac{\sqrt{l_1^2 + 4l_0l_2} - l_1}{2l_2}. \tag{3.9}$$

The accuracy of this approximation over a wide range of equivalence ratios is illustrated in Fig. 3.4. It is shown in Appendix A that for sufficiently rich mixtures, such that $C_{\mathrm{H}_2}/C_{\mathrm{O}_2} \gg k_{1f}/k_{2f}$ and $C_{\mathrm{H}_2}/C_{\mathrm{O}_2} \gg k_{1f}/k_{3f}$, the eigenvalue simplifies to

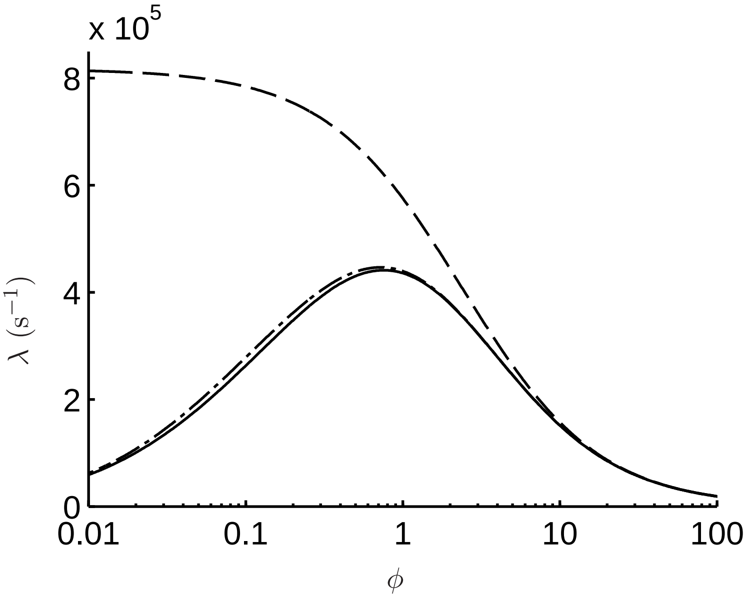

Figure 3.4: The variation with composition of λ_1, solution for (3.6), at $T = 1200$ K and $p = 1$ atm (solid curve) together with the approximate solutions $\lambda_1 \approx 2k_{1f}C_{\mathrm{O}_2} - k_{4f}C_{\mathrm{O}_2}C_{\mathrm{M}_4}$ (dashed curve) and $\lambda_1 \approx \lambda$ as simplified in (3.9) (dot-dashed curve).

$$\lambda_1 \simeq 2k_{1f}C_{\mathrm{O}_2} - k_{4f}C_{\mathrm{O}_2}C_{\mathrm{M}_4}, \tag{3.10}$$

whereas the corresponding eigenvector reduces to C_{H}, indicating that for these rich conditions H becomes the dominant radical in the radical pool with the steady state assumptions for O and OH being reasonably accurate, thereby explaining the good results obtained with the three-step chemistry for rich mixtures in Fig. 3.1.

The exponential radical growth given in (3.8) continues until radical-radical reactions, reactant consumption and heat release become significant, when the radical concentrations reach values comparable to the initial reactant concentrations. For a complete analytic expression for the ignition time, expressions for C_1, V_1 and $\bar{C}_0$ are needed in (3.8). The derivation of these expressions is given in Appendix A, giving an explicit expression for the ignition time

$$t_i = \lambda^{-1} \ln(\varepsilon^{-1}), \tag{3.11}$$

where ε, typically of the order of 10^{-6}, is the characteristic radical mole fraction at the end of the initiation period.

3.4 The modified branching rate

The ignition time given in (3.11) is to be compared with that predicted with the three-step reduced chemistry, which, with O and OH in steady state, would yield

$$C_{\mathrm{H}} \propto \exp[(2k_{1f}C_{\mathrm{O_2}} - k_{4f}C_{\mathrm{O_2}}C_{\mathrm{M_4}})t] \tag{3.12}$$

for the H-atom growth. This is different from the general solution

$$C \propto \exp(\lambda t), \tag{3.13}$$

obtained above for the radical pool, except for very rich mixtures, for which $\lambda \simeq 2k_{1f}C_{\mathrm{O_2}} - k_{4f}C_{\mathrm{O_2}}C_{\mathrm{M_4}}$ and $C \simeq C_{\mathrm{H}}$, as previously discussed. Correspondingly, the ignition time obtained with the reduced chemistry is a factor

$$\Lambda = \lambda/(2k_{1f}C_{\mathrm{O_2}} - k_{4f}C_{\mathrm{O_2}}C_{\mathrm{M_4}}) \tag{3.14}$$

smaller than that obtained by integrating the initial problem (3.2), which explains the differences observed in Figs. 3.1–3.2.

The above discussion suggests that these large errors in autoignition time prediction, associated with the steady-state assumptions for O and OH, can be corrected by modifying the induction time scale through the introduction of modified reaction rates for the reduced chemistry

$$\frac{\omega_{\mathrm{I}}^*}{\omega_{\mathrm{I}}} = \frac{\omega_{\mathrm{II}}^*}{\omega_{\mathrm{II}}} = \frac{\omega_{\mathrm{III}}^*}{\omega_{\mathrm{III}}} = \Lambda, \tag{3.15}$$

where the factor Λ is given by (3.7), (3.9) and (3.14) as a function of the local temperature and composition. This modification of the overall rates is tested in Fig. 3.5, which shows homogeneous ignition times computed with the modified reaction rates (3.15), yielding remarkable agreement over the whole range of conditions investigated. Note that the introduction of the scaling factor Λ does not modify the resulting crossover temperature, so that the reduced chemistry description remains also applicable for conditions close to the second explosion limit.

3.5 The modification criterion

The correction for the rates in (3.15) applies to the description of the rapid chain-branching radical growth that leads to autoignition, but must be switched off in places where the steady-state assumptions for O and OH apply with sufficient accuracy, which occurs in general in hot regions with relatively high radical concentrations. To complete the correction to the reduced chemistry for general use, then a simple

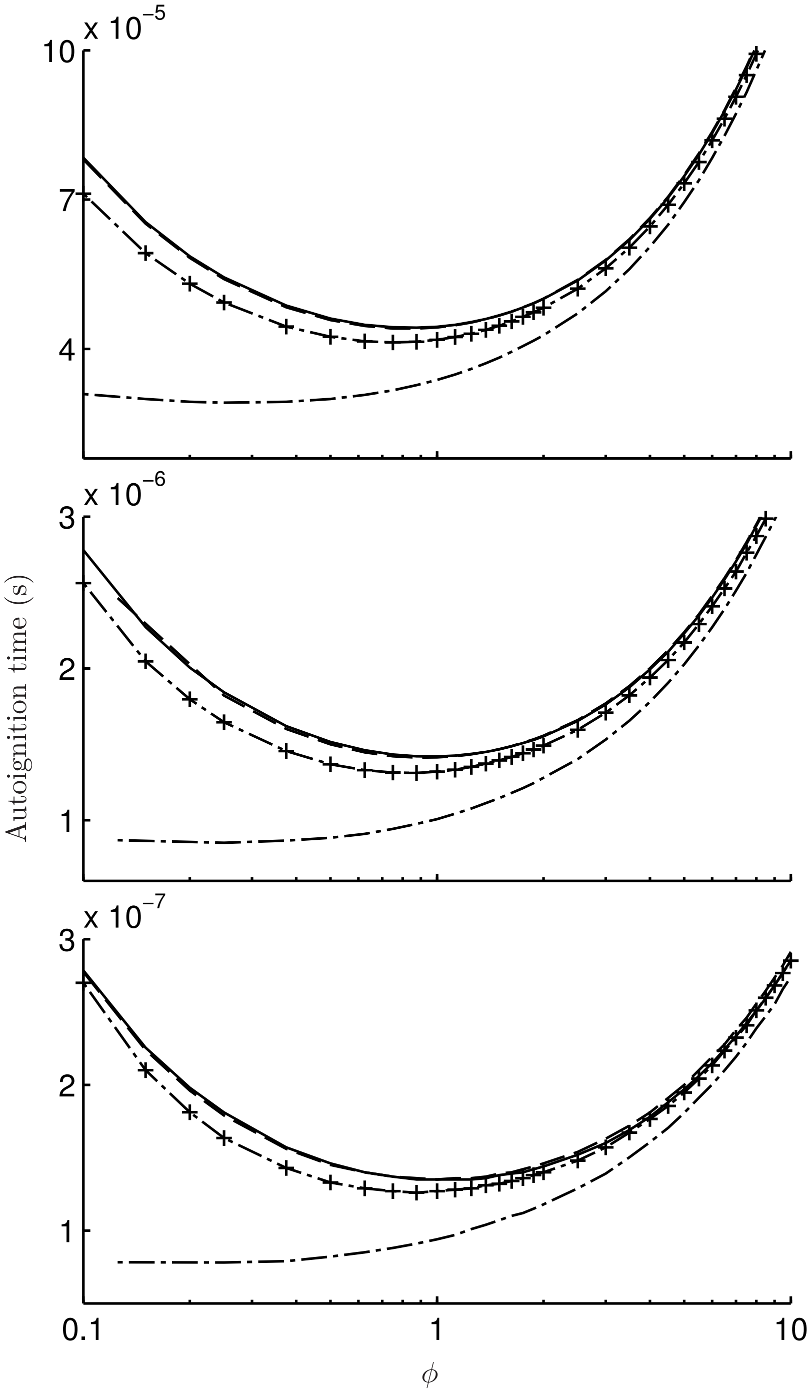

Figure 3.5: The variation with equivalence ratio of the induction time in isobaric homogeneous combustion for different conditions of pressure and initial temperature (upper plot: $T = 1200$ K and $p = 1$ atm; middle plot: $T = 1500$ K and $p = 10$ atm; lower plot: $T = 1800$ K and $p = 50$ atm) as obtained with the detailed 21-step chemistry (solid curves), with the short 12-step chemistry (dashed curves) and with the 3-step reduced mechanism (dot-dashed curves), with the crosses indicating the results obtained with the modified reaction rates (3.15).

criterion is needed that can be employed to identify chain-branching radical explosions automatically in numerical computations of complex reactive flows. For the three-step reduced chemistry, the steady-state approximation of the hydroperoxyl radical HO_2 can be used for that purpose. Under most conditions, in places where the chemical reaction is significant, the H and OH concentrations are sufficiently large for reactions $5f$, $6f$ and $7f$ to maintain the HO_2, produced mainly by reaction $4f$, in steady state. As previously observed [37], this does not occur, however, where autoignition is taking place. In a general computation, therefore, one may identify the places where autoignition is possibly occurring - and where the modified reaction rates (3.15) are therefore needed - by checking the validity of the steady-state assumption for HO_2. For that purpose, the rate of HO_2 production $\dot{C}_{\mathrm{HO}_{2P}} = \omega_{4f} + \omega_{6b}$ and that of HO_2 consumption $\dot{C}_{\mathrm{HO}_{2C}} = \omega_{5f} + \omega_{6f} + \omega_{7f} + 2\omega_{10f} + \omega_{11f}$ are computed locally. The steady-state is regarded as a valid approximation wherever $(\dot{C}_{\mathrm{HO}_{2P}} - \dot{C}_{\mathrm{HO}_{2C}})/(\dot{C}_{\mathrm{HO}_{2P}} + \dot{C}_{\mathrm{HO}_{2C}})$ is smaller than a presumed threshold value, below which $\Lambda = 1$ in (3.15), whereas for larger values the corrected reaction rates must be employed, since autoignition may be occurring. Note that, since Λ enters in (3.15) as a factor affecting all reaction rates, the resulting value of $(\dot{C}_{\mathrm{HO}_{2P}} - \dot{C}_{\mathrm{HO}_{2C}})/(\dot{C}_{\mathrm{HO}_{2P}} + \dot{C}_{\mathrm{HO}_{2C}})$ is independent of whether or not the modification is switched on, thereby guaranteeing numerical stability. Also of interest for numerical implementation is that application of the corrected reaction rates must be subject to the additional condition that the local H-atom chemical production rate be positive, as occurs in autoignition.

The results obtained with use of this simple triggering criterion were found to be quite independent of the threshold value used, provided the value selected was sufficiently small, with a value equal to 0.05 used for the computations shown below. The modification introduced does not affect the results of computations of steady planar deflagrations and counterflow diffusion flames, which remain virtually identical to those determined without the correction, because the steady-state assumption for HO_2 applies in these flames within the reaction region, so that the modified rate is not triggered there. Erroneous triggering on the low-temperature side of high-pressure deflagrations, leading to errors in resulting propagation velocities, was avoided by adding the additional condition of positive H-atom production previously mentioned.

The use of the modified reaction rates improves considerably the description of mixing-layer ignition, as shown in Fig. 3.6, which corresponds to the same conditions previously considered in Fig. 3.2. As can be seen, when the correction is incorporated to the reduced chemistry, the resulting field of heat-release rate including the location of ignition is quite similar to that obtained with detailed chemistry.

The modified three-step kinetics also provides better accuracy in describing detonation structures, as shown in Fig. 3.7. In particular, the degree of accuracy obtained is quite satisfactory concerning the resulting induction length. Errors in peak radical concentrations, on the order of 20 %, are also reasonable. Since O and OH are present at equilibrium in nonnegligible amounts, errors on the order of 5 % appear in the final values of the temperature and pressure when these two species are not taken into account in the overall energy balance, as occurs when using the reduced chemistry. The results in this figure are reasonable for steady, planar, one-dimensional detonations, while cellular detonations, with interacting high-pressure, high-temperature triple points encounter conditions for which the detailed chemistry fails, and vibrational relaxation need to be considered.

3.6 Conclusions

In this chapter, we have shown that a systematically derived three-step overall mechanism based on steady-state approximations for O, OH and H_2O_2, with reaction rates modified by rescaling to improve autoignition-time agreements under fuel-lean and stoichiometric conditions, for which the hypothesized O and OH steady states fail, provides a satisfactory description of most aspects of hydrogen combustion.

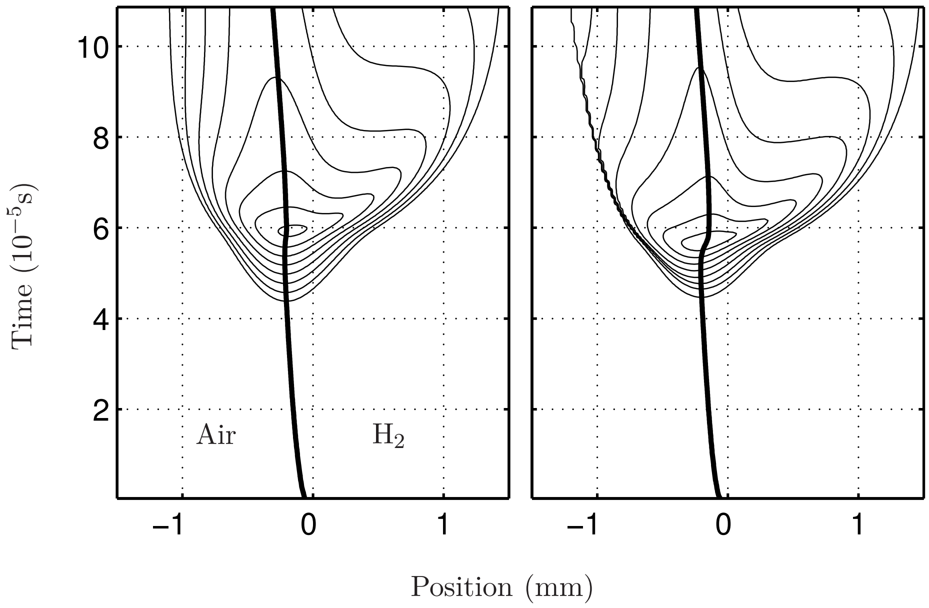

Figure 3.6: Isocontours of heat-release rate corresponding to $2^n \times 10^8$ J m^{-3}s^{-1} for $n = 1$ up to $n = 8$ in the transient one-dimensional H_2/air mixing layer at atmospheric pressure and initial temperature 1200K as obtained with the 21-step chemistry (left plot) and with the 3-step reduced chemistry with modified rates (right-hand-side plot); the black line indicates the location where the mixture is stoichiometric.

Inaccurate representations of minor-species concentrations may be anticipated in certain regions from this reduced chemistry, but for deflagration, detonation, high-temperature ignition and extinction studies in which interest focuses on gasdynamic, transport and heat-release processes, extending to both low-speed and supersonic combustion, these simplified descriptions may enable sufficiently accurate calculations to be performed that otherwise would not be possible.

The work presented in this chapter corresponds to the article "An explicit reduced mechanism for H_2-air combustion", presented on the occasion of the 33rd Symposium on Combustion, in Beijing, China, and published in the Proceedings of the Combustion Institute [51].

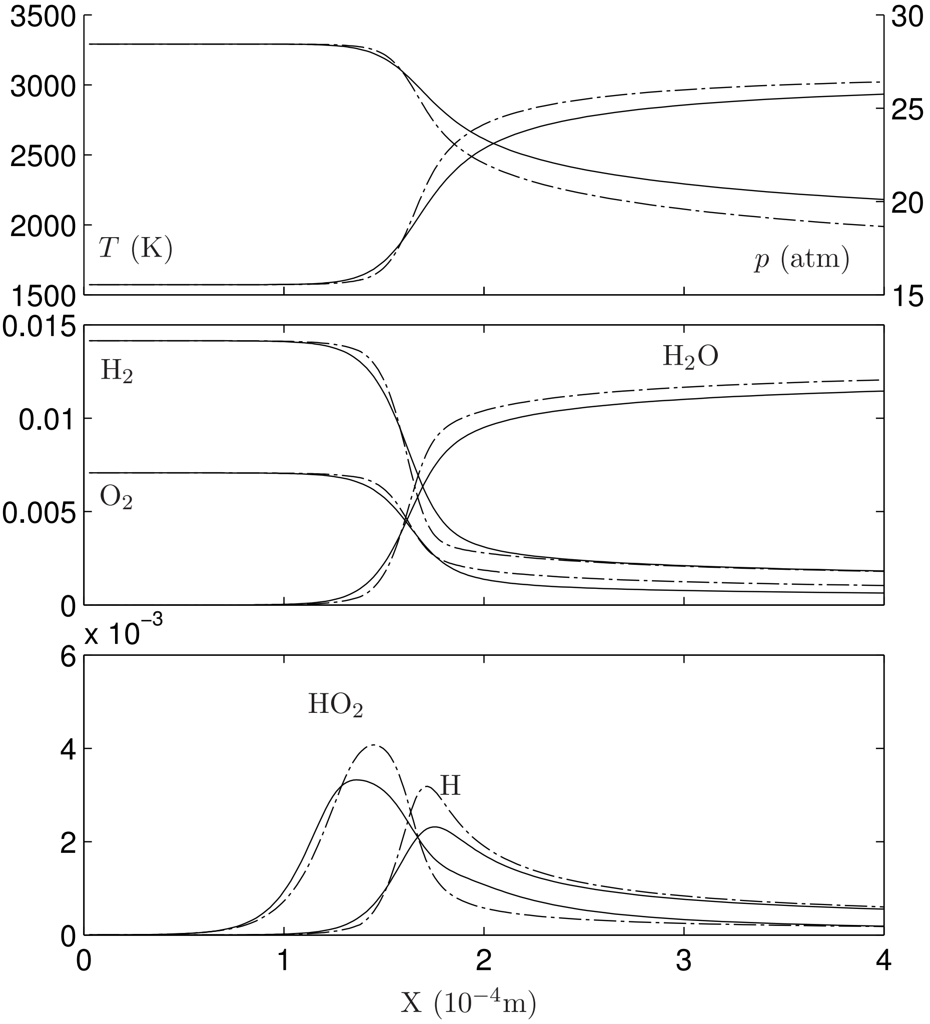

Figure 3.7: The variation with the distance from the shock of the pressure, temperature and species mole fractions in a Chapman-Jouguet detonation propagating in a stoichiometric hydrogen-air mixture with $p = 1$ atm and T=300K as obtained with the detailed 21-step chemistry (solid curves) and with the 3-step reduced mechanism with corrected rates (dot-dashed curves).

CHAPTER 4

Simulation of a supersonic hydrogen-air autoignition-stabilized flame using reduced chemistry

The purpose of the present chapter is twofold. The first objective is to complete the validation of the three-step reduced chemistry proposed in Chapters 2 and 3, in the context of turbulent autoignition. To this end, a supersonic lifted co-flowing hydrogen-air diffusion flame stabilized by autoignition is chosen as test case. Given that the flame involves autoignition, diffusion and premixed combustion processes under intensely fluctuating flow conditions, it is a challenging test case for the three-step chemistry. This objective is tackled in the first two sections of the chapter.

Systematic post-processing of such unsteady three-dimensional lifted flame simulations to analyze flame stabilization is a challenge [38–43] because the instantaneous stabilization position typically fluctuates rapidly. Moreover non-premixed combustion, premixed combustion and autoignition processes can contribute simultaneously to stabilization. The last section presents a new explicit diagnostic to readily identify regions where autoignition is occurring, based on joint use of quantities introduced in Chapter 3. The diagnostic is fully explicit, which makes it computationally cheap, and easily accessible both at the post-processing stage and in run-time.

4.1 Description of the supersonic flame

The supersonic burner (SSB) of the NASA Langley Research Center [52] sketched in Fig. 4.1 and with operating conditions given in Table 4.1, produces an axy-symmetric flame from a sonic pure hydrogen cold jet surrounded by a largely supersonic (Mach 2) jet of hot products generated by a lean combustor. Massive convection leads to a large induction zone, preceding the flame stabilization area, about 6 cm from the nozzle exit, or 25 D (D=2.36 mm, is the diameter of the inner hydrogen jet). Spark schlieren and visual photographs were made of the flame [52], some of which are shown in Fig. 4.2, illustrating the instantaneous H_2 jet and coflow, as well as the mean flame shape.

The work of Cheng et al. [52] with the SSB provides accurate experimental data on the dynamics, the mixing and the combustion conditions of this supersonic lifted flame. Through combining ultraviolet spontaneous vibrational Raman scattering and laser-induced predissociative fluorescence techniques, they obtained simultaneous instantaneous measurements for temperature and species concentrations (main species and OH radical). Measurements are reported as radial profiles at distances x/D = 0.85, 10.8, 21.5, 32.3, 43.1, 64.7 and 86.1 from the burner exit and as scatter plots of temperature and species at several selected locations.

4.1.1 Numerical set-up

Simulations of the supersonic flame described above are carried out with the Navier-Stokes equations solver AVBP [53], developed at Centre Européen de Recherche et de Formation Avancée en Calcul Scientifique (CERFACS). AVBP is an unstructured parallel compressible solver designed for Large Eddy Simula-

Dimensions	
Air mass flow rate (±2%)	0.0735 kg/s
H_2 mass flow rate (±2%)	0.000173 kg/s
O_2 mass flow rate (±3%)	0.0211 kg/s
fuel mass flow rate (±3%)	0.000362 kg/s
Nozzle exit inner diameter	17.78 mm
Fuel injector inner diameter	2.36 mm
Fuel injector outer diameter	3.81 mm
Vitiated Air Exit Conditions	
Pressure	107 kPa
Temperature	1250 K
Mach number	2.0
Velocity	1420 m/s
O_2 mole fraction	0.201
N_2 mole fraction	0.544
H_2O mole fraction	0.255
Fuel Exit Conditions	
Pressure	112 kPa
Temperature	540 K
Mach number	1.0
Velocity	1780 m/s
H_2 mole fraction	1.0

Table 4.1: Supersonic burner nominal operating conditions [52].

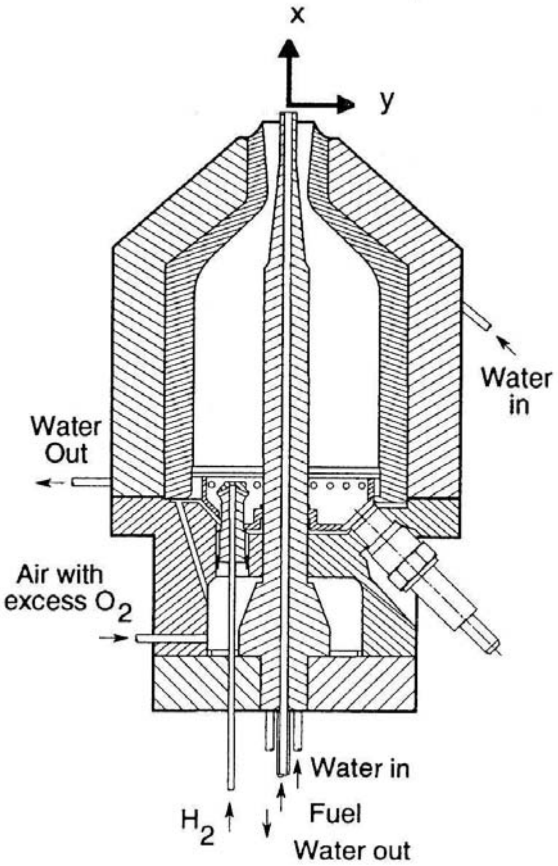

Figure 4.1: Sketch of the supersonic burner.

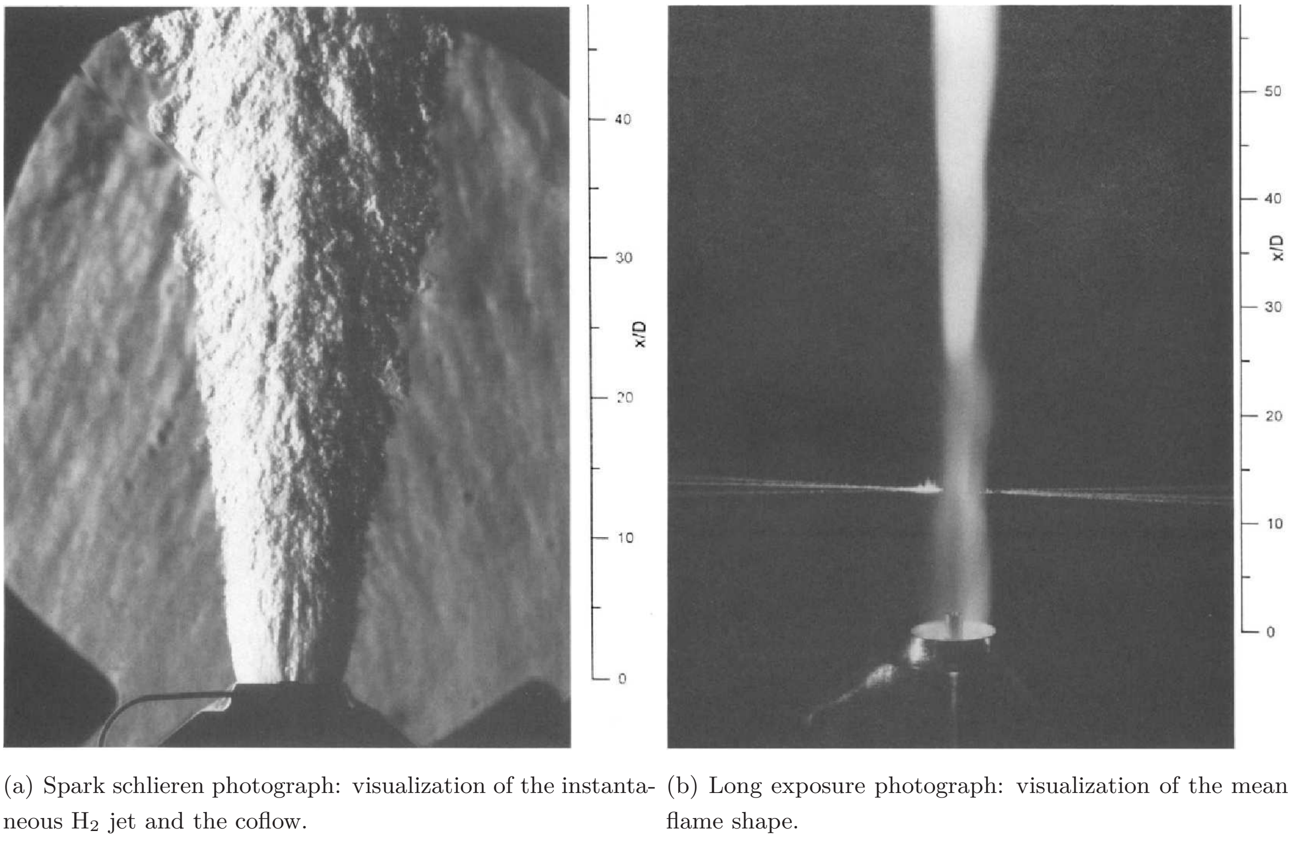

(a) Spark schlieren photograph: visualization of the instantaneous H_2 jet and the coflow.

(b) Long exposure photograph: visualization of the mean flame shape.

Figure 4.2: Photographs of the supersonic flame in [52].

tion (LES) or Direct Numerical Simulation (DNS) of combustion systems. The balance equations for mass, momentum, energy and species mass fractions are explicitly integrated with a 3^{rd}-order scheme in space – Taylor Galerkin – and time – Runge-Kutta. To handle shocks in the supersonic jet the strategy proposed in [54] was followed: the sub-grid scale turbulent viscosity μ_t is modeled through a standard Smagorinsky model, a centered numerical scheme is chosen and a hyperviscosity like in [55] is used for capturing shocks. A subgrid scale diffusivity is introduced for chemical species via a turbulent Schmidt number equal to 0.6 (molecular diffusivity is different for each species, and specified by the Schmidt numbers : H_2: 0.28; O_2: 0.99; H_2O: 0.77; H: 0.17; O: 0.64; OH: 0.65; HO_2: 0.65; H_2O_2: 0.65; N_2: 0.87). No sub-grid turbulent combustion model is used, on the grounds that the resolved scales control fully the combustion processes in the region of interest for this study, that is, in the stabilization region. More details on this are given below in Sec. 4.1.3.

A number of groups have simulated the main characteristics of this supersonic flame using Eulerian and Lagrangian Monte Carlo Probability Density Function (PDF), or flamelet models [56–60], in a Reynolds Averaged Navier-Stokes (RANS) context. The boundary conditions have proven to be one of the most sensitive elements in simulating this flame. The experiments in [52] provide detailed data on the fluid mechanical scales and on the flow composition at $x/\mathrm{D}=0.85$, a very short distance from the nozzle exit compared to the 25D experimental flame stabilization lift-off height. This location was chosen in this work as the inlet boundary and velocity, temperature, pressure and main species concentrations profiles – consistent with the experimental data and the nominal flow rates of the burner given in Tab. 4.1 – are imposed as boundary condition. Homogeneous isotropic turbulence is then superimposed in the vitiated air coflow, with a rms velocity of 300 m/s, consistently with the 20% fluctuations in velocity at the jet exit reported in the experiment [52].

The computational domain is a hemisphere corresponding to $x \geq 0.85D$ and of radius 10000D, and the fully unstructured grid consists of 6.6M tetraedric cells, with a minimum volume of $\Delta v = 8.10^{-13}\mathrm{m}^3$. The convex boundary on the sphere is an adiabatic wall, sufficiently far so that no wave reaches it during the simulation time.

4.1.2 Reaction mechanisms for hydrogen combustion

The main objective of the work presented in this chapter is to test, in a turbulent case, the behavior of the three-step mechanism for H_2-air combustion developed in Chapters 2 and 3 by comparing it to the well-validated [4] 21-step detailed chemical-kinetic mechanism consisting of the steps listed in Tab. 2.1.

In order to understand the effect of the correction proposed in Sec. 3.4, to study the numerical stability of the associated modification criterion, described in Sec. 3.5, and to assess the accuracy of the three-step mechanism, the simulation of the supersonic flame was performed thrice, using the detailed San Diego chemistry, the reduced chemistry with the correction described in Sec. 3.4 ($\omega_{\mathrm{I}}^*/\omega_{\mathrm{I}} = \omega_{\mathrm{II}}^*/\omega_{\mathrm{II}} = \omega_{\mathrm{III}}^*/\omega_{\mathrm{III}} = \Lambda$), and the reduced mechanism without the correction.

4.1.3 Physical scales and mesh requirements

The experiments show that the flame anchors in a flow of mean velocity $\overline{u} = 1200\mathrm{m/s}$, which is hundreds of times the laminar flame speed of a hydrogen/air stoichiometric premixed flame. Even with a turbulence level of 20%, it is clear that the flame cannot be stabilized through a propagative edge flame, because the flow velocity is at least ten times higher than the deflagration speed. Instead, the flame of the present study is stabilized by autoignition of the mixing layer between the cold hydrogen jet and the hot vitiated air coflow.

The physical scales associated with the autoignition process are evaluated from a preliminary computation, in laminar conditions, in order to estimate the mesh resolution requirements in the turbulent computation. The transient evolution of a one-dimensional mixing layer of cold H_2 and hot vitiated air with conditions for composition and temperature identical to those of the supersonic flame, given in Tab.4.1 was computed using the NTMIX code[48] with detailed chemistry and complex transport as in [49]. Autoignition occurs at the most-reacting mixture fraction f_{mr}, leading to the formation of two premixed fronts that leave behind a trailing diffusion flame [10]. The temporal triple-flame structure obtained using detailed and reduced chemistry is presented in Fig. 4.3. Also shown are lines corresponding to the evolution of the stoichiometric and most-reacting mixture fraction location (f_{st} and f_{mr}). The mixture fraction f is defined as

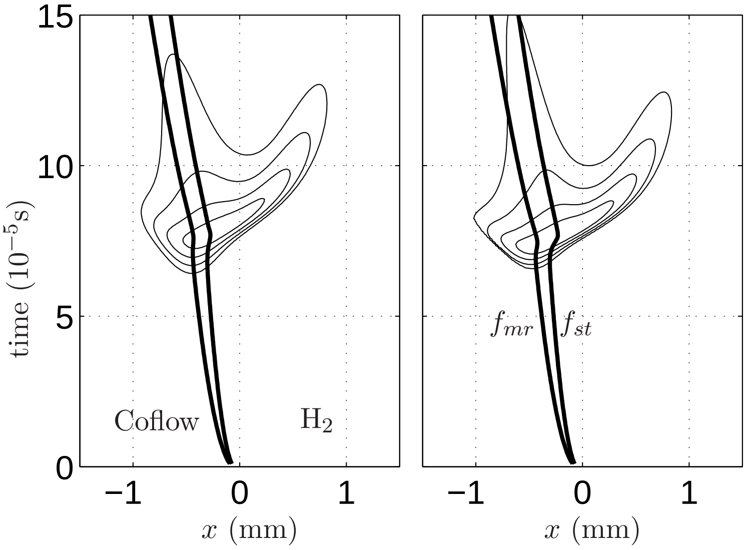

Figure 4.3: Isocontours of heat release rate corresponding to $2^n \times 10^9$J.m^{-3}.s^{-1} for $n = 1$ up to $n = 4$ in the transient one-dimensional mixing layer between the fuel and the vitiated air, with conditions given in Tab. 4.1, as obtained with the detailed chemistry (left plot), and with the three-step reduced chemistry with modified rates (right plot). The black lines indicate the location where $f = f_{st}$ (stoichiometry) and $f = f_{mr}$ (most-reacting).

$$f = \frac{Z_H - Z_{H,coflow}}{Z_{H,fuel} - Z_{H,coflow}}. \tag{4.1}$$

Here, Z_H is the hydrogen elemental mass fraction in the mixture,

$$Z_H = \sum \mu_{i,H} Y_i, \tag{4.2}$$

where $\mu_{i,H}$ denotes the mass proportion of atomic hydrogen in the species i, and Y_i are their mass fractions. Figure 4.3 shows that autoignition occurs after a time $t_{ind.} \approx 6.10^{-5}$s, after which the flame ignites and splits into three branches : a lean, spatially decaying premixed flame (left branch), a diffusion flame anchored around the stoichiometry f_{st}=0.03 and a rich, spatially decaying premixed flame (right branch). The time scale associated with the premixed branches is denoted $t_{fl.}$ and estimated $\approx 4.10^{-5}$s.

Considering a mean jet velocity $\overline{u} = 1200$m/s, the induction zone should extend over a region of $t_{ind.}.\overline{u} \approx$ 30D, and the premixed branches over $t_{fl.}.\overline{u} \approx$ 20D. In this stabilization region ($0 < x/\mathrm{D} < 50$), mixing is a key phenomenon and must be captured from the largest to the smallest scales, i.e. in a DNS-like approach. A very refined mesh was then used in the near burner area, $0.1 < \Delta x < 0.4$mm, was imposed for $x/\mathrm{D} < 40$, to ensure that mixing and ignition are well resolved, and that there is no need for subgrid turbulent combustion modeling in this area. The ratio of the minimum grid spacing to the experimental integral and Kolmogorov scales are then respectively of the order of 0.02 and 10 according to the experiments by Cheng et al. [52]. Pictures of the refined mesh are included in Fig. 4.4. In Fig. 4.4(a), one may seize the ratio of the domain size over the flame dimensions, as the end of the bottom section of the hemisphere is visible in the background. A posteriori tests confirming the adequacy of the mesh resolution are presented in Sec. 4.2.4.

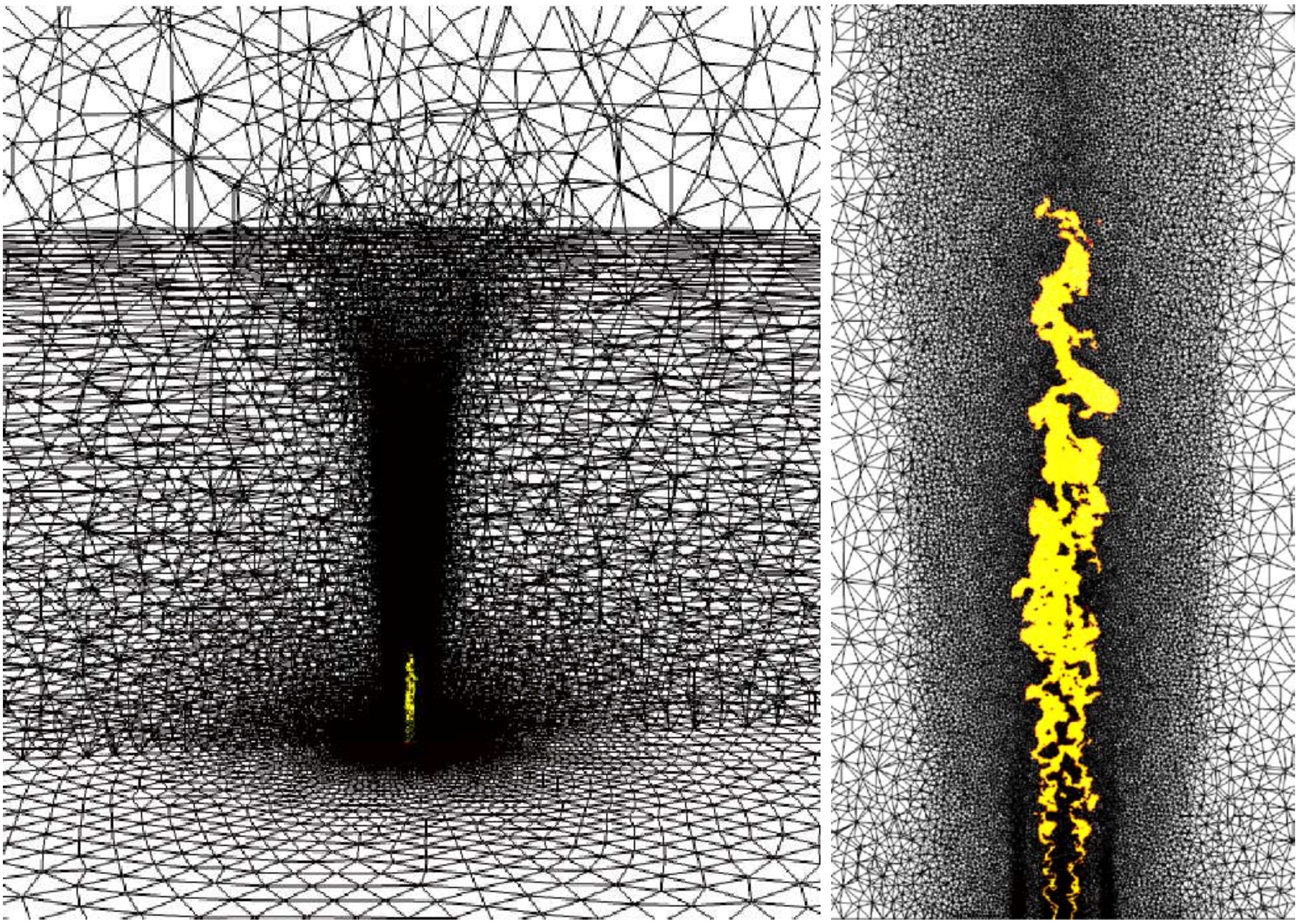

(a) View of the hemispherical domain.

(b) Grid resolution in the flame.

Figure 4.4: Illustration of the grid. In color are represented the zones of interest in the flame (corresponding to a certain threshold on the reactivity as introduced in Sec. 4.3).

Further downstream, the absence of a sub-grid turbulent combustion model will lead to an under-resolution of the diffusion flame. This does not imply numerical instabilities, as species and temperature gradients are controlled by the resolved flow. As the flame stabilization is the result of an autoignition process, and not an upstream propagation equilibrated by convection, the lack of subgrid model in the diffusion flame cannot affect the flame position.

As for the time resolution, the time step is limited by the smallest cell size and the fastest acoustic propagation speed $u + c$, u being the flow velocity, and c the sound speed, using a Courant-Friedrichs-Lewy criterion of 0.7. The resulting time-step is close to 2.10^{-8}s, which is at all times below any chemical-kinetic time scale.

4.2 Results

Computations were performed on a HP AMD cluster with 20.3 peak Tflops/s at CERFACS, using up to 120 cores.

4.2.1 Qualitative results

Figure 4.5 presents the instantaneous and mean temperature and HO_2 mass fraction fields obtained in the simulation of the supersonic flame, and allow a first qualitative comparison between the three chemical-kinetic mechanisms. The highly fluctuating nature of the flame can be observed on the left side plots in Fig. 4.5.a, showing the instantaneous temperature field. The left side plots in Fig. 4.5.b show that HO_2 appears well before the high temperature region, indicating that autoignition is starting at distances of about 20D from the burner exit.

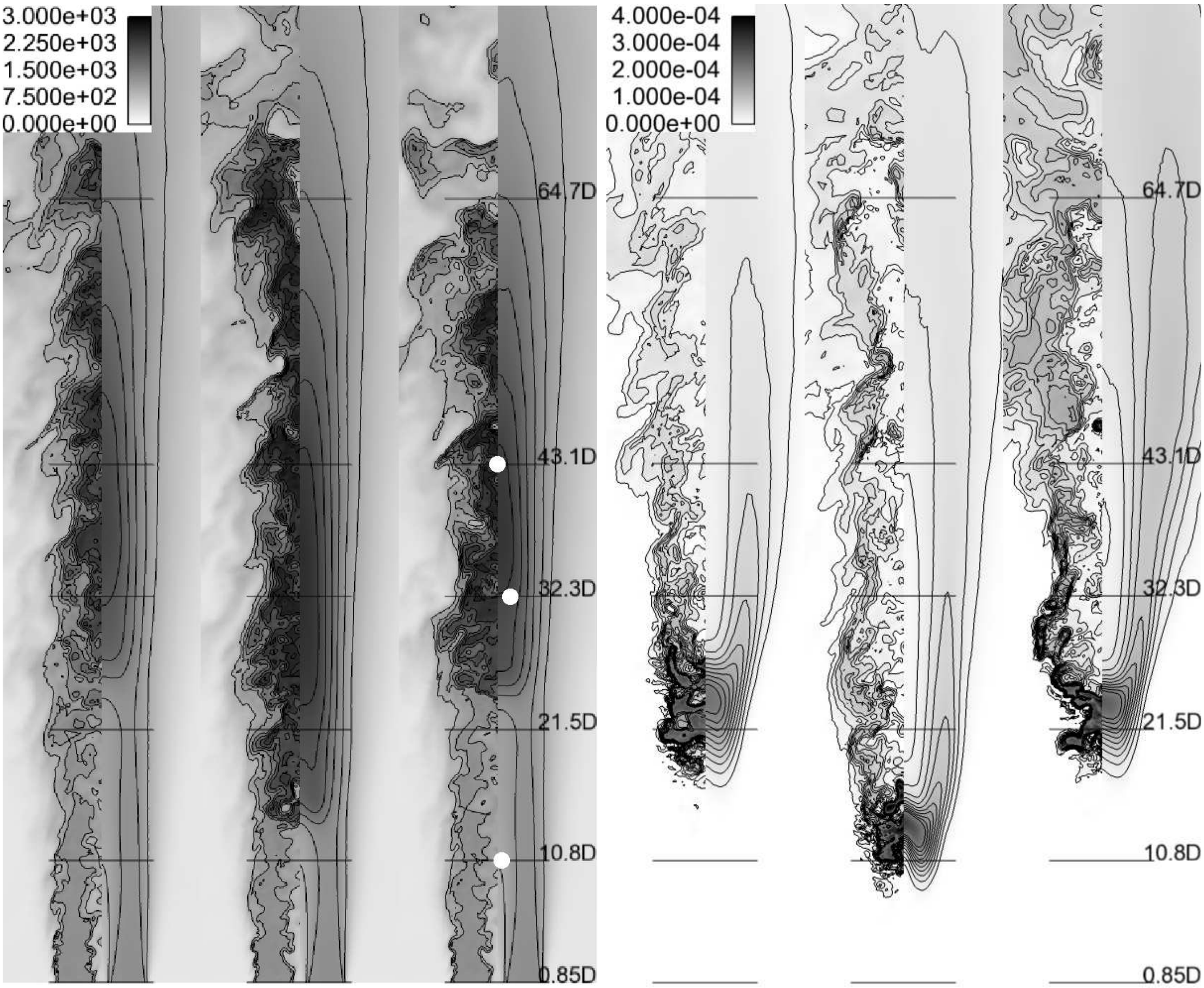

a. Temperature **b. HO_2 mass fraction**

Figure 4.5: Instantaneous (left side) and mean (right side) fields of a) temperature, b) HO_2 mass fraction, in the center plane of the flame. From left to right : detailed chemistry [4], reduced chemistry without the correction, and reduced chemistry with the modified rate. Contour lines are plotted every a) 250K from 1000K to 2500K; b) 10^{-5} from 2.10^{-5} to 2.10^{-4}. White dots in the right plot correspond to the location of scatter plots of Figs. 4.8 to 4.9(b).

Focusing on the mean temperature in Fig. 4.5.a, the first noteworthy result is that the detailed chemistry predicts with good accuracy the stabilization position of the flame at about 25D from the supersonic burner, as obtained in the experiment, validating the choice of the San Diego detailed chemistry [4] as a reference. Secondly, the reduced mechanism including the adequate modified rates ($\omega_{\mathrm{I}}^{*}, \omega_{\mathrm{II}}^{*}$ and $\omega_{\mathrm{III}}^{*}$) as presented in Chapter 3 predicts a very similar turbulent flame: the stabilization position, and the instantaneous and mean temperature and HO_2 radical mass fraction fields are very similar to those obtained with detailed chemistry.

Finally, the reduced mechanism without correction (middle pictures in Figs. 4.5.a and 4.5.b) expectedly results in a large under-prediction of the stabilization height, about 40% shorter. Besides, the shape of the mean flame base indicates that this mechanism predicts a leaner autoignition, which is consistent with the laminar results presented in Chapter 3. The inclusion of the correction of the reaction rates in the reduced chemistry changes drastically the stabilized flame, both in position and shape, indicating again that autoignition is the key mechanism in this flame stabilization.

4.2.2 Comparison with experiment

A quantitative comparison of the flames obtained in the three simulations is presented in Fig. 4.6. It represents profiles for mean values and rms fluctuations of the temperature, mole fractions of main species H_2, O_2, H_2O, and radical HO_2 mole fraction along the flame axis, as obtained with the detailed chemistry, the reduced chemistry, and the reduced chemistry without correction. Some experimentally measured points, extracted from radial profiles, are also included. They were obtained by interpolating at y=0 the radial profiles reported in [52]. Because of the asymmetry of the experimental radial profiles (see for instance the asymmetric temperature profiles in Fig. 4.7.c), this interpolation does not necessarily correspond to the axis of the flame. The SSB, depicted in Fig. 4.1, shows a short combustion chamber fueled asymetrically by the hydrogen and oxygen injectors, followed by a short convergent divergent nozzle. The resulting flow is expected to be more asymmetric than the present CFD inlet conditions, which explains the deviation of the numerical results and experiments in these plots. As will be seen below, numerical and experimental radial profiles show a much better agreement.

Table 4.2 shows the lift-off height in D units, computed as the position of the maximum temperature gradient of the three mean temperature profiles in Fig. 4.6. These values confirm that the reduced mechanism without correction predicts the lift-off height with an error of more than 40%, while the introduction of the correction reduces the error to about 5%. In the remainder of the discussion, only the detailed mechanism and the reduced mechanism including the adequate correction will be considered.

	Lift-off height	Relative error
Detailed chemistry	26.12	0
Reduced chemistry	24.73	-5.35%
No correction	14.55	-44.5%

Table 4.2: Stabilization position in D units, as obtained with the detailed chemistry[4], the reduced mechanism, and the reduced mechanism without the correction. Experiments measure stabilization at 25D.

The reduced chemistry reproduces with good accuracy the mean and rms fluctuations profiles of all species predicted by the detailed chemistry. This is even true for the hydroperoxyl radical HO_2 (bottom plots in Fig. 4.6), which shows outstanding agreement in the induction zone, up to about x/D=20.

Figure 4.7 includes experimental and numerical radial profiles for mean values and rms fluctuations of the temperature, mole fractions of main species H_2, O_2, H_2O and radical HO_2 mole fraction at axial distances x/D=10.8, 21.5, 32.3 and 43.1. These axial locations are indicated in Fig. 4.5. for reference.

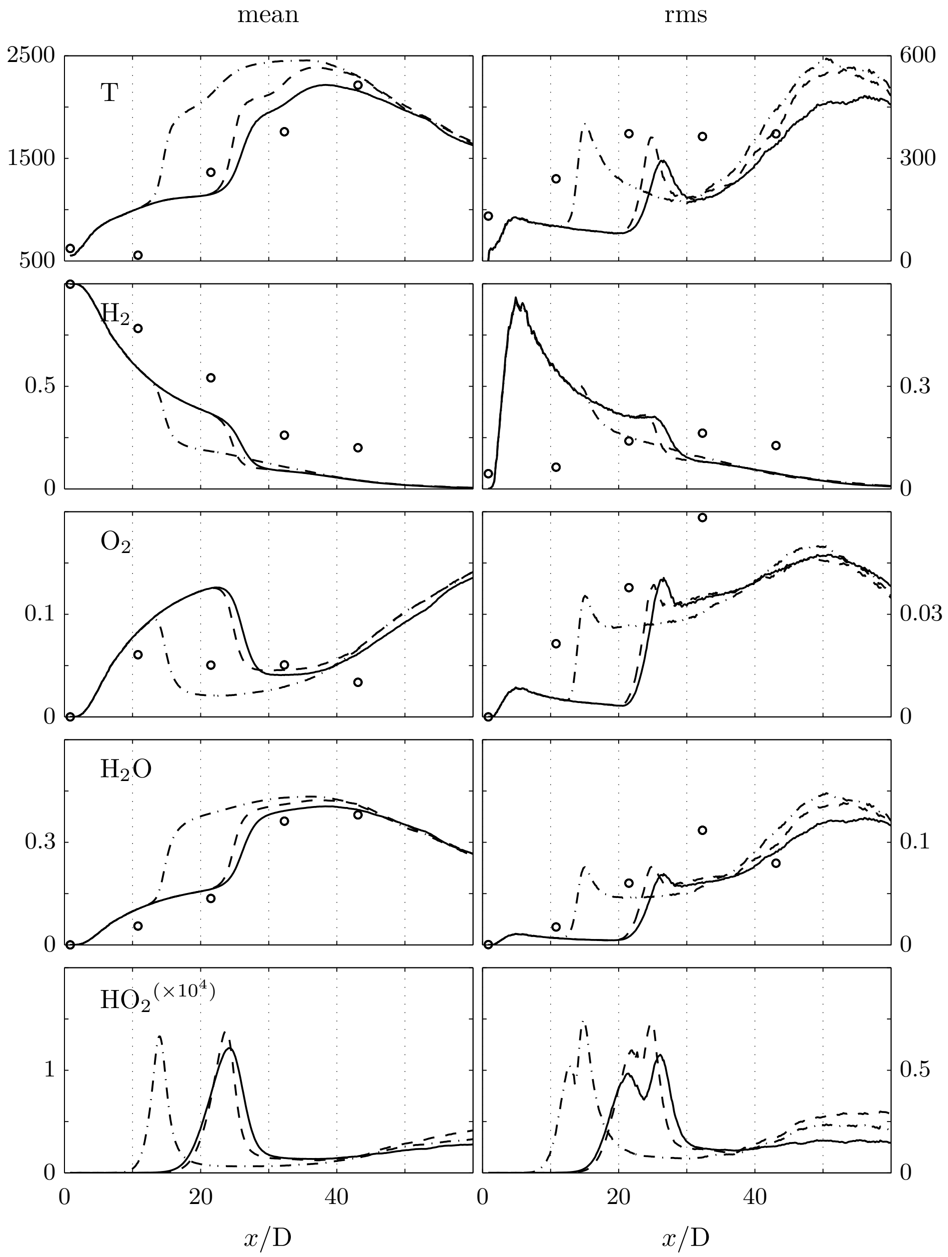

Figure 4.6: Mean and rms profiles for the temperature and mole fractions of selected species along the flame axis, as obtained with the detailed chemistry [4] (solid curves), with the reduced mechanism (dashed curves), with the reduced mechanism without correction (dot-dashed curves), and in the experiments [52] (circles).

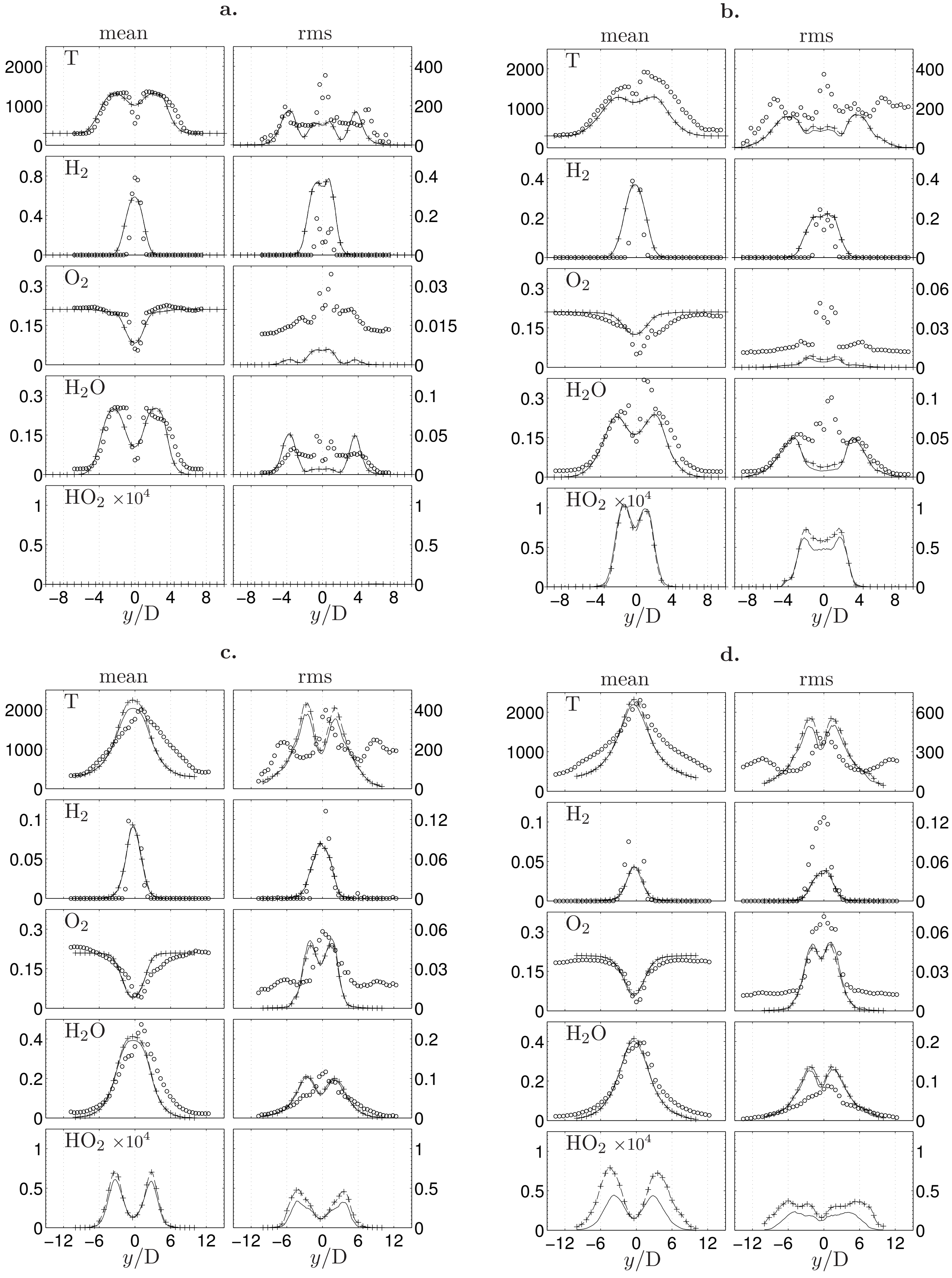

Figure 4.7: Mean and rms profiles for the temperature and mole fractions of selected species at (a) x/D=10.8, (b) 21.5, (c) 32.3 and (d) 43.1, as obtained with the detailed chemistry [4] (solid curves), with the reduced mechanism (dashed curves and crosses), and in the experiments [52] (circles).

Mean and rms profiles in the induction zone, corresponding to axial distances x/D =10.8 and 21.5, and represented in Figs. 4.7.a and 4.7.b, are identical for the main species and temperature with the detailed and the reduced chemistry. They are also very similar for HO_2 mole fraction. Moreover, the agreement with the experimental mean values is very reasonable. Rms fluctuations in the simulation are comparable in magnitude to the experimental measurements, even if the central area peaks are not well reproduced.

Figures 4.7.c and 4.7.d show radial profiles for the same quantities at x/D=32.3 and 43.1, inside the stabilized flame. Mean values of the main species are still in good agreement for the detailed and the reduced mechanism, with small overestimations of HO_2 mass fraction in the diffusion flame. The two peaks observed in the numerical rms profiles in Figs 4.7.a and 4.7.b slowly merge into one as distance from the nozzle increases, giving a better agreement with the experiment.

To further compare the numerical results and the experiments, scatter plots of temperature and species mole fractions are presented in Figs. 4.8 and 4.9. The left plots correspond to simultaneous experimental measurements at three locations [x/D, y/D]=[10.8, -0.65], [32.3, 1.1] and [43.1, 0] and the right plots to instantaneous values from the simulation with the reduced chemistry over 0.6ms at the same locations. The plots also show lines, representing the limits of pure mixing between the reactant streams (mixing line), and of adiabatic equilibrium after combustion (equilibrium line). Stoichiometry corresponds to a mixture fraction value $f_{st} = 0.03$.

The first scatter plots, in Fig. 4.8, correspond to the probe located at x/D = 10.8 and y/D = -0.65, in the induction zone, far from the ignition region (see Fig. 4.5). As expected, the temperature and main species are all very close to the mixing line, indicating that no reaction has occurred yet. This good agreement validates the resolution of mixing at large scales, a sine qua non condition for the good prediction of the lift-off height. Some traces of OH, appear in the experiment at very low mixture fractions, which correspond to products of a lean pre-combustion in the SSB, as reported in the experiment, and not to the onset of ignition.

For the next scatter plots, in Figs. 4.9(a) and 4.9(b), probes are located inside the stabilized flame (see Fig. 4.5). The species and temperature progressively approach their adiabatic equilibrium level. The range of mixture fractions encountered at the second probe in Fig. 4.9(a), located in the flame, is fairly similar in the experiment and in the simulation ($f \in [0, 0.08]$ and [0,0.07] respectively). Agreement in the range of fluctuating f values is not as good at the last probe (Fig. 4.9(b)), but remains acceptable. Conditional averaging of the experimental and simulation scatter plots would show a good agreement, however, the scattering of the points in the vertical direction of these plots is noticeably different, as shown in Figs. 4.9(a) and 4.9(b). It is to be related to the lower rms fluctuations for temperature and species in the vicinity of the symmetry axis, as reported in Figs. 4.6 and 4.7. This is due to the choice of the injected turbulence (homogeneous isotropic), which does not describe the inhomogeneities produced by the splitter between the two jets. As a consequence, less fluctuations are found in this area compared to the experiment. This however seems to have a negligible impact on the global mixing (see Fig. 4.8). The quality of the simulated flow is then considered sufficient to study the impact of the finite-rate chemistry on flame stabilization.

We compare in Fig. 4.10 scatter plots of HO_2 mole fraction at x/D=20, y/D=0, (where autoignition seems to start according to Fig. 4.5) as obtained with the detailed and the reduced chemistry. This area preceding the stabilization point contains the most important variations for the hydroperoxyl radical, while all other quantities remain close to the mixing line, indicating the onset of autoignition close to the most-reacting mixture fraction $f \approx f_{mr} = 0.015$. The similarity between the detailed and reduced chemistries indicate that the latter captures the main autoignition mechanism.

Figure 4.11 includes the same comparison for the temperature and the mole fractions of H_2, H_2O and

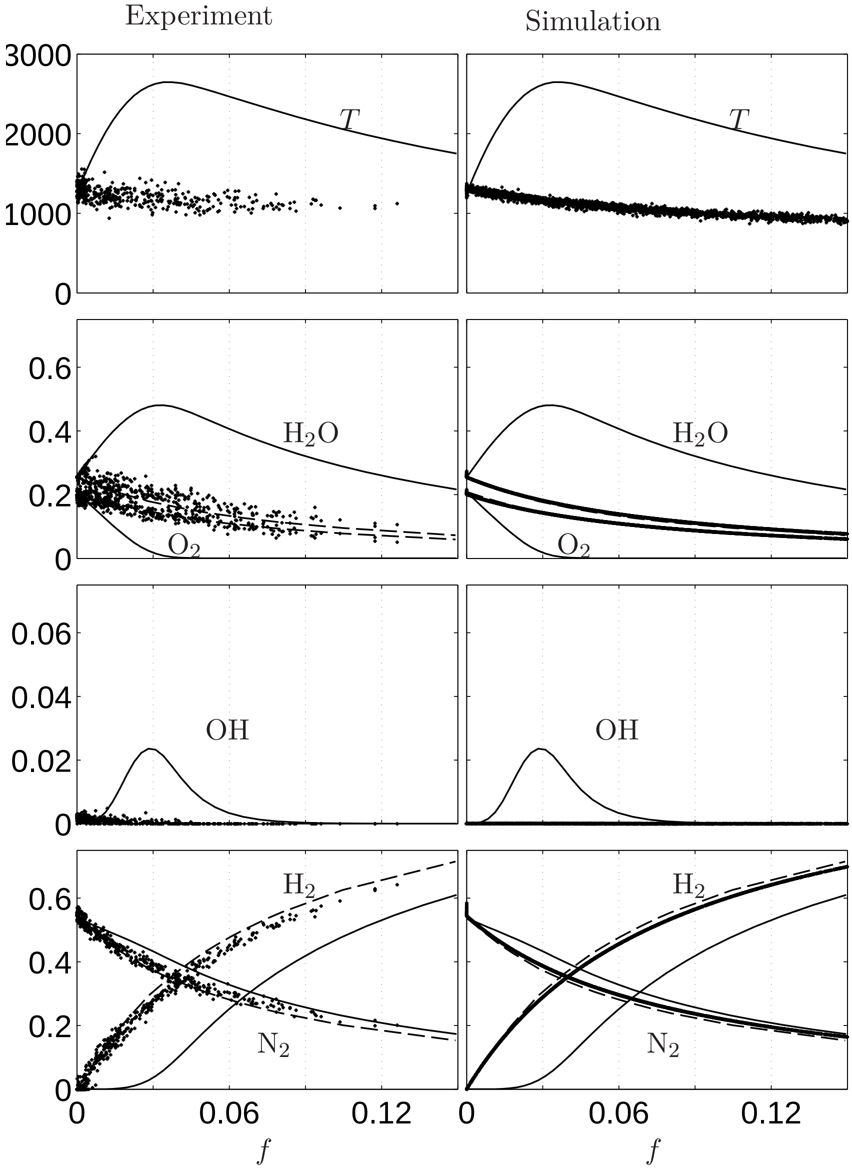

Figure 4.8: Scatter plots of temperature, main species mole fractions (H_2, O_2, N_2, H_2O), and OH mole fraction versus mixture fraction at x/D = 10.8, y/D= -0.65. Equilibrium (solid curve) and mixing lines (dashed curve) are also included. Left: Experiment. Right: Simulation.

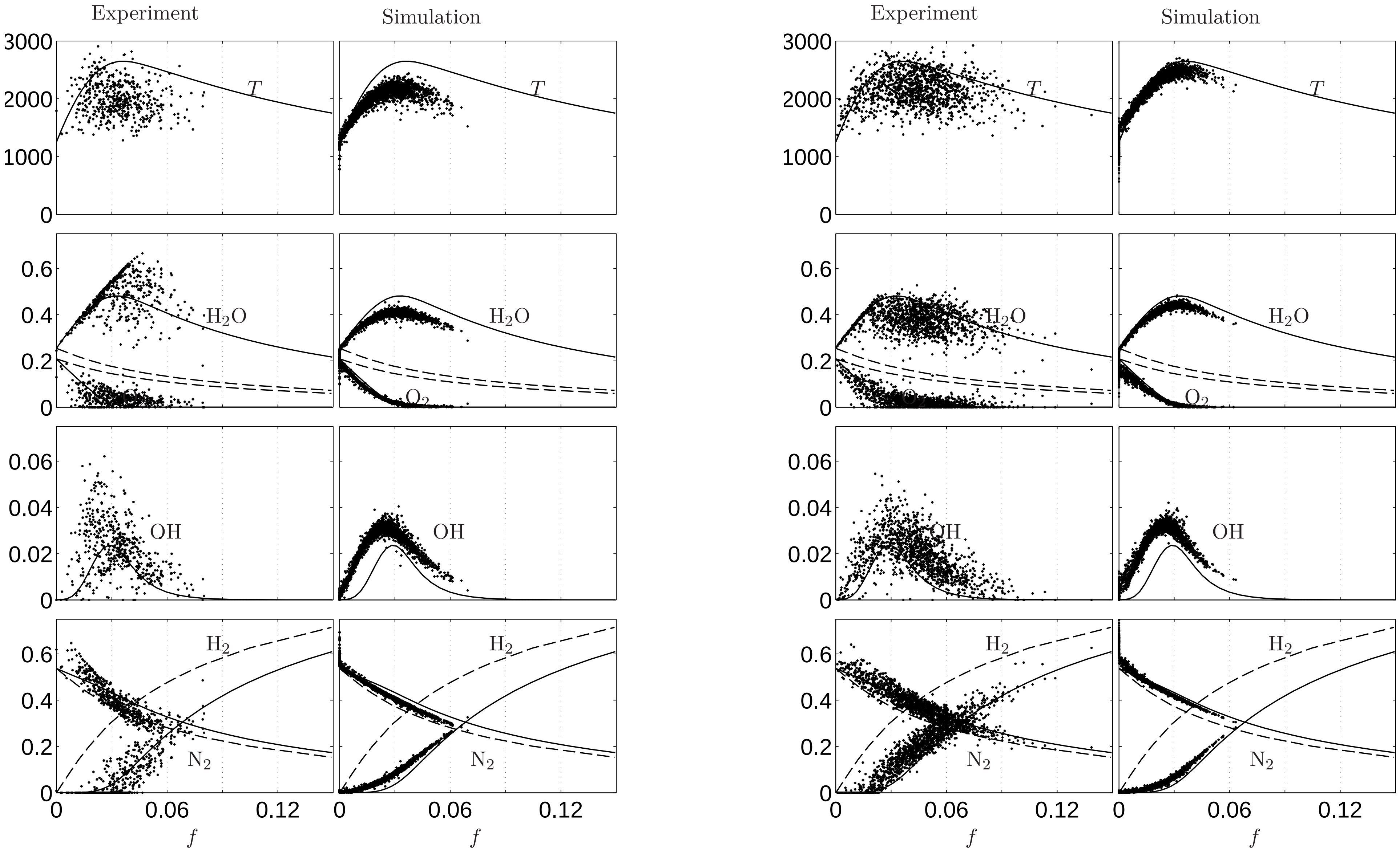

(a) Position : x/D = 32.3, y/D= 1.1.

(b) Position : x/D = 43.1, y/D= 0

Figure 4.9: Scatter plots of temperature, main species mole fractions (H_2, O_2, N_2, H_2O), and OH mole fraction versus mixture fraction. Equilibrium (solid curve) and mixing lines (dashed curve) are also included. Left: Experiment. Right: Simulation.

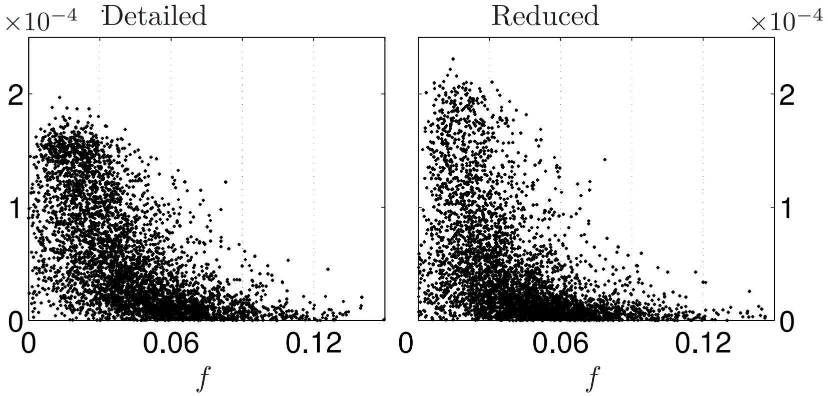

Figure 4.10: Scatter plots of HO_2 mole fraction versus mixture fraction at x/D = 20, y/D= 0. Left: detailed chemistry. Right: reduced chemistry.

OH in the mixture fraction space at [x/D, y/D]=[25, 0]. At this position, autoignition has occurred, and all species show intense fluctuations. Most of the hydroperoxyl has been consumed, triggering the chain-branching reactions characteristic of H_2 oxidation under these conditions.

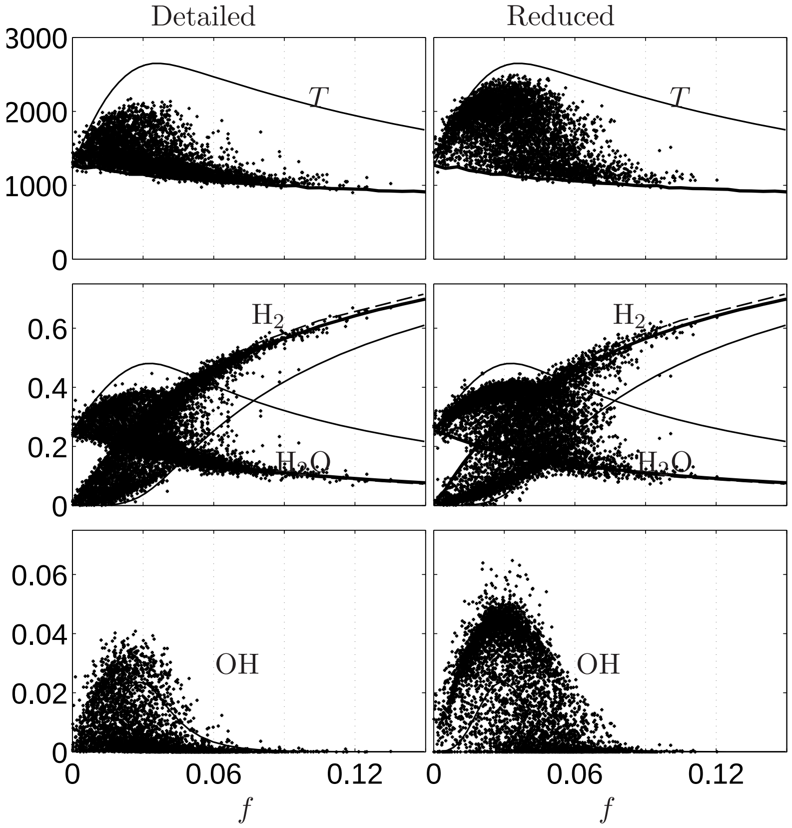

Figure 4.11: Scatter plots of temperature and selected species mole fractions (H_2, H_2O and OH) versus mixture fraction as obtained with detailed and reduced chemistry, at x/D = 25, y/D= 0. Equilibrium (solid curve) and mixing lines (dashed curve) are also included. Left: detailed chemistry. Right: reduced chemistry.

In Fig. 4.11, OH radical, absent from the reduced chemistry, was estimated using the appropriate steady state expression given in Eq. (2.4), showing a reasonable agreement with the detailed chemistry.

4.2.3 Discussion

The comparison of the shapes of the mean and rms profiles in the induction zone preceding the flame, shown in Figs. 4.6, 4.7.a and 4.7.b. indicates that the mixing layer between hydrogen and the hot coflow is not well reproduced in the simulation. A better strategy for the inlet boundary condition should be investigated, to account for the non-uniformity of the turbulence at x/D=0.85, and the species fluctuations due to the unsteadiness of the flow characteristics after the pre-combustion chamber. However, this does not influence the flame stabilization, which seems to be purely chemistry related.

A second discrepancy is that the experimental flame seems generally wider than the simulated flame. This error is recurrent in all recent simulations of this flame [56–61], and may be lessened by more realistic boundary conditions including, for instance, a realistic burner geometry.

The detailed and reduced chemistries predict mean values and rms fluctuations very similar for all main species, except in a very small area around 25D, as revealed in Fig. 4.11. This probe was purposedly located in the area between the two stabilization positions predicted by the detailed and the reduced chemistries (resp. at about 26D and 24.5D, as presented in Tab. 4.2), to evaluate the size of the largest possible errors.

However, the burnt gases maximum temperature is overestimated by about 150K, as shown in Figs. 4.6, 4.7.c and 4.7.d. This is a well-known drawback of using explicitly reduced chemical mechanisms: the selected subset of radicals has a strong impact in the evaluation of the specific-heat C_p, and thus on thermodynamics.

Besides these drawbacks, this flame simulation captures the correct physics, and is a good reference for studying the impact of the chemistry model, which is the objective of the present work.

4.2.4 Resolution in the stabilization region

No subgrid scale turbulent combustion model is used in the present simulations, that are considered DNS in the flame stabilization regions. This was justified a priori in Sec. 4.1.3, as a result of a very fine mesh resolution in the near burner region (from $x = 0$ to $x = 40$ D). This refined region should contain the area of interest for this study, estimated from laminar flame results to cover a region up to x/D=30 for autoignition and a region up to x/D=50 for the stabilization point. It can readily be seen from Figs. 4.5 and 4.12(b), that also in the turbulent flame case, the stabilization region is included in the well resolved area.

Additionally, an a posteriori test for the resolution in this region can be obtained by comparing the SGS turbulent viscosity μ_t and the laminar viscosity μ in this region. Figure 4.12(a) shows an instantaneous plot of the ratio μ_t/μ in the central plane of the simulation, in which contour lines of reactivity λ – a variable introduced in the next section – are superimposed. In the induction region, where mixing and autoignition occur, that is, in the highly reactive region where $\lambda > 10^5 s^{-1}$, the SGS turbulent viscosity is less than an order of magnitude larger than the laminar viscosity $\mu \approx 5.10^{-5}$ kg/m s. This shows that the turbulent structures in the induction area are well resolved.

Finally, the resolution issue has also been tested when examining the scatter plots in Figs. 4.8 and 4.9(a), for x/D≤40D. The fluctuations in the mixture fraction space f obtained in the simulation cover a similar range than the mixture fraction measured in the experiment, although some differences are observed. This means that the resolved scales in f represent the experimental fluctuations, and no SGS fluctuation model is needed. Further in the flame, after 40 D, for example in Fig. 4.9(b), a first hint of possible subresolution in f appears.

4.3 An explicit diagnostic for autoignition identification.

The hydroperoxyl radical HO_2 peaks typically in igniting mixtures, therefore it has been extensively used for detection and visualization of autoignition in lifted-flames [40, 42, 62]. However, HO_2 concentration also peaks in ignited mixtures near the fuel-rich reaction zones of flames [38]. Moreover, its concentration during

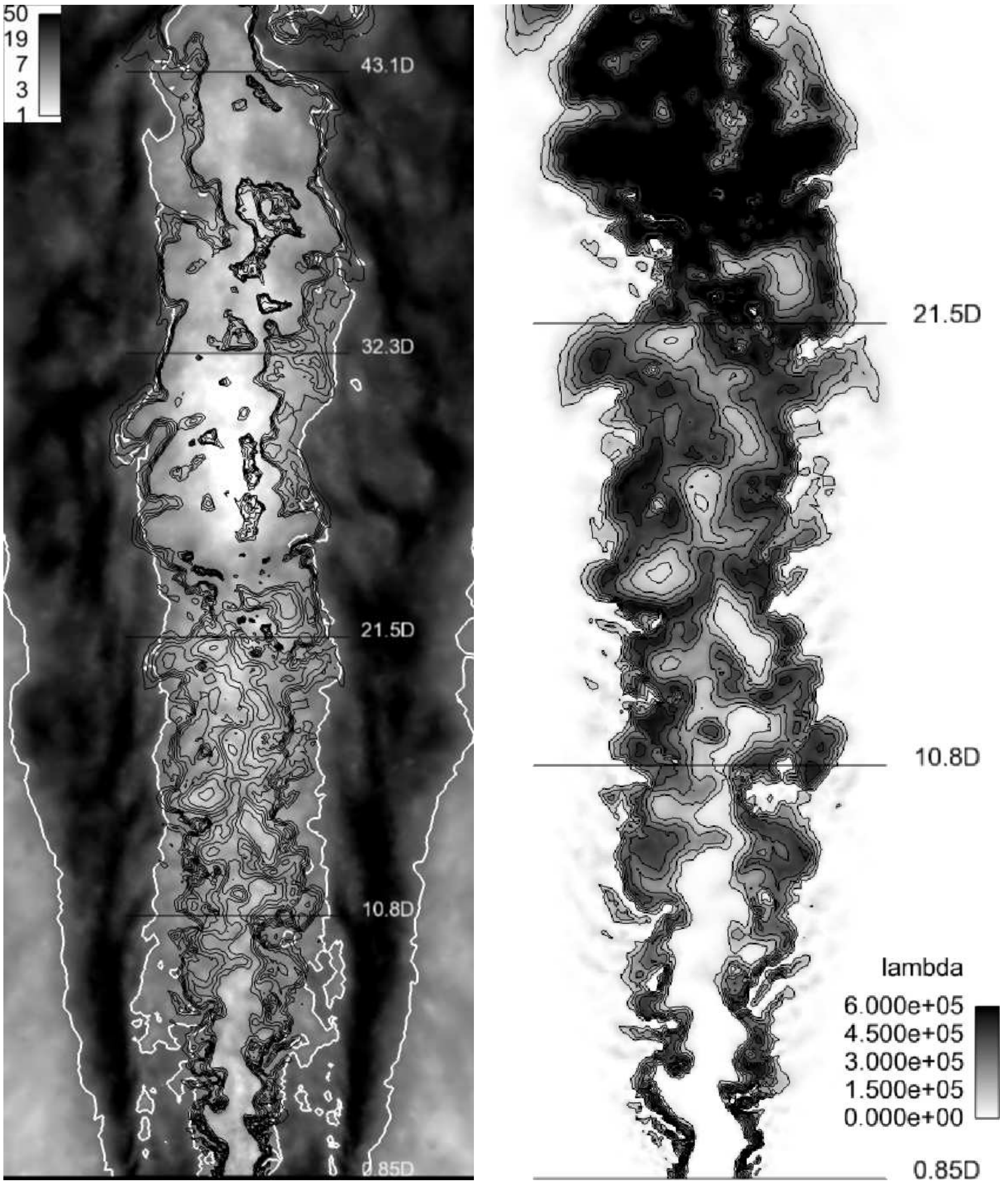

(a) (b)

Figure 4.12: (a) The ratio μ_{turb}/μ_{lam}, and isocontours of the reactivity $\lambda = k.10^5 s^{-1}, k = 1, 2, .., 5$ delimiting the autoignition region. The white line is situated at $\mu_{turb}/\mu_{lam} = 10$.
(b) Snapshot of λ, the reactivity of the mixture. Contour lines at $\lambda = k.10^5\mathrm{s}^{-1}$, k=1,2,..,5.

autoignition processes changes drastically with local conditions, and can hinder the detection of certain autoignition spots when several local maxima (in HO_2 level) are simultaneously present.

This section shows a possible use of the analysis of high-temperature autoignition presented in Chapter 3 for a new explicit diagnostic to identify autoignition at the post-processing stage.

4.3.1 Reactivity of the mixture

The chemical explosive mode analysis (CEMA) proposed by Lu et al. [38, 63], and derived from the computational singular perturbation (CSP) method [26], is a method to quantify the reactivity of the mixture at each point in the computation of a flame. Chemical explosive modes are associated with positive eigenvalues of the Jacobian of the chemical source term. In [38], explosive modes are detected by computing numerically the eigenvalues of the full Jacobian at every point of the computational domain. Here we propose to use to that effect the explicit expression for the eigenvalue associated to autoignition chemistry derived in Chapter 3, and given by Eqs. (3.7) and (3.9).

This simple expression for λ, depending only on the local reactant concentrations and temperature, gives an accurate estimation of the local non-premixed potential reactivity. It can also be used to estimate a priori the most-reacting mixture fraction f_{mr} [10, 40, 49], which corresponds to the maximum value of λ in a mixture.

Note that λ is proportional to the inverse of the autoignition time in homogeneous conditions. It is possible to obtain explicitly the relation between λ and the autoignition time, by fully integrating the differential equations (3.2). The complete integration results in an additional logarithmic term (associated to the initiation term $\bar{\epsilon}$), which was not found to improve significantly the identification of the most-reacting mixtures in this case. The complete derivation of this additional term is given in Appendix A.

Figure 4.12(b) presents a snapshot of the instantaneous λ value in the supersonic flame simulated in this work. Given that λ depends only on the local temperature and concentrations C_{H_2} and C_{O_2}, and because these quantities barely change during induction, λ is approximately constant along the most-reacting mixture line, marking reactivity but not the actual occurrence of ignition. Autoignition occurs along this line after sufficient accumulation of HO_2 radical, which can be identified by a second variable, as presented in next section.

4.3.2 Autoignition progress

Figure 4.13 shows the evolution of λ, the temperature and selected species mole fractions in an isobaric homogeneous reactor with initial conditions close to those encountered in the induction zone of the supersonic flame (p=1atm., T=1200K, f=0.03). It shows that, as explained above, the concentration of H_2, O_2, H_2O, H, as well as the temperature and therefore the reactivity λ remain constant during the induction process.

The chemical steady-state parameter SS, defined as

$$SS = \frac{\mathrm{production\,rate}(HO_2) - \mathrm{destruction\,rate}(HO_2)}{\mathrm{production\,rate}(HO_2) + \mathrm{destruction\,rate}(HO_2)}, \tag{4.3}$$

was used in Chapter 3 as a means to detect autoignition and activate the correction in the three-step reduced mechanism. The evolution of SS during autoignition in the homogeneous reactor is included in the lower plot of Fig. 4.13. In the homogeneous autoignition process, HO_2 production starts by the initiation step $H_2 + O_2 \rightarrow HO_2 + H$. While the produced H radical is readily consumed by the third-body reaction $H + O_2 + M \rightarrow HO_2 + M$, producing more HO_2, HO_2 cannot be consumed by any of the reactants and SS remains by definition unity during this stage. As HO_2 radical accumulates, SS decreases, reaching

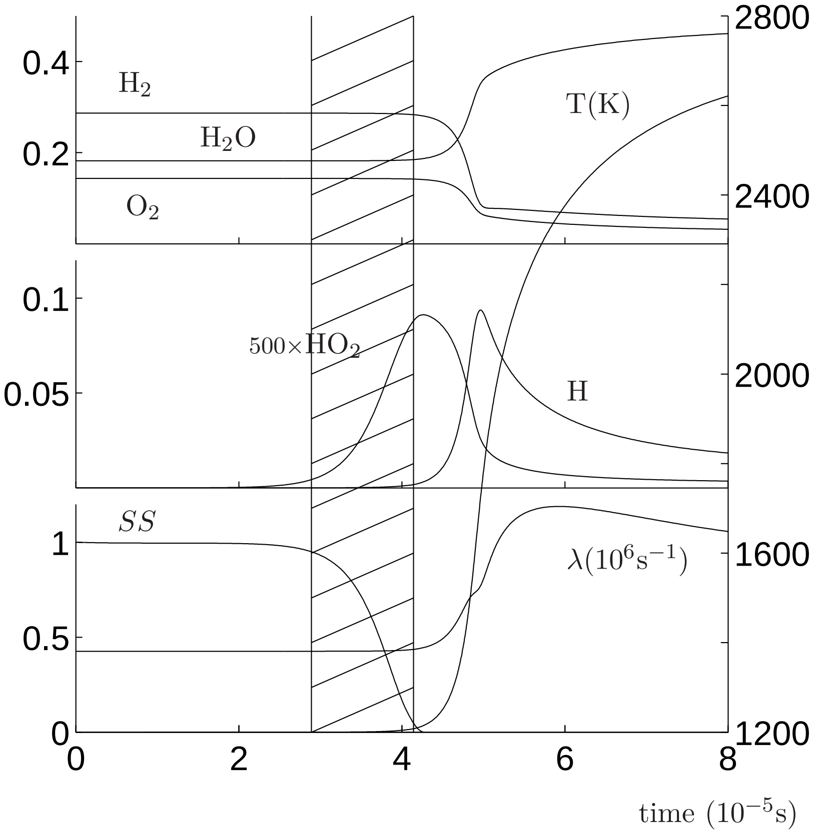

Figure 4.13: Evolution of the mole fractions of the main species (top), of H and HO_2 radicals (middle), reactivity λ and autoignition criteria SS (bottom), and temperature (full-height), during isobaric homogeneous autoignition. Vertical lines at SS=0.95 and 0.05.

0 when the HO_2 concentration attains its maximum value, triggering the autoignition. We can identify the autoignition period as the period when HO_2 progresses towards steady state, when SS decreases. In Fig. 4.13 two vertical lines are plotted at $SS_{max} = 0.95$ and $SS_{min} = 0.05$ to show that these two values can be chosen as delimiters of the autoignition region. Given the variations of SS (see Fig.4.13), the criterion depends very little on the choice SS_{min}, provided it is sufficiently small. However, the value of SS_{max} sets the sensibility of the criterion. It has to be small enough to be insensitive to numerical instabilities, but large enough to capture the induction region. Figures in the next section show that $SS_{max} = 0.95$ is a good choice.

4.3.3 Identifying autoignition

The stabilization of a turbulent lifted flame by autoignition is more complex than the homogeneous case described in Fig. 4.13. However, the discussion stands in reactive preheated turbulent mixtures, and the region where SS is between SS_{max} and SS_{min}, may be identified as the autoignition kernel.

Figure 4.14 represents on the left the area corresponding to $0.05 < SS < 0.95$ in a symmetry plane of the computed flame, and on the right the isosurfaces of SS=0.05 and 0.95 colored with the reactivity λ, computed from an instantaneous solution obtained with the reduced chemistry. As a reference, a gray temperature isosurface at T=1600K is also plotted, delimiting the burnt gases region. For visualization purposes the SS isosurfaces were restricted here to very reactive mixtures, eliminating points where λ is smaller than one third of its maximum value. The volume corresponding to $0.05 < SS < 0.95$, well separated from the burnt gases, can then be associated to the autoignition kernel.

Further study of this ignition kernel shows that it contains pockets of burnt gases, some of these pockets

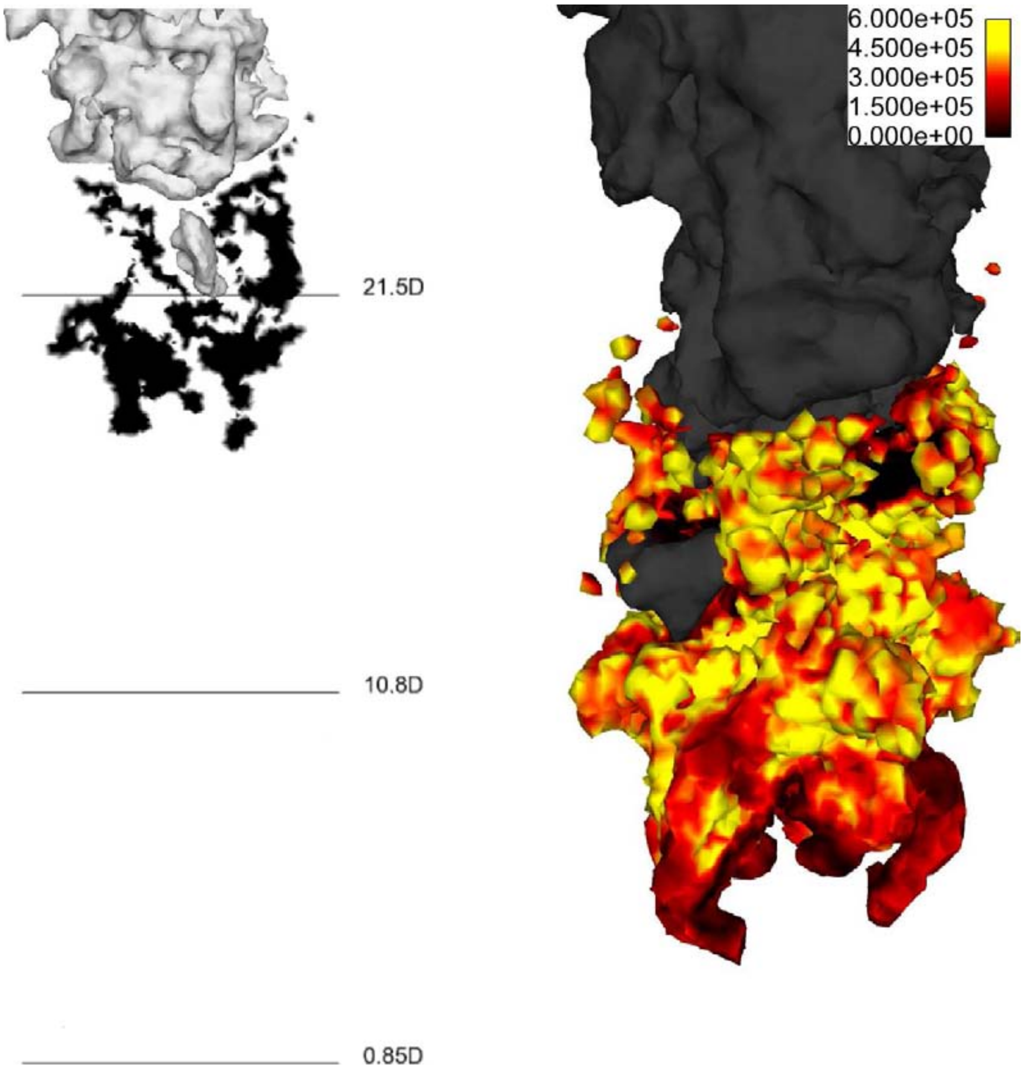

Figure 4.14: Left: in black, area corresponding to $0.05 < SS < 0.95$ in the symmetry plane. Right: zoom on the iso-surfaces $SS = 0.05$ and 0.95, colored with λ. In gray, temperature isosurface at T=1600K.

readily visible in Fig. 4.14. The strict separation of the burnt gases region and the autoignition kernel in Fig. 4.14 shows the efficacy of the method as an identifier of autoignition. Upstream, the autoignition kernel shows finger-like shapes, corresponding to the first detectable stages of autoignition. The coloring indicates that autoignition at this first spots occurs at maximum values of λ, that is, at the most reactive mixture, as should be expected.

4.4 Conclusions

We have presented simulations that validate the three-step reduced kinetic-chemical mechanism for H_2 oxidation in a turbulent, autoignition-stabilized flame. The use of the reduced chemistry results in a significant 20% speed-up compared to the detailed mechanism. Note that a speed-up of up to 45% was obtained using the reduced mechanism in a two-dimensional cartesian grid DNS solver [49]. Higher speed-up, of up to 75%, was obtained in transported PDF simulations. These differences in speed-up can be related to the different relative weight of chemistry integration in the cost of the three simulation methods.

The reduced mechanism for H_2 oxidation offers an attractive alternative to detailed chemistry as being computationally cheaper, and leading to practically identical results. Given that it was derived in a fully explicit manner, no tuning is necessary prior to a flame computation and it can be readily adapted to any

H_2-oxidation detailed chemistry available in the literature. The simulation using the reduced chemistry is as stable as the computation with the complete chemistry. The modification of the three global reaction rates introduced in Chapter 3 has proven to be an effective correction even in a turbulent simulation, and, more importantly, does not cause any particular numerical instability. Given the excellent results obtained with the reduced chemistry in laminar combustion, and its accuracy in this turbulent lifted flame, it is expected to give good results in other turbulent lifted flames as well, provided that autoignition occurs at conditions above the 2nd explosion limit.

Based on the quantities introduced in Chapter 3, an efficient autoignition detection methodology was presented in the last section. This method is computationally cheap, as all quantities are given by explicit formulas, and can be adapted to any H_2-air oxidation scheme, provided that the hydroperoxyl radical HO_2 is included in the mechanism. This includes also any H_2-dominated autoignition process, for instance that of syngas ($H_2 : CO$) mixtures (see Chapter 5). Also, it provides a simple way to evaluate the most-reacting mixture fraction in a mixing-layer. A similar method for more complex fuels should be further investigated, starting with a systematic simplification of the autoignition chemistry. The resulting system might not reduce to a simple quadratic expression, as for the hydrogen mixtures reactivity, or even be fully explicit, but it should remain cheaper computationally than analyzing the complete Jacobian of the chemical source term, whose complexity grows with the square of the number of species.

Additionally, this study enlightens the fact that the choice of the chemistry scheme in a simulation of an autoignition-stabilized lifted flame is essential, as an inappropriate choice can lead to errors on the flame stabilization-height of up to 50%.

The work presented in this chapter corresponds to the article "Simulation of a supersonic hydrogen-air autoignition-stabilized flame using reduced chemistry", submitted to Combustion and Flame [64].

CHAPTER 5

A four-step reduced mechanism for syngas combustion

Syngas is a coal-derived fuel of industrial interest in gas-turbines applications. Regardless of the coal type and gasification technology, the syngas mixture always contains significant amounts of CO and H_2 as the main reactive species along with diluents such as N_2, CO_2 and H_2O, while the hydrocarbon content, mainly CH_4, is in general very limited, especially when O_2-enriched gasification is employed. In deriving chemistry descriptions for syngas combustion, it therefore appears reasonable to focus on the chemistry of CO and H_2, neglecting the contribution of the hydrocarbon chemistry to the overall combustion process. Since the H_2/CO volume ratio in most syngas mixtures typically exceeds 0.25 and often takes on values that are of the order of 0.5 or above, it is found that the hydrogen chemistry plays a dominant role in syngas combustion, which therefore exhibits large burning rates and small autoignition times, comparable to those found in hydrogen combustion.

5.1 The reduced chemistry

The CO-H_2 submechanism of the so-called San Diego mechanism [4], comprising 30 elementary reactions among 11 reactive chemical species (CO, CO_2, HCO, O_2, H_2, H_2O, H_2O_2, O, H, OH and HO_2), will be used as a detailed-chemistry description for validation purposes.

Of the 21 steps in this mechanism that do not involve carbon atoms, a subset of twelve elementary steps, numbered 1-12 in Table 5.1, with the subscript f and b employed to denote forward and backward reactions was shown in Chapter 2 to give sufficiently accurate predictions for laminar burning velocities and induction times of H_2-air mixtures, as well as for structures and propagation velocities of detonations and strain-rate dependences of properties of H_2-air nonpremixed flames. Although not all of these elementary steps are essential for gas-turbine combustion (e.g., 8b and 9b need to be retained only if high-temperature equilibrium is to be described accurately, as occurs in detonations), no significant simplification follows from discarding any one of the less important rates, so that the following development employs all twelve reactions, as they appear in the table, for describing H_2 oxidation in syngas combustion.

Starting with a mechanism comprising reactions 1-12 augmented with the three reactions for CO conversion to CO_2 and the six HCO reactions of the San Diego mechanism [4], extensive computations of premixed flames and homogeneous ignition histories were performed to elucidate the minimum number of additional species and elementary steps needed to describe also the CO-oxidation chemistry of CO/H_2 mixtures containing H_2 in relative amounts typical of syngas, i.e., mole-fraction ratios $0.10 \lesssim X_{\mathrm{H_2}}/(X_{\mathrm{CO}} + X_{\mathrm{H_2}}) \lesssim 0.60$. It was found that adding only four elementary steps, numbered 13-16 in Table 5.1, with only 13 and 15 being reversible, sufficed to provide reasonably accurate predictions of burning rates and induction times under conditions of interest for gas-turbine combustion. Along with reaction 13, which is known to be central to CO oxidation, the extended mechanism includes reactions 15 and 16f, because they are needed for describing stoichiometric and rich flames, with deletion of 15b leading in particular to large overpredictions of burning rates for rich mixtures. On the other hand, reaction 14f, unimportant for flame propagation, was found to be essential for describing autoignition for conditions near the second explosion limit, in agreement with previous studies [65]. The overall skeletal mechanism therefore consists of 16 reactions, 8 reversible, and 11 reactive species.

	Reaction		A^a	n	E^a
1	$H+O_2 \rightleftharpoons OH+O$	k_f	$3.52\ 10^{16}$	-0.7	71.42
		k_b	$7.04\ 10^{13}$	-0.26	0.60
2	$H_2+O \rightleftharpoons OH+H$	k_f	$5.06\ 10^{4}$	2.67	26.32
		k_b	$3.03\ 10^{4}$	2.63	20.23
3	$H_2+OH \rightleftharpoons H_2O+H$	k_f	$1.17\ 10^{9}$	1.3	15.21
		k_b	$1.28\ 10^{10}$	1.19	78.25
4	$H+O_2+M \rightarrow HO_2+M^b$	k_0	$5.75\ 10^{19}$	-1.4	0.0
		k_∞	$4.65\ 10^{12}$	0.44	0.0
5	$HO_2+H \rightarrow 2OH$		$7.08\ 10^{13}$	0.0	1.23
6	$HO_2+H \rightleftharpoons H_2+O_2$	k_f	$1.66\ 10^{13}$	0.0	3.44
		k_b	$2.69\ 10^{12}$	0.36	231.86
7	$HO_2+OH \rightarrow H_2O+O_2$		$2.89\ 10^{13}$	0.0	-2.08
8	$H+OH+M \rightleftharpoons H_2O+M^c$	k_f	$4.00\ 10^{22}$	-2.0	0.0
		k_b	$1.03\ 10^{23}$	-1.75	496.14
9	$2H+M \rightleftharpoons H_2+M^d$	k_f	$1.30\ 10^{18}$	-1.0	0.0
		k_b	$3.04\ 10^{17}$	-0.65	433.09
10	$2HO_2 \rightarrow H_2O_2+O_2$		$3.02\ 10^{12}$	0.0	5.8
11	$HO_2+H_2 \rightarrow H_2O_2+H$		$1.62\ 10^{11}$	0.61	100.14
12	$H_2O_2+M \rightarrow 2OH+M^e$	k_0	$8.15\ 10^{23}$	-1.9	207.62
		k_∞	$2.62\ 10^{19}$	-1.39	214.74
13	$CO + OH \rightleftharpoons CO_2 + H$	k_f	$4.4\ 10^{6}$	1.5	-3.1
		k_b	$2.41\ 10^{13}$	0.22	104.60
14	$CO + HO_2 \rightarrow CO_2 + OH$		$6.03\ 10^{13}$	0.0	96.0
15	$HCO + M \rightleftharpoons CO + H + M^f$	k_f	$1.86\ 10^{17}$	-1	71.13
		k_b	$3.51\ 10^{16}$	-0.77	5.35
16	$HCO + H \rightarrow CO + H_2$		$5.0\ 10^{13}$	0.0	0.0

Table 5.1: Rate coefficients in Arrhenius form $k = AT^n \exp(-E/R^oT)$ for the skeletal mechanism.

[a] Units are mol, s, cm^3, kJ, and K.

[b] Chaperon efficiencies are 2.5 for H_2, 16.0 for H_2O, 1.2 for CO, 2.4 for CO_2, 0.7 for Ar and He and 1.0 for all other species; Troe falloff with $F_c = 0.5$

[c] Chaperon efficiencies are 2.5 for H_2, 12.0 for H_2O, 1.9 for CO, 3.8 for CO_2, 0.5 for Ar and He and 1.0 for all other species.

[d] Chaperon efficiencies are 2.5 for H_2, 12.0 for H_2O, 1.9 for CO, 3.8 for CO_2, 0.38 for Ar and He and 1.0 for all other species.

[e] Chaperon efficiencies are 2.0 for H_2, 6.0 for H_2O, 1.5 for CO, 2.0 for CO_2, 0.4 for Ar and He and 1.0 for all other species; $F_c = 0.265 \exp(-T/94\text{K}) + 0.735 \exp(-T/1756\text{K}) + \exp(-5182\text{K}/T)$

[f] Chaperon efficiencies are 1.9 for H_2, 12.0 for H_2O, 2.5 for CO, 2.5 for CO_2 and 1.0 for all other species.

The reduction continues by introducing steady-state assumptions for intermediates, as is appropriate for O, OH and H_2O_2 in hydrogen-air deflagrations, as well as in CO/H_2-air deflagrations, as indicated by our computations, with HCO also accurately obeying a steady state in the latter system. With these approximations, the chemistry for CO/H_2 oxidation reduces to the four global steps

$$\begin{aligned} 3H_2 + O_2 &\overset{\text{I}}{\rightleftharpoons} 2H_2O + 2H \\ 2H + M &\overset{\text{II}}{\rightleftharpoons} H_2 + M \\ H_2 + O_2 &\overset{\text{III}}{\rightleftharpoons} HO_2 + H \\ CO + H_2O &\overset{\text{IV}}{\rightleftharpoons} CO_2 + H_2, \end{aligned}$$

with rates given in terms of the different elementary reaction rates by the expressions

$$\omega_{\text{I}} = \omega_1 + \omega_{5f} + \omega_{10f} + \omega_{11f} + \omega_{14f}, \tag{5.1a}$$

$$\omega_{\text{II}} = \omega_{4f} + \omega_8 + \omega_9 - \omega_{10f} - \omega_{11f} - \omega_{15}, \tag{5.1b}$$

$$\omega_{\text{III}} = \omega_{4f} - \omega_{5f} - \omega_6 - \omega_{7f} - 2\omega_{10f} - \omega_{11f} - \omega_{14f}, \tag{5.1c}$$

$$\omega_{\text{IV}} = \omega_{13} + \omega_{14f}. \tag{5.1d}$$

The temperature T and the concentrations C_i of the seven species of the reduced mechanism (O_2, H_2, CO, H_2O, CO_2, H, HO_2) enter in the computation of the above elementary rates. The computation of ω_{1b}, ω_{7f}, ω_{8f}, and ω_{13f} requires also knowledge of the OH concentration C_{OH}, while the O-atom and formyl concentrations C_{O} and C_{HCO} are needed to compute ω_{1b} and ω_{15f}, respectively. These additional concentrations can be obtained by solving the four steady-state equations derived by equating the production and consumption chemical rates of OH, O, H_2O_2, and HCO given by the skeletal mechanism, yielding the explicit expressions

$$C_{\text{OH}} = [(A_1^2 + 4A_0A_2)^{1/2} - A_1]/(2A_2), \tag{5.2}$$

$$C_{\text{O}} = \frac{k_{1f}C_{\text{H}}C_{\text{O}_2} + k_{2b}C_{\text{OH}}C_{\text{H}}}{k_{1b}C_{\text{OH}} + k_{2f}C_{\text{H}_2}}, \tag{5.3}$$

$$C_{\text{HCO}} = \frac{k_{15b}C_{\text{CO}}C_{\text{H}}C_{\text{M}_{15}}}{k_{15f}C_{\text{M}_{15}} + k_{16f}C_{\text{H}}}, \tag{5.4}$$

with

$$\begin{aligned} A_0 = {} & k_{2f}C_{\text{H}_2}(2k_{1f}C_{\text{H}}C_{\text{O}_2} + k_{3b}C_{\text{H}}C_{\text{H}_2\text{O}} + 2k_{5f}C_{\text{H}}C_{\text{HO}_2} + k_{8b}C_{\text{M}_8}C_{\text{H}_2\text{O}} \\ & +2k_{10f}C_{\text{HO}_2}^2 + 2k_{11f}C_{\text{HO}_2}C_{\text{H}_2} + k_{13b}C_{\text{CO}_2}C_{\text{H}} + k_{14f}C_{\text{CO}}C_{\text{HO}_2}), \\ A_1 = {} & k_{2f}C_{\text{H}_2}(k_{3f}C_{\text{H}_2} + k_{7f}C_{\text{HO}_2} + k_{8f}C_{\text{M}_8}C_{\text{H}} + k_{13f}C_{\text{CO}}) \\ & -k_{1b}(k_{3b}C_{\text{H}}C_{\text{H}_2\text{O}} + 2k_{5f}C_{\text{H}}C_{\text{HO}_2} + k_{8b}C_{\text{M}_8}C_{\text{H}_2\text{O}} \\ & +2k_{10f}C_{\text{HO}_2}^2 + 2k_{11f}C_{\text{HO}_2}C_{\text{H}_2} + k_{13b}C_{\text{CO}_2}C_{\text{H}} + k_{14f}C_{\text{CO}}C_{\text{HO}_2}), \\ A_2 = {} & k_{1b}(2k_{2b}C_{\text{H}} + k_{3f}C_{\text{H}_2} + k_{7f}C_{\text{HO}_2} + k_{8f}C_{\text{M}_8}C_{\text{H}} + k_{13f}C_{\text{CO}}). \end{aligned}$$

As discussed in Chapter 3, the steady states for O and OH, which hold with reasonable accuracy in flames, fail however during autoignition events, thereby leading to significant underpredictions of induction times, with errors increasing for decreasing equivalence ratio. An appropriate correction to the branching rate is obtained by introducing, during the chain-branching period that leads to autoignition, modified rates $\omega_{\text{I}}^*/\omega_{\text{I}} = \omega_{\text{II}}^*/\omega_{\text{II}} = \omega_{\text{III}}^*/\omega_{\text{III}} = \omega_{\text{IV}}^*/\omega_{\text{IV}} = \Lambda$, where the factor Λ is that derived in Chapter 3, and given by Eqs. (3.7), (3.9) and (3.14). For the reasons detailed in Sec. 3.5 in the case of H_2-O_2 autoignition, the modification must be switched off by setting $\Lambda = 1$ in places where the steady states for O and OH apply, which occurs in general in hot regions with relatively high radical concentrations, where the HO_2 steady state also holds. The modification criterion presented in Sec. 3.5 is adapted for this reduced chemistry, by the inclusion of an extra term in the rate of HO_2 consumption $\dot{C}_{\text{HO}_{2C}} = \omega_{5f} + \omega_{6f} + \omega_{7f} + 2\omega_{10f} + \omega_{11f} + \omega_{14f}$, to account for the consumption of HO_2 by step 14f, specific to CO oxidation.

Note that, since the first twelve steps of the skeletal mechanism in Table 5.1 are identical to those used in Chapter 2, in the absence of CO the four-step mechanism described above naturally reduces to the three-step mechanism for H_2-air combustion.

5.2 Validation of the reduced mechanism

The chemical-kinetic mechanism discussed above were used in COSILAB [46] computations of laminar flame velocities and induction times. To test the degree of accuracy associated with the chemical simplifications, the numerical results were compared with those obtained from both detailed-chemistry computations and computations with the skeletal mechanism of Table 5.1. In addition, to test practical applicability, the results were compared with recent experimental data. In particular, Figs. 5.1 and 5.2 test the predictive capability of the chemical-kinetic mechanisms with regard to burning rates, whereas Fig. 5.3 is used to compare predictions of ignition times.

Different pressures are considered in Fig. 5.1 for two different values of the CO/H_2 ratio characteristic of typical syngas mixtures. The performance of the reduced mechanism is seen to be satisfactory for all conditions investigated, based on comparisons with both the detailed and skeletal mechanisms. For very rich mixtures at the highest pressure shown, the detailed-chemistry description employed here consistently gives burning rates that are much larger than those obtained in experiments, while there are other descriptions that produce better agreement [66]. The detailed chemistry deserves further attention for these conditions. For all other conditions, the agreement of the detailed and skeletal mechanisms with the experiments is very good, while the reduced mechanism tends to overpredict burning rates as a result of the steady-state assumptions introduced, with errors being typically smaller than 15 %.

Preheat is investigated in Fig. 5.2.a, along with fuel dilution with CO_2. Both effects are well reproduced by the reduced chemistry, except in highly preheated mixtures, with $T_u = 700$ K, where overpredictions of flame velocities, in comparison with predictions of the detailed chemistry are on the order of 15 %. With strong preheat, besides significant errors associated with the steady-state simplifications, there exist noticeable discrepancies between the detailed-chemistry predictions and the experimental results [69], further augmenting reduced-chemistry discrepancies and calling for future detailed-chemistry investigation, even though experimentally it might be difficult to suppress pre-reaction at such high initial temperatures.

The dependence of the burning rate on the relative CO/H_2 content of the fuel mixture is shown in Fig. 5.2.b at both atmospheric and elevated pressure and for conditions ranging from pure H_2 to pure CO and including preheated mixtures and fuel dilution with CO_2. It can be seen that both the detailed and the skeletal mechanisms agree well with the experimental measurements for all of these conditions, whereas the reduced mechanism tends to overpredict burning rates. As in Fig. 5.1, errors are seen to be typically smaller than 15 %, the only exception being fuel mixtures with very small H_2 content, for which the errors become larger, especially for atmospheric combustion.

Autoignition times, defined by a temperature-inflexion criterion for homogeneous adiabatic ignition computations in an isobaric reactor, are compared in Fig. 5.3 with results of recent shock-tube measurements [65] for CO/H_2-air mixtures with $\phi = 0.5$ and different CO/H_2 ratios representative of typical syngas mixtures. The conditions considered include near-atmospheric and elevated pressure, although no experimental measurements are available at high pressure for the two mixtures with larger H_2/CO ratio. As can be seen, the agreement found between the computations and the experiments is reasonably good for conditions that place the system above, around or slightly below crossover, such that the resulting induction times are small. For these lean mixtures, the previously discussed correction factor Λ in essential for achieving accurate results; without this branching-rate correction, the reduced chemistry would predict the induction time to be less than one third of that obtained with detailed chemistry. The reduced-chemistry predictions are in excellent agreement with detailed-chemistry predictions until temperatures decrease below about 900 K, where the need for further study of both computational and experimental results has been discussed widely in the literature [71–73].

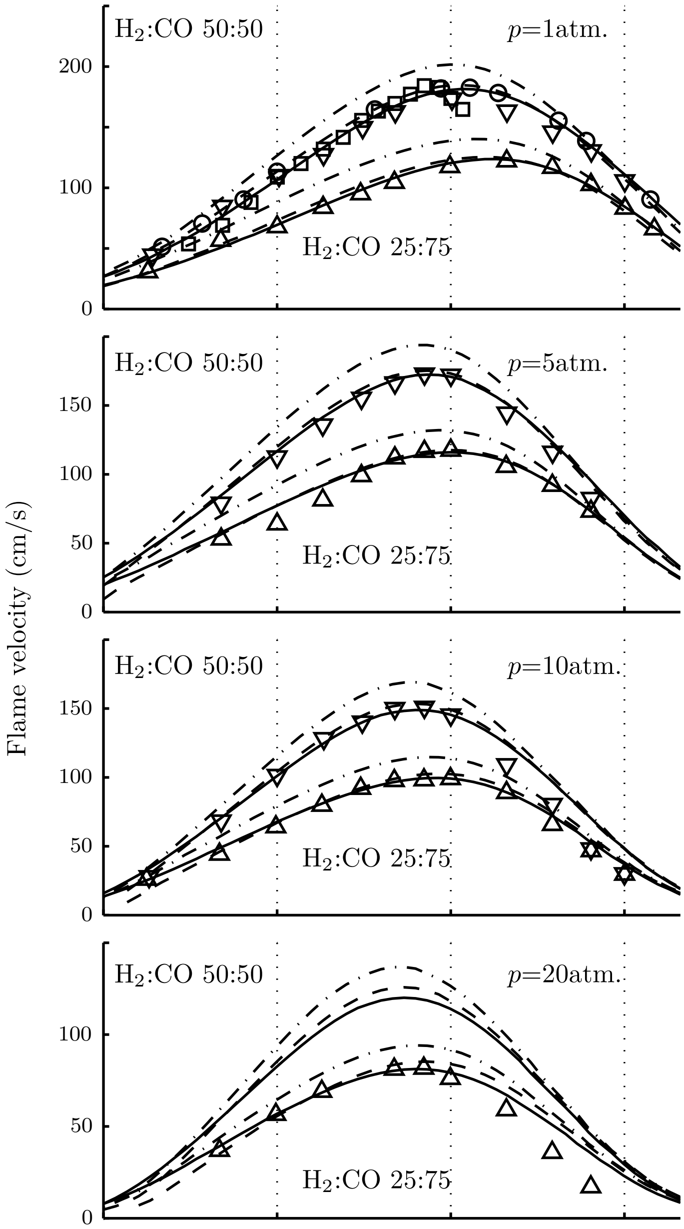

Figure 5.1: The variation with equivalence ratio of the laminar flame velocity for a CO/H$_2$-oxidizer mixture at initial temperature $T_u = 300$ K and for four different pressures and two different CO/H$_2$ ratios as obtained from numerical integrations with detailed (solid curves), skeletal (dashed curves), and reduced (dot-dashed curves) chemistry descriptions and from laboratory measurements (triangles: [66]; cicles: [67]; squares ×: [68]); the oxidizer for $p = 1$ atm is air, while for $p = (5, 10, 20)$ atm it is an oxygen-helium mixture with mole-fraction ratio $X_{\mathrm{He}}/X_{\mathrm{O_2}} = 7$ [66].

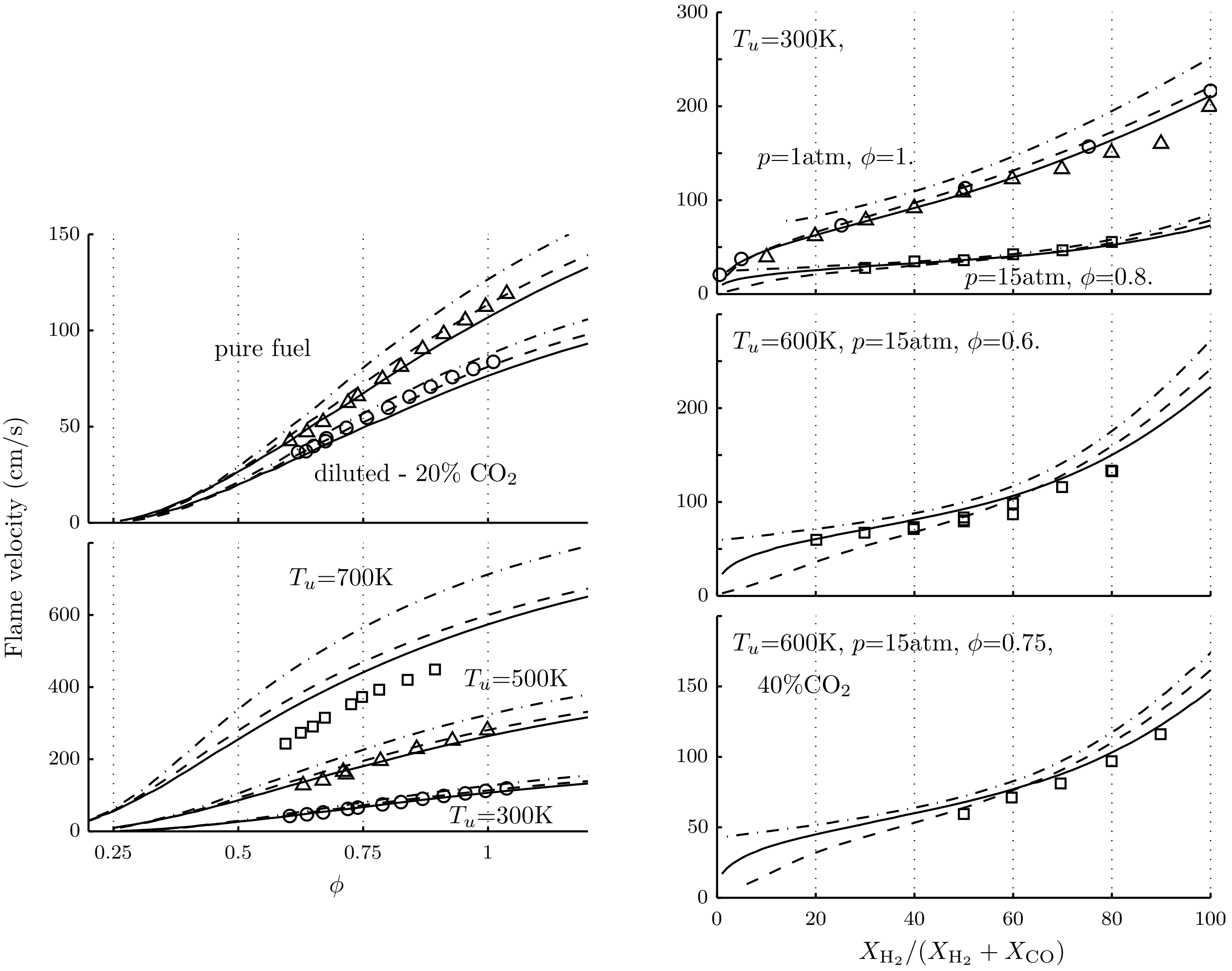

a.

b.

Figure 5.2: a. The variation with equivalence ratio of the laminar flame velocity for a $CO/H_2/CO_2$-air mixture with $X_{CO}/X_{H_2} = 1$ at $p = 1$ atm as obtained from numerical integrations with detailed (solid curves), skeletal (dashed curves), and reduced (dot-dashed curves) chemistry descriptions and from laboratory measurements (symbols: [70]). The lower plot shows results for $X_{CO_2} = 0$ with three different values of T_u while the upper plot shows results for $T_u = 300$ K with $X_{CO_2} = 0$ and with $X_{CO_2} = 0.2$ in the fuel mixture. b. The variation of the laminar flame velocity with the fuel composition for a $CO/H_2/CO_2$-oxidizer mixture as obtained from numerical integrations with detailed (solid curves), skeletal (dashed curves), and reduced (dot-dashed curves) chemistry descriptions and from laboratory measurements (circles: [67]; triangles: [68]; squares: [69]). The oxidizer is air for $p = 1$ atm and a helium-oxygen mixture with mole-fraction ratio $X_{He}/X_{O_2} = 9$ for $p = 15$ atm. Fuel dilution with CO_2 is considered in the bottom plot; all other cases correspond to undiluted CO/H_2 fuel mixtures.

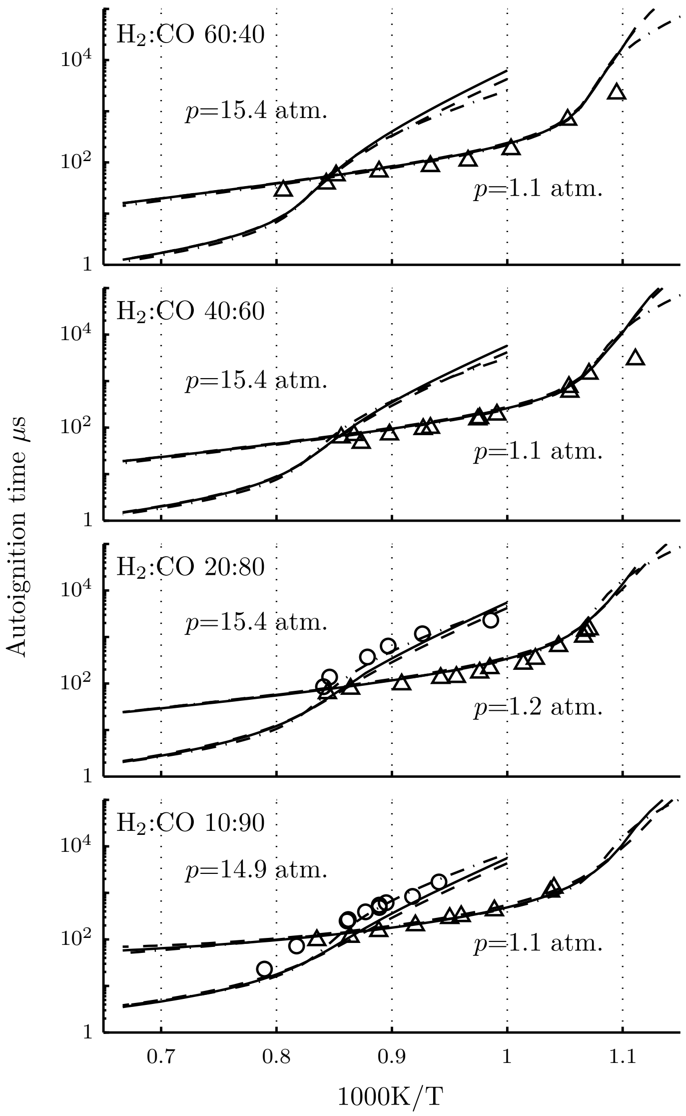

Figure 5.3: The variation with initial temperature of the induction time for a CO/H$_2$-air mixture with $\phi = 0.5$ as obtained from numerical integrations with detailed (solid curves), skeletal (dashed curves), and reduced (dot-dashed curves) chemistry descriptions and from laboratory measurements (symbols: [65]).

5.3 Concluding remarks

The mechanism presented here can be used over a wide range of combustion conditions that include, in particular, most of those of gas-turbine operation. In view of the previously identified discrepancies between predictions of current chemical-kinetic mechanisms and experimental measurements [70, 74], further improvements of the reduced mechanism may stem from modifications in reaction rates of elementary steps, to be sought in future chemical-kinetic investigations, leading to better predictions of burning rates for strongly preheated mixtures as well as of induction times at temperatures below crossover. Further simplifications of the reduced description, arising for instance in connection with steady states of additional intermediaries, are worth pursuing in the future for application under more restrictive combustion conditions. For instance, a HO_2 steady state is accurate within the main reaction layer in deflagrations, thereby leading to a three-step mechanism, which would, however, not be very accurate for describing autoignition. An even simpler description for syngas flames arises for conditions such that the peak temperature lies close to the crossover value, as occurs in very lean (or very rich) mixtures or in highly diluted environments, for which a two-step mechanism can be envisioned to be sufficiently accurate, with both H and HO_2 maintaining steady state, as occurs in H_2-air flames near the lean limit [30, 31].

The work presented in this chapter corresponds to the article "A four-step reduced mechanism for syngas combustion", published in Combustion and Flame [75].

CHAPTER 6

Explicit analytic prediction for hydrogen-oxygen ignition times at temperatures below crossover

Numerous analytic studies of ignition above crossover are available, including explicit analytic predictions of induction times [37, 45, 76–80]. By way of contrast, theoretical investigations of low-temperature ignition are scarce. The most notable contribution is that of Treviño [45], who identified in particular the key chemistry and attempted an analysis of the corresponding ignition event. He found in particular that, while H_2-O_2 ignition at high temperature takes place as a branched-chain explosion, a thermal runaway characterizes ignition below crossover. The present chapter extends the previous work by further simplifying the chemistry description to a form that is amenable to asymptotic treatment by activation-energy asymptotics, leading to an explicit expression that gives predictions of induction times in close agreement with those obtained by numerical integrations employing detailed chemistry.

Before proceeding with the analysis, it is worth mentioning that experiments of homogeneous ignition encounter numerous difficulties at temperatures below crossover [81], with ignition occurring locally at points typically located near walls and extending to the reactive mixture through flame propagation. As a result, the ignition delay measured experimentally in shock tubes is not that corresponding to homogeneous autoignition but rather the ratio of the tube radius to the flame speed [82]. Although more work is required to further clarify the nature of these low-temperature shock-tube processes, that is not the intention of the present chapter. Instead, the analysis focuses on the homogeneous ignition regime by taking a widely accepted, detailed chemical-kinetic mechanism [4] as a starting point for the development of analytical results and using this detailed scheme in numerical integrations for validation purposes.

6.1 Reduced-chemistry description

We have seen above that, at sufficiently high temperature, ignition is characterized by a long induction period of chain-carrier growth determined by the competition of chain-branching reactions, such as $H+O_2 \overset{1f}{\to} OH+O$, with chain-terminating three-body collisions, such as $H+O_2+M \overset{4f}{\to} HO_2+M$, while the initiation reaction $H_2+O_2 \overset{6b}{\to} HO_2+H$ is only significant during the initial instants. If the mixture is sufficiently rich, then the shuffle reactions $H_2+O \overset{2f}{\to} OH+H$ and $H_2+OH \overset{3f}{\to} H_2O+H$ are sufficiently fast for the radicals O and OH to maintain steady state. In that case, a single global reaction of the form $3H_2+O_2 \to 2H_2O+2H$ describes accurately the growth of H radicals, the rate of H-atom production being given by twice that of reaction 1f minus that of reaction 4f [37].

Previous theoretical analyses have shown that high-temperature ignition histories can be computed accurately from integrations of unsteady homogeneous equations in isobaric adiabatic systems, which yield analytic expressions for the induction time above crossover when the effects of reactant consumption and heat release are both neglected during the induction period [37, 45, 76–80]. Ignition events described by the overall reaction $3H_2+O_2 \to 2H_2O+2H$ have ignition times t_i that increase linearly proportional to $(2k_{1f} - k_{4f}C_{M_4})^{-1}$, where k_j represents the rate constant for reaction j and C_{M_4} is the effective third-body concentration of reaction 4. This factor defines the relevant crossover temperature for ignition of rich mixtures according to $2k_{1f} = k_{4f}C_{\mathrm{M}_4}$, giving a value on the order of $T_c = 950$ K at atmospheric pressure. For temperatures above crossover, the inequality $2k_{1f} > k_{4f}C_{\mathrm{M}_4}$ applies and a successful branched-chain explosion develops. As the temperature decreases, chain termination through $\mathrm{H+O_2+M} \xrightarrow{4f} \mathrm{HO_2+M}$ becomes increasingly important, augmenting the induction time and causing the prediction for t_i to diverge to infinity as crossover is reached [37].

This divergence is illustrated in Fig. 6.1, which shows the variation with initial temperature of the induction time computed in an isobaric homogeneous reactor with detailed chemistry and also with the two-step and the corrected three-step reduced mechanisms derived in Chapters 2 and 3, respectively. The two-step reduced mechanism underpredicts the ignition time above crossover but as crossover is approached yields a diverging value for t_i, in agreement with the previous discussion. The three-step reduced mechanism with the correction to account for O and OH steady-state failure is seen to give an excellent prediction for t_i at high temperature. Although the resulting value of t_i remains finite at all temperatures as a result of consideration of $\mathrm{HO_2}$ out of steady state, the associated accuracy degrades appreciably at temperatures below crossover, with computed ignition times that for $T \simeq 800$ K at $p = 1$ atm are already twenty times smaller than those obtained with detailed chemistry.

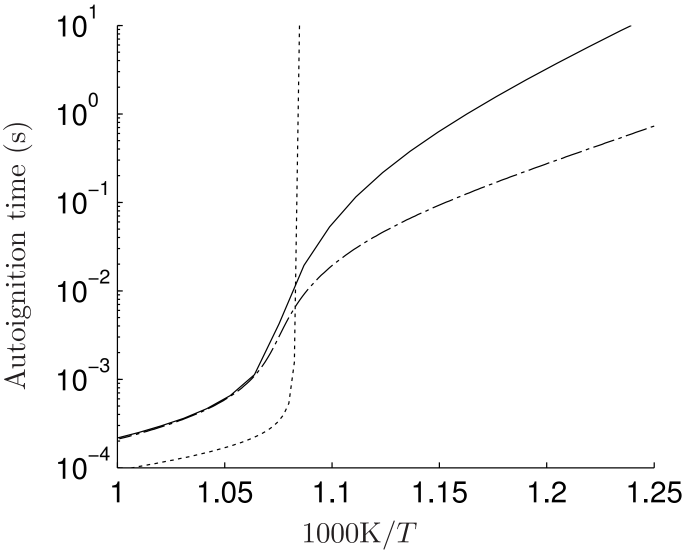

Figure 6.1: The variation with equivalence ratio of the induction time as obtained in an isobaric homogeneous reactor for $\phi = 0.5$ K and $p = 1$ atm with the detailed 21-step chemistry (solid curves), with the short 12-step chemistry (dashed curves), with the 3-step reduced mechanism including the correction (dot-dashed curves), and with the 2-step reduced mechanism (dotted curves).

Clearly, the prevailing rate of chain termination through $\mathrm{H+O_2+M} \xrightarrow{4f} \mathrm{HO_2+M}$ precludes in principle chain branching at temperatures below crossover. As shown by Treviño [45], the alternative branched-chain path that enables ignition is provided by $\mathrm{H_2O_2+M} \xrightarrow{12f} \mathrm{2OH+M}$, with $\mathrm{H_2O_2}$ being formed through $\mathrm{2HO_2} \xrightarrow{10f} \mathrm{H_2O_2+O_2}$ and, to a smaller extent, also through $\mathrm{HO_2+H_2} \xrightarrow{11f} \mathrm{H_2O_2+H}$, so that a total of 8 elementary reactions, included in Table 2.2, are needed for the description of low-temperature ignition. The reaction-rate parameters included in the table are those of the so-called San-Diego mechanism [4], a detailed 21-step scheme that will be used below in the numerical integrations for validation purposes.

Treviño also noticed that, because of rapid H-atom removal through $\mathrm{H+O_2+M} \xrightarrow{4f} \mathrm{HO_2+M}$, all three radicals O, OH and H maintain steady state during ignition below crossover [45]. The resulting reduced chemistry can be expressed as three overall steps

$$\begin{aligned} 2H_2 + O_2 &\overset{\text{I}}{\rightarrow} 2H_2O \\ 2H_2O &\overset{\text{II}}{\rightarrow} H_2O_2 + H_2 \\ H_2 + 2O_2 &\overset{\text{III}}{\rightarrow} 2HO_2 \end{aligned}$$

with rates (mols per unit volume per unit time) given by $\omega_{\text{I}} = \omega_{1f} + \omega_{10f} + \omega_{11f}$, $\omega_{\text{II}} = \omega_{10f} + \omega_{11f} - \omega_{12f}$, and $\omega_{\text{III}} = \frac{1}{2}(\omega_{4f} + \omega_{6b} - 2\omega_{10f} - \omega_{11f})$, and with the H-atom concentration, needed to evaluate ω_{1f} and ω_{4f}, given by its steady-state expression

$$C_{\text{H}} = \frac{\omega_{6b} + \omega_{11f} + 2\omega_{12f}}{(k_{4f}C_{\text{M}_4} - 2k_{1f})C_{\text{O}_2}}. \tag{6.1}$$

Results obtained by using this three-step mechanism in numerical integrations of adiabatic, isobaric homogeneous reactors are compared in Fig. 6.2 with those obtained with the 21-step San Diego mechanism, with the ignition time defined in the computations by the temperature-inflection criterion. For the stoichiometric H_2-air mixture considered, the crossover temperature defined from the condition $2k_{1f} = k_{4f}C_{\text{M}_4}$ is $T_c = (943, 1186, 1431)$ K for $p = (1, 10, 50)$ atm. As can be seen, Treviño's chemistry gives excellent agreement for the three pressures tested in the figure for initial temperatures below the crossover value. Since it is evident from (6.1) that the reduction fails at crossover, it is noteworthy that the results remain reasonable up to within about 25 K of crossover.

6.2 Further chemistry simplifications

The thermal-explosion character of ignition at temperatures below crossover is illustrated in the plot of Fig. 6.3, which shows the temperature evolution for a stoichiometric H_2-air mixture at atmospheric pressure and with initial temperature $T = 820$ K. The very sharp temperature increase after the long delay involving an imperceptible temperature rise is indicative of a thermal explosion. To investigate the steady state of HO_2 and H_2O_2, the plot also includes as dashed curves the evolution with time of the ratio $(\omega_p - \omega_c)/\omega_p$ for these two species prior to ignition, with ω_p and ω_c representing their production and consumption rates (e.g., for HO_2, $\omega_p = \omega_{4f} + \omega_{6b}$ and $\omega_c = 2\omega_{10f} + \omega_{11f}$). As can be seen, a steady-state assumption is never a good approximation for H_2O_2. On the other hand, the HO_2 balance indicates that there exists an initial period in which this intermediate is created with negligible consumption, through $H_2{+}O_2 \overset{6b}{\rightarrow} HO_2{+}H$ followed by $H{+}O_2{+}M \overset{4f}{\rightarrow} HO_2{+}M$. When the HO_2 concentration reaches a sufficiently large value the overall consumption rate $2\omega_{10f} + \omega_{11f}$ becomes significant and eventually places this intermediate in steady state. Consequently, the HO_2 steady-state equation $\omega_{4f} + \omega_{6b} - 2\omega_{10f} - \omega_{11f} = 0$ applies with good accuracy over most of the ignition history, with the exception of the initial buildup period, to be neglected in the following description. This last steady-state equation, together with that of the H-atom, given in (6.1), yields

$$\begin{aligned} \omega_{\text{I}} &= \frac{\omega_{6b} + \omega_{11f} + (1+\alpha)\omega_{12f}}{1-\alpha} \\ \omega_{\text{II}} &= \frac{(1-\frac{1}{2}\alpha)(\omega_{6b} + \omega_{11f}) + \alpha\omega_{12f}}{1-\alpha}, \end{aligned} \tag{6.2}$$

for the rates of the overall steps

$$\begin{aligned} 2H_2 + O_2 &\overset{\text{I}}{\rightarrow} 2H_2O \\ 2H_2O &\overset{\text{II}}{\rightarrow} H_2O_2 + H_2. \end{aligned} \tag{6.3}$$

The reaction-rate ratio

$$\alpha = 2k_{1f}/(k_{4f}C_{\mathrm{M}_4}) \tag{6.4}$$

appearing above, which equals unity at crossover, decreases rapidly as the temperature decreases, reaching values on the order of $\alpha \sim 0.05$ as the temperature falls 200 K below crossover. The HO_2 concentration, needed to compute ω_{11f}, can be determined from the truncated expression

$$C_{\mathrm{HO}_2} = \left(\frac{(2-\alpha)\omega_{6b} + 2\omega_{12f}}{2(1-\alpha)k_{10f}}\right)^{1/2}, \tag{6.5}$$

obtained from the corresponding steady-state equation $\omega_{4f} + \omega_{6b} - 2\omega_{10f} - \omega_{11f} = 0$ by using (6.1) to write ω_{4f} and neglecting hydroperoxyl consumption through $HO_2 + H_2 \xrightarrow{11f} H_2O_2 + H$, an excellent approximation under most conditions.

The accuracy of the two-step mechanism is tested in Fig. 6.2, in which the initial concentrations involve no radicals for the detailed chemistry but very small radical concentrations consistent with the steady states for the reduced mechanisms. As can be seen, the agreement obtained is excellent for initial temperatures $T \lesssim 1000$ K, including in particular all temperatures below crossover at atmospheric pressure. Increasing departures are however observed for higher temperatures in the plots for $p = 10$ atm and $p = 50$ atm. At these elevated temperatures, ignition times are short, because H_2O_2 consumption through reaction 12f becomes very fast. Since the HO_2 chemistry is much less dependent on temperature changes, as can be seen in the reaction-rate constants of $H{+}O_2{+}M \xrightarrow{4f} HO_2{+}M$ and $2HO_2 \xrightarrow{10f} H_2O_2{+}O_2$, the steady-state assumption for this species becomes less accurate, in that the initial HO_2 build-up period, required for the HO_2 concentration to increase to a sufficiently large value for its steady state to apply, takes up a significant fraction of the total ignition delay time. When that occurs, the two-step mechanism becomes less accurate and leads, for instance, to underpredictions in ignition time of the order of 50% for $p = 50$ atm and $T = 1200$ K. Except at those high-pressure, high-temperature conditions, the degree of accuracy of the two-step mechanism exhibited in Fig. 6.2 is quite satisfactory, thereby motivating the following development.

6.3 Activation-energy asymptotics

With reactant consumption neglected, as is appropriate given the thermal-runaway character of the ignition, the problem of homogeneous ignition in an adiabatic isobaric reactor reduces to that of integrating

$$\begin{aligned} \frac{\mathrm{d}C_{\mathrm{H_2O_2}}}{\mathrm{d}t} &= \omega_{\mathrm{II}} \\ \rho c_p \frac{\mathrm{d}T}{\mathrm{d}t} &= -2h_{\mathrm{H_2O}}(\omega_{\mathrm{I}} - \omega_{\mathrm{II}}) - h_{\mathrm{H_2O_2}}\omega_{\mathrm{II}} \end{aligned} \tag{6.6}$$

with initial conditions $T - T_o = C_{\mathrm{H_2O_2}} = 0$, where ρ and c_p are the initial values of the density and specific heat at constant pressure, and $h_{\mathrm{H_2O}} = -241.8$ kJ/mol and $h_{\mathrm{H_2O_2}} = -136.11$ kJ/mol are the values of the standard enthalpy of formation of the products. The analysis can be further simplified by noting that the direct contribution of ω_{6b} to the rates (6.2) is always small, initiation being triggered by ω_{11f} through the term involving ω_{6b} in $C_{\mathrm{HO_2}}$. Also, the combined contribution $\alpha(\omega_{12f} - \frac{1}{2}\omega_{11f})$ to ω_{II} can be neglected in the first approximation under most conditions, so that $\omega_{\mathrm{II}} \simeq \omega_{11f}/(1-\alpha)$. When these additional simplifications

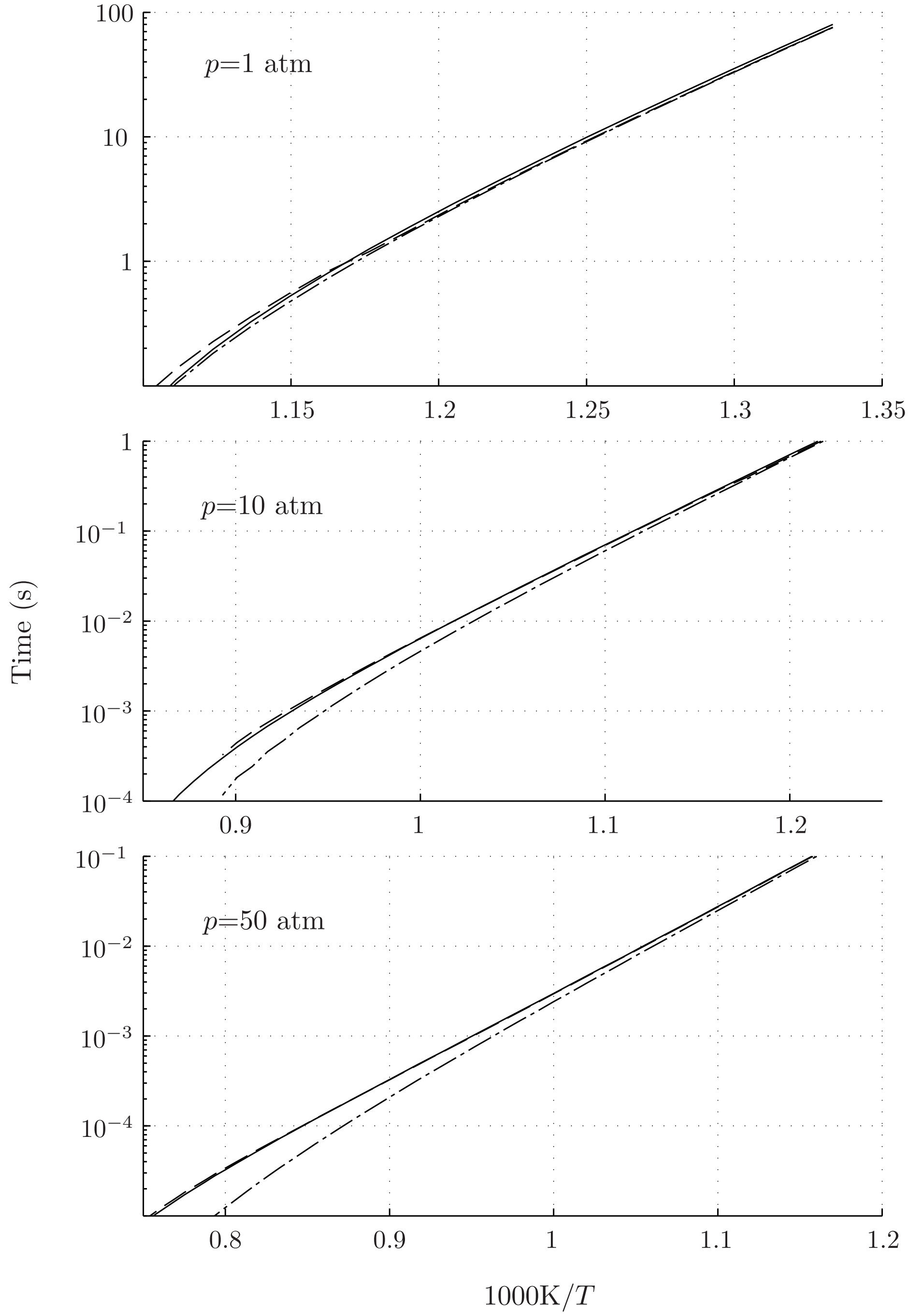

Figure 6.2: Ignition time obtained for a stoichiometric H_2-air mixture with 21-step detailed chemistry (solid line), with Treviño's 3-step reduced mechanism (dashed curves), and with the 2-step reduced mechanism given in (6.3) with the truncated HO_2 expression (6.5) (dot-dashed curves).

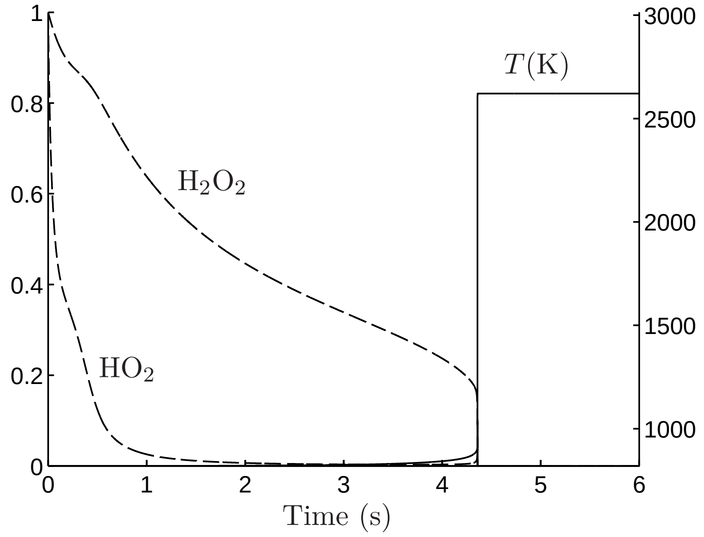

Figure 6.3: The temperature evolution (solid curve) during ignition of a stoichiometric H_2-air mixture at atmospheric pressure and with initial temperature $T = 820$ K. The dashed curves represent the corresponding steady-state ratios $(\omega_p - \omega_c)/\omega_p$ for HO_2 and H_2O_2 prior to ignition, with ω_p and ω_c representing their production and consumption rates.

are incorporated into (6.6) with (6.5) used to express $C_{\mathrm{HO_2}}$, the reduced expressions

$$\begin{aligned}\omega_{\mathrm{I}} - \omega_{\mathrm{II}} &= \frac{1+\alpha}{1-\alpha} k_{12f} C_{\mathrm{M}_{12}} C_{\mathrm{H_2O_2}} \\ \omega_{\mathrm{II}} &= \frac{k_{11f} k_{12f}^{1/2}}{k_{10f}^{1/2}} \frac{C_{\mathrm{H_2}} C_{\mathrm{M}_{12}}}{(1-\alpha)^{3/2}} \left[\left(1 - \frac{\alpha}{2}\right) \frac{k_{6b} C_{\mathrm{H_2}} C_{\mathrm{O_2}}}{k_{12f} C_{\mathrm{M}_{12}}^2} + \frac{C_{\mathrm{H_2O_2}}}{C_{\mathrm{M}_{12}}} \right]^{1/2},\end{aligned} \tag{6.7}$$

are obtained for the overall rates, where $C_{\mathrm{M}_{12}}$ is the effective third-body concentration of reaction 12f.

The activation energies of $k_{11f}(k_{12f}/k_{10f})^{1/2}$ and k_{12f} are very large, as could have been anticipated in view of the thermal-runaway character of the temperature evolution in Fig. 6.3. Their dimensionless values can be written with account taken of the algebraic temperature dependences present in k_{11f} and k_{12f} to give for instance $\beta_{11f} = E_{11f}/(R^o T_o) + n_{11f} + \frac{1}{2}[E_{12f}/(R^o T_o) + n_{12f} - E_{10f}/(R^o T_o)] = 29.88$ and $\beta_{12f} = E_{12f}/(R^o T_o) + n_{12f} = 29.31$ at $T_o = 800$ K. As can be seen, differences between these two quantities are very small and can be consequently neglected in the first approximation in the following asymptotic analysis, which uses a single dimensionless activation energy $\beta = \beta_{11f} = \beta_{12f}$ to define a dimensionless temperature increment

$$\theta = \beta \frac{T - T_o}{T_o}. \tag{6.8}$$

The resulting thermal explosion can be described by introducing additional dimensionless variables

$$\varphi = \left[(1-\alpha)^{1/2}(1+\alpha)\beta q\right]^{2/3} \left(\frac{k_{11f}}{(k_{10f}k_{12f})^{1/2}}\right)^{-2/3} \left(\frac{C_{\mathrm{H_2}}}{C_{\mathrm{M}_{12}}}\right)^{-2/3} \frac{C_{\mathrm{H_2O_2}}}{C_{\mathrm{M}_{12}}}, \tag{6.9}$$

and

$$\tau = \frac{(1+\alpha)^{1/3}}{(1-\alpha)^{4/3}} (\beta q)^{1/3} k_{12f} C_{\mathrm{M}_{12}} \left(\frac{k_{11f}}{(k_{10f}k_{12f})^{1/2}}\right)^{2/3} \left(\frac{C_{\mathrm{H_2}}}{C_{\mathrm{M}_{12}}}\right)^{2/3} t, \tag{6.10}$$

with

$$q = \frac{-2h_{\mathrm{H_2O}} C_{\mathrm{M}_{12}}}{\rho c_p T_o}, \tag{6.11}$$

all quantities (except, of course, $C_{\mathrm{H_2O_2}}$ and t) evaluated in the initial mixture, reducing the problem to that of integrating

$$\frac{\mathrm{d}\varphi}{\mathrm{d}\tau} = (a+\varphi)^{1/2}e^{\theta} \tag{6.12}$$

$$\frac{\mathrm{d}\theta}{\mathrm{d}\tau} = \varphi e^{\theta} + \Delta(a+\varphi)^{1/2}e^{\theta} \tag{6.13}$$

with initial conditions $\varphi = \theta = 0$ at $\tau = 0$. In the formulation,

$$a = \left(1-\frac{\alpha}{2}\right)^{1/3}(1-\alpha)^{1/3}(1+\alpha)^{2/3}(\beta q)^{2/3}\frac{k_{6b}k_{10f}^{1/3}}{(k_{11f}k_{12f})^{2/3}}\left(\frac{C_{\mathrm{H_2}}}{C_{\mathrm{M_{12}}}}\right)^{1/3}\left(\frac{C_{\mathrm{O_2}}}{C_{\mathrm{M_{12}}}}\right) \tag{6.14}$$

is a parameter measuring the initiation rate and

$$\Delta = \left[\frac{k_{11f}/(k_{10f}k_{12f})^{1/2}}{(1-\alpha)^{1/2}(1+\alpha)}\right]^{2/3}(\beta q)^{1/3}\left(\frac{C_{\mathrm{H_2}}}{C_{\mathrm{M_{12}}}}\right)^{2/3}\frac{h_{\mathrm{H_2O_2}}}{2h_{\mathrm{H_2O}}} \tag{6.15}$$

is a measure of the ratio of the heat-release rates associated with H_2O_2 and H_2O production. Note that the problem can be written as a single differential equation by dividing (6.12) and (6.13) and integrating to give

$$\theta = \frac{2}{3}(a+\varphi)^{3/2} - 2a(a+\varphi)^{1/2} + \frac{4}{3}a^{3/2} + \Delta\varphi \tag{6.16}$$

which can then be substituted into (6.12) to give an equation for the evolution of φ with τ.

The solution can be simplified by recognizing that $a \ll 1$, with typical values being of order $a \sim 10^{-4}$ at $T = 800$ K. Initiation is only important for $\tau \sim a^{1/2}$ when $\varphi \sim \theta \sim a$, and becomes negligible at later times, when (6.16) reduces to $\theta = (2/3)\varphi^{3/2} + \Delta\varphi$, so that the ignition time associated with thermal runaway is obtained from the quadrature

$$\tau_i = \int_0^{\infty} \frac{\mathrm{d}\varphi}{\varphi^{1/2}\exp\left(\frac{2}{3}\varphi^{3/2} + \Delta\varphi\right)}, \tag{6.17}$$

which converges as $\varphi \to 0$ because of the square-root dependence $\varphi^{1/2}$ affecting the H_2O_2 production rate. Note that if a linear dependence were present instead, as is typical of chain-branching processes, careful consideration of the initiation period would have been required, complicating the analysis, as shown in the general theory of branched-chain thermal explosions [83]. As an additional simplification to (6.17), it should also be noted that the reat release associated with H_2O_2 production is relatively small, giving small values of $\Delta \simeq 0.05$. If the corresponding contribution in the exponential is neglected, then the above integral reduces to $\tau_i = (2/3)^{2/3}\Gamma(1/3) \simeq 2.0444$, where Γ is the Gamma function.

6.4 The ignition time

With use made of (6.10), this final result of the activation-energy analysis can be expressed in dimensional form to yield

$$t_i = 2.0444\frac{(1-\alpha)^{4/3}}{(1+\alpha)^{1/3}}(\beta q)^{-1/3}(k_{12f}C_{\mathrm{M_{12}}})^{-1}\left(\frac{k_{11f}}{(k_{10f}k_{12f})^{1/2}}\right)^{-2/3}\left(\frac{C_{\mathrm{H_2}}}{C_{\mathrm{M_{12}}}}\right)^{-2/3} \tag{6.18}$$

as a prediction for the ignition time, where all reaction-rate constants and the parameters

$$\beta = \frac{E_{12f}}{R^oT} + n_{12f}, \quad q = -\frac{2h_{\mathrm{H_2O}}C_{\mathrm{M_{12}}}}{\rho c_p T} \quad \text{and} \quad \alpha = \frac{2k_{1f}}{k_{4f}C_{\mathrm{M_4}}} \tag{6.19}$$

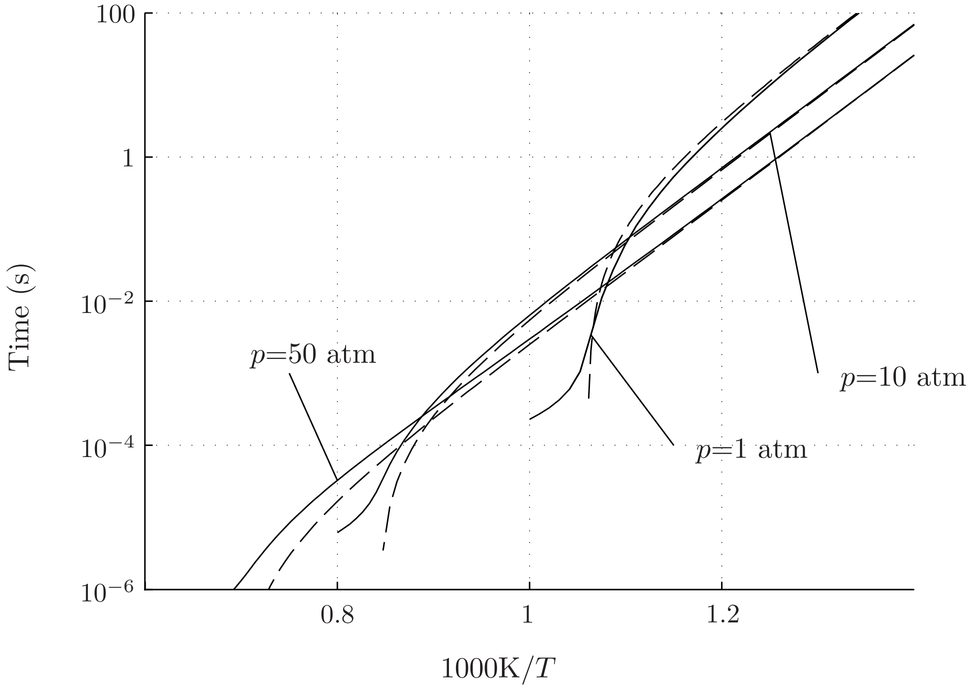

Figure 6.4: The variation with initial temperature of the ignition time for three different pressures as obtained for a stoichiometric H_2-air mixture by numerical integration of the conservation equations with 21-step chemistry (solid curves) and by evaluation of (6.18) (dashed curves).

are to be evaluated at the initial conditions, with the chaperon efficiencies taken into account in writing the effective third-body concentrations $C_{M_4} = p(1 + 1.5X_{H_2} + 15X_{H_2O})/(R^oT)$ and $C_{M_{12}} = p(1 + X_{H_2} + 5X_{H_2O})/(R^oT)$ in terms of the initial mole fractions X_i.

The explicit prediction given in (6.18) is compared in Figs. 6.4 and 6.5 with detailed-chemistry results. In particular, Fig. 6.4 shows the variation with temperature of the ignition time for a stoichiometric H_2-air mixture, giving excellent agreement for the three pressures tested. As expected, the prediction departs from the detailed-chemistry results as crossover is approached, when (6.18) predicts $t_i \to 0$ as $\alpha \to 1$, whereas the detailed-chemistry results exhibit the transition towards the fast high-temperature regime. Also, the accuracy degrades somewhat for $p = 50$ atm as the temperature increases above $T \simeq 1200$ K, in the temperature range where the HO_2 steady-state assumption no longer holds, as discussed above in connection with the validity of the two-step mechanism.

The variation with composition is tested separately in Fig. 6.5, where results corresponding to H_2-air mixtures at three different pressures are shown, along with results of ignition of H_2-O_2 mixtures at $p = 50$ atm and $p = 500$ atm, two limiting cases bounding the pressure range of interest for cryogenic rocket motor applications. The equivalence ratios investigated extend from very lean to very rich mixtures, within the range of flammability conditions. Except for very lean mixtures at atmospheric pressure, the errors are typically smaller than 20 % for the temperatures selected, i.e., $T = (800, 900, 1000, 1100)$ K for $p = (1, 10, 50, 500)$ atm. Additional computations, not shown in the figure, revealed that the errors are even smaller as the temperature is further decreased, in agreement with the results shown for stoichiometric mixtures in Fig. 6.4.

For mixtures at atmospheric pressure, the analytic expression tends to overpredict ignition times, giving errors that are more pronounced as the mixture becomes leaner. These overpredictions, exceeding 30 % for $\phi \lesssim 0.2$, are related to one of the simplifications introduced when deriving (6.7). As the H_2 concentration decreases for leaner mixtures, the rate of HO_2+$H_2 \overset{11f}{\to} H_2O_2$+H also decreases, which in turn reduces the

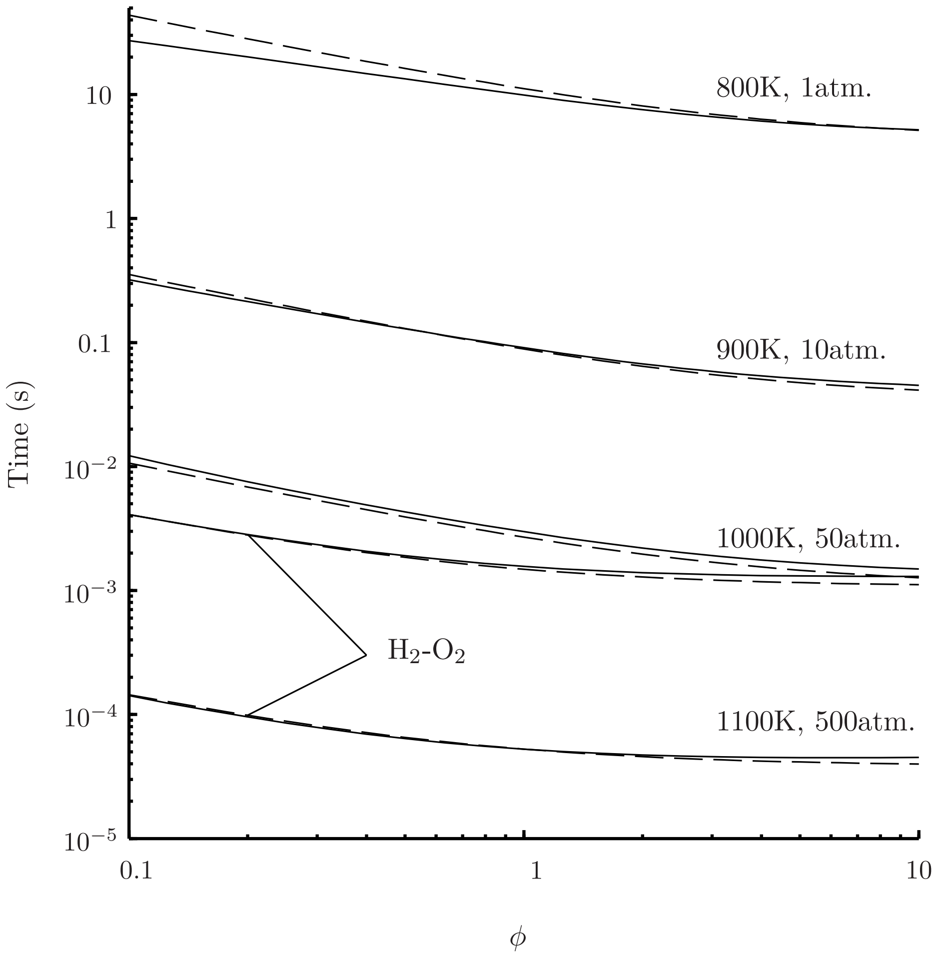

Figure 6.5: The variation with equivalence ratio of the ignition time as obtained by numerical integration of the conservation equations with 21-step chemistry (solid curves) and by evaluation of (6.18) (dashed curves) for H_2-air mixtures at different conditions of pressure and initial temperature and also for a H_2-O_2 mixture at $p = 50$ atm and $T = 1000$ K and at $p = 500$ atm and $T = 1100$ K.

accuracy of the approximation $(1 - \alpha/2)\omega_{11f} + \alpha\omega_{12f} \simeq \omega_{11f}$ used in writing ω_{II}, because the value of α is not small for these near-crossover conditions (e.g., $\alpha = 0.203$ for $\phi = 0.1$) and the rate ω_{12f} is independent of the H_2 concentration. Clearly, the error decreases rapidly as conditions move away from crossover, so that, for instance, at $\phi = 0.1$ and $p = 1$ atm the overprediction in ignition time is only 8 % when $T = 700$ K. This higher-order effect could be included in the asymptotic development by accounting for the missing term in (6.12), but that analysis is not pursued further here, because the expected improvements are limited to very lean mixtures near crossover, and the results are not reducible to a simple explicit form, such as that given in (6.18).

6.5 Conclusions

This chapter has shown how reduced-chemistry techniques based on chemical-time disparities can be combined with activation-energy asymptotics to yield an explicit expression for the ignition time of hydrogen-oxygen mixtures when the initial temperature is below the so-called crossover temperature. This expression shows that, while the rate of the branching step 1f (compared with that of the recombination step 4f) becomes important for reducing the ignition time as crossover is approached, far from crossover the induction delay depends instead only on the rate and energetic parameters of the steps 10f, 11f and 12f, involving H_2O_2, the ignition delay decreasing with increasing rate constants of steps 12f and 11f and (more weakly) with a decreasing rate constant for step 10f, according to the power-law factors exhibited in (6.18). The delay varies inversely with pressure, as is expected from the second-order (binary-collision) chemistry and exhibits effectively a 2/3 reaction-order dependence on the H_2 concentration, while being independent of the O_2 concentration.

The ignition-delay expression provided here has been tested to predict ignition times with accuracies that are typically better than 20 % over a wide range of temperature, pressures and compositions. Reduced accuracy is found only at elevated pressure for temperatures higher than $T \simeq 1100$ K, arising because of failure of the HO_2 steady-state approximation under those conditions, and also for extremely lean mixtures close to crossover, for which a more elaborate analysis would be needed to account for the greater complexity in the tradeoff between the contributions of steps 11f and 12f to H_2O_2 production and consumption. Nevertheless, the overall performance of the expression proposed for the ignition time is in general very satisfactory.

The work presented in this chapter corresponds to the article "Explicit analytic prediction for hydrogen-oxygen ignition times at temperatures below crossover", published in Combustion and Flame [84].

CHAPTER 7

Universal reduced chemistry for H_2-air combustion

Figure 7.1 compares ignition-time predictions obtained with detailed and skeletal chemistry with those obtained with the three-step reduced chemistry description derived in Chapter 3. As can be seen, excellent agreement is obtained for conditions above the second explosion limit – indicated in the figure by a vertical line – when the rates are modified to account for O and OH steady-state departures, a feature of the mechanism explained in Chapter 3. However, the reduced-chemistry description seems unable to reproduce with good accuracy autoignition processes close or below the second explosion limit, with departures increasing for decreasing temperatures. We shall see below that modifications to the chemistry, guided by knowledge gained in Chapter 6, are needed for derivation of reduced descriptions that can successfully describe not only flames and high-temperature autoignition, but also autoignition events below the second explosion limit.

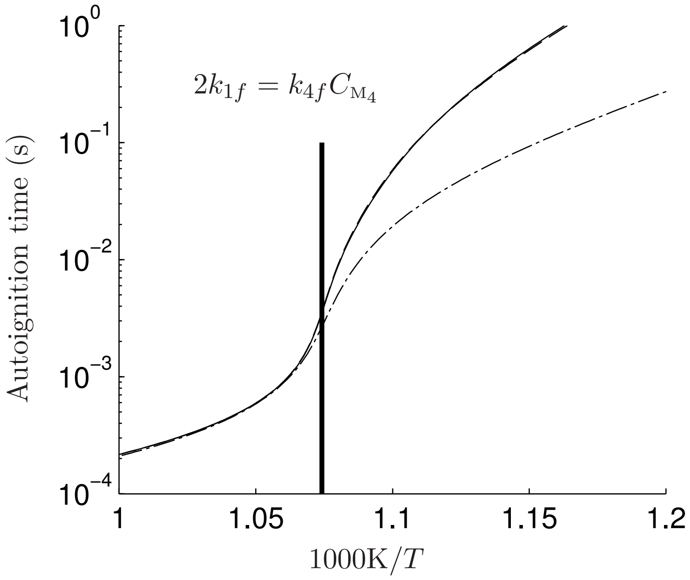

Figure 7.1: Ignition time obtained for a H_2-air mixture with $\phi = 0.5$ and $p = 1$ atm as obtained with the detailed 21-step chemistry (solid curves), with the short 12-step chemistry (dashed curves), with the 3-step reduced mechanism using the modified branching rates (dot-dashed curves).

7.1 Chemistry descriptions for autoignition

7.1.1 The four-step mechanism

The derivation below uses as starting point the 12-step short mechanism of Chapter 2, which is shown in Fig. 7.1 to give excelent predictions of ignition times for temperatures both above and below the crossover temperature. As seen in Chapter 6, while the H_2O_2 steady state is an excellent assumption for flames and also during high-temperature autoignition, it is, however, never a valid approximation during the thermal-runaway events that characterize autoignition below crossover. It then seems natural, in searching to extend the range of validity of the reduced chemistry, to consider the four-step reduced mechanism that follows from assuming that only O and OH are in steady state, while H, HO_2 and H_2O_2 are not. Starting from the twelve chemical steps in Tab. 2.2, and linearly combining the production rates $\dot{C}_i$ of each species i yields

$$\begin{aligned}
\dot{C}_{\mathrm{H_2}} - \dot{C}_{\mathrm{OH}} - 2\dot{C}_{\mathrm{O}} &= -3\omega_{\mathrm{I}} + \omega_{\mathrm{II}} - \omega_{\mathrm{III}} - \omega_{\mathrm{IV}} \\
\dot{C}_{\mathrm{O_2}} &= -\omega_{\mathrm{I}} - \omega_{\mathrm{III}} - \omega_{\mathrm{IV}} \\
\dot{C}_{\mathrm{H_2O}} + \dot{C}_{\mathrm{O}} + \dot{C}_{\mathrm{OH}} &= 2\omega_{\mathrm{I}} \\
\dot{C}_{\mathrm{H}} + \dot{C}_{\mathrm{OH}} + 2\dot{C}_{\mathrm{O}} &= 2\omega_{\mathrm{I}} - 2\omega_{\mathrm{II}} + \omega_{\mathrm{III}} \\
\dot{C}_{\mathrm{HO_2}} &= \omega_{\mathrm{III}} \\
\dot{C}_{\mathrm{H_2O_2}} &= \omega_{\mathrm{IV}},
\end{aligned} \tag{7.1}$$

where

$$\begin{aligned}
\omega_{\mathrm{I}} &= \omega_1 + \omega_{5f} + \omega_{12f} \\
\omega_{\mathrm{II}} &= \omega_{4f} + \omega_8 + \omega_9 - \omega_{10f} - \omega_{11f} \\
\omega_{\mathrm{III}} &= \omega_{4f} - \omega_{5f} - \omega_6 - \omega_{7f} - 2\omega_{10f} - \omega_{11f} \\
\omega_{\mathrm{IV}} &= \omega_{10f} + \omega_{11f} - \omega_{12f}.
\end{aligned} \tag{7.2}$$

Neglecting in (7.1) the small concentrations of the steady-state species O and OH reveals that the previous system of equations corresponds to the four overall reactions

$$\begin{aligned}
3\mathrm{H_2} + \mathrm{O_2} &\overset{\mathrm{I}}{\rightleftharpoons} 2\mathrm{H_2O} + 2\mathrm{H} \\
\mathrm{H} + \mathrm{H} + \mathrm{M} &\overset{\mathrm{II}}{\rightleftharpoons} \mathrm{H_2} + \mathrm{M} \\
\mathrm{H_2} + \mathrm{O_2} &\overset{\mathrm{III}}{\rightleftharpoons} \mathrm{HO_2} + \mathrm{H} \\
\mathrm{H_2} + \mathrm{O_2} &\overset{\mathrm{IV}}{\rightleftharpoons} \mathrm{H_2O_2}.
\end{aligned}$$

The computation of the rates ω_{1b}, ω_{7f} and ω_{8f} requires knowledge of the concentrations of O and OH, which can be obtained in explicit form by solving their steady-state equations. The expression for C_{O} given in (2.5) remains valid, whereas the expression (2.4) for C_{OH} must be modified to account for the fact that H_2O_2 is not assumed to be in steady state, yielding

$$C_{\mathrm{OH}} = [(A_1^2 + 4A_0A_2)^{1/2} - A_1]/(2A_2), \tag{7.3}$$

where

$$\begin{aligned}
A_0 = {} & C_{\mathrm{H_2}} k_{2f} (2k_{1f} C_{\mathrm{H}} C_{\mathrm{O_2}} + k_{3b} C_{\mathrm{H}} C_{\mathrm{H_2O}} + 2k_{5f} C_{\mathrm{H}} C_{\mathrm{HO_2}} \\
& + 2k_{12f} C_{\mathrm{H_2O_2}} C_{\mathrm{M_{12}}} + k_{8b} C_{\mathrm{M_8}} C_{\mathrm{H_2O}}) \\
A_1 = {} & + C_{\mathrm{H_2}} k_{2f} (k_{8f} C_{\mathrm{M_8}} C_{\mathrm{H}} + k_{7f} C_{\mathrm{HO_2}} + k_{3f} C_{\mathrm{H_2}}) \\
& - k_{1b} (k_{3b} C_{\mathrm{H}} C_{\mathrm{H_2O}} + 2k_{5f} C_{\mathrm{H}} C_{\mathrm{HO_2}} \\
& + 2k_{12f} C_{\mathrm{H_2O_2}} C_{\mathrm{M_{12}}} + k_{8b} C_{\mathrm{M_8}} C_{\mathrm{H_2O}}) \\
A_2 = {} & k_{1b} (2k_{2b} C_{\mathrm{H}} + k_{3f} C_{\mathrm{H_2}} + k_{7f} C_{\mathrm{HO_2}} + k_{8f} C_{\mathrm{M_8}} C_{\mathrm{H}}).
\end{aligned}$$

To account for the O and OH departures from steady states found during high-temperature autoignition events, the four overall rates are to be modified wherever HO_2 is not in steady-state, following the procedure presented in Chapter 3. The accuracy of the resulting description is illustrated in Fig. 7.2, which shows predictions of ignition times. The agreement with predictions of the detailed mechanism is seen to be excellent.

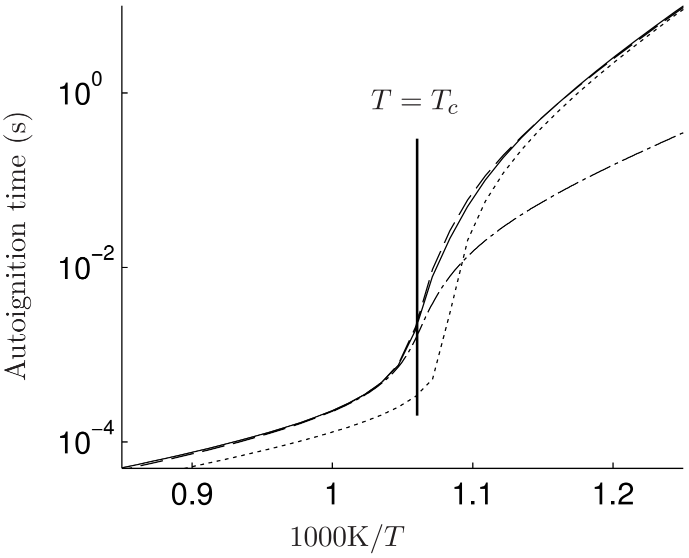

Figure 7.2: The variation with initial temperature of the ignition time for a stoichiometric mixture of H_2-air at atmospheric pressure as obtained with the temperature-inflection criterion with the detailed 21-step chemistry (solid curve), with the reduced four-step chemistry including HO_2 and H_2O_2 (dashed curve), with the three-step description including HO_2 (dot-dashed curve), and with the three-step description including H_2O_2 (dotted curve).

7.1.2 The two separate three-step mechanisms

According to the discussions given in the preceeding chapters, simplified versions of this four-step reduced mechanism apply for ignition conditions away from the second explosion limit. Thus, for ignition above crossover, H_2O_2 may be assumed to be in steady state, leading to the three-step reduced chemistry

$$\begin{aligned} 3H_2 + O_2 &\overset{\mathrm{I}}{\rightleftharpoons} 2H_2O + 2H \\ H + H + M &\overset{\mathrm{II}}{\rightleftharpoons} H_2 + M \\ H_2 + O_2 &\overset{\mathrm{III}}{\rightleftharpoons} HO_2 + H \end{aligned}$$

derived in Chapter 3, with rates

$$\begin{aligned} \omega_{\mathrm{I}} &= \omega_1 + \omega_{5f} + \omega_{10f} + \omega_{11f} \\ \omega_{\mathrm{II}} &= \omega_{4f} + \omega_8 + \omega_9 - \omega_{10f} - \omega_{11f} \\ \omega_{\mathrm{III}} &= \omega_{4f} - \omega_{5f} - \omega_6 - \omega_{7f} - 2\omega_{10f} - \omega_{11f}. \end{aligned} \tag{7.4}$$

On the other hand, for conditions sufficiently below the second explosion limit, the results presented in Chapter 6 suggest that the HO_2 steady-state assumption is a reasonable approximation (see Fig. 6.3), whereas that of H_2O_2 is not. Introducing a steady-state approximation for HO_2 reduces the four-step chemistry to

$$\begin{aligned} 3H_2 + O_2 &\overset{\mathrm{I}}{\rightleftharpoons} 2H_2O + 2H \\ H + H + M &\overset{\mathrm{II}}{\rightleftharpoons} H_2 + M \\ H_2 + O_2 &\overset{\mathrm{IV}}{\rightleftharpoons} H_2O_2, \end{aligned} \tag{7.5}$$

with corresponding rates

$$\begin{aligned} \omega_{\mathrm{I}} &= \omega_1 + \omega_{5f} + \omega_{12f} \\ \omega_{\mathrm{II}} &= \omega_{4f} + \omega_8 + \omega_9 - \omega_{10f} - \omega_{11f} \\ \omega_{\mathrm{IV}} &= \omega_{10f} + \omega_{11f} - \omega_{12f}. \end{aligned} \tag{7.6}$$

For evaluation of elementary rates, the concentrations of the steady-state species O and HO_2 are computed from (2.5) and (2.6), whereas that of OH is evaluated from (7.3), which appropriately accounts for H_2O_2 being out of steady state. As can be seen in the comparisons of Fig. 7.2, while a four-step mechanism including both HO_2 and H_2O_2 gives accurate predictions for ignition times regardless of the initial temperature, the two separate three-step descriptions derived by considering either H and HO_2 or H and H_2O_2 to be out of steady state give reasonable accuracy in their expected ranges of validity, but are much less accurate otherwise.

Note that for flames, where HO_2 and H_2O_2 may be additionally assumed to be in steady state, both three-step descriptions naturally reduce to the same two-step reduced mechanism

$$\begin{aligned} 3H_2 + O_2 &\overset{\mathrm{I}}{\rightleftharpoons} 2H_2O + 2H \\ H + H + M &\overset{\mathrm{II}}{\rightleftharpoons} H_2 + M \end{aligned} \tag{7.7}$$

with rates

$$\begin{aligned} \omega_{\mathrm{I}} &= \omega_1 + \omega_{5f} + \omega_{10f} + \omega_{11f} \\ \omega_{\mathrm{II}} &= \omega_{4f} + \omega_8 + \omega_9 - \omega_{10f} - \omega_{11f}, \end{aligned} \tag{7.8}$$

which was seen in Chapter 2 to provide sufficient accuracy for laminar burning velocities and strain rates of extinction. If there is interest in autoignition, however, then the two-step mechanism is not sufficient, and either HO_2 or H_2O_2 needs to be incorporated in the reduced chemistry as an additional chemical species out of steady state, the selection of one or the other depending on whether or not the temperature is above crossover. These two species are hardly ever simultaneously out of steady state, the only exception being ignition events at temperatures close to crossover, while for all other combustion situations the steady-state assumption is accurate for at least one of these two species. This observation motivates the investigation given below, in which a three-step mechanism is proposed as the minimum description able to encompass all combustion processes. Besides H atoms, a second species out of steady state, a surrogate intermediate X, is introduced to represent the role of either HO_2 or H_2O_2, depending on the local conditions.

7.2 A universal three-step description

In defining the properties of the surrogate X one may take into account the fact that, since in low-temperature autoignition the contribution of the H_2O_2 enthalpy is negligible for obtaining the correct induction time, as shown in Chapter 6, it is possible, with no adverse consequences, to select the enthalpy of formation of X to be equal to that of HO_2. On the other hand, given that the two molecules H_2O_2 and HO_2 have similar transport properties, predictions are quite independent of which diffusivity is employed for X, with that of HO_2 used in the computations below. The main difficulties in the development stem from the fact that the overall reactions for the consumption of HO_2 and H_2O_2 are different, with reaction III involving H-atom production, while reaction IV does not. Besides, since the expressions for the two sets of overall rates are different, a local criterion must be introduced to decide which one of the two sets of reactions is to be employed.

7.2.1 Modified reaction rates

In the development, let us consider the three overall steps

$$\begin{aligned}3H_2 + O_2 &\overset{\mathrm{I}}{\rightleftharpoons} 2H_2O + 2H\\ H + H + M &\overset{\mathrm{II}}{\rightleftharpoons} H_2 + M\\ H_2 + O_2 &\overset{\mathrm{III}}{\rightleftharpoons} X + H,\end{aligned} \tag{7.9}$$

which are exactly those for high-temperature ignition, with X=HO_2 and with overall rates given in (7.4)

$$\begin{aligned}\omega_{\mathrm{I}}^{+} &= \omega_1 + \omega_{5f} + \omega_{10f} + \omega_{11f}\\ \omega_{\mathrm{II}}^{+} &= \omega_{4f} + \omega_8 + \omega_9 - \omega_{10f} - \omega_{11f}\\ \omega_{\mathrm{III}}^{+} &= \omega_{4f} - \omega_{5f} - \omega_6 - \omega_{7f} - 2\omega_{10f} - \omega_{11f},\end{aligned} \tag{7.10}$$

to be corrected as in Chapter 3 in places where X (HO_2, in this case) is out of steady state.

As previously noted, an incorrect H-atom production rate would follow from using the above overall reaction III given in (7.9) with X=H_2O_2 for describing low-temperature ignition, because this reaction produces H atoms, while the overall reaction IV does not. This difficulty can be avoided by modifying the rate of II according to $\omega_{\mathrm{II}}^{-} = \omega_{\mathrm{II}} + \omega_{\mathrm{IV}}/2$, resulting finally in the overall rate expressions

$$\begin{aligned}\omega_{\mathrm{I}}^{-} &= \omega_{\mathrm{I}} = \omega_1 + \omega_{5f} + \omega_{12f}\\ \omega_{\mathrm{II}}^{-} &= \omega_{\mathrm{II}} + \omega_{\mathrm{IV}}/2 = \omega_{4f} + \omega_8 + \omega_9 - (\omega_{10f} + \omega_{11f} + \omega_{12f})/2\\ \omega_{\mathrm{III}}^{-} &= \omega_{\mathrm{IV}} = \omega_{10f} + \omega_{11f} - \omega_{12f},\end{aligned} \tag{7.11}$$

for describing low-temperature ignition with (7.9). The resulting rate expression for H is the same as that of (7.5) and (7.6). Clearly, the modification proposed introduces errors in H_2 production, but these errors are unimportant for ignition, because reactant consumption is negligible. As a result, the ignition times shown in Fig. 7.3, obtained with the three-step mechanism defined in (7.5) and (7.6), are indistinguishable from those obtained with the mechanism (7.9) with overall rates (7.11).

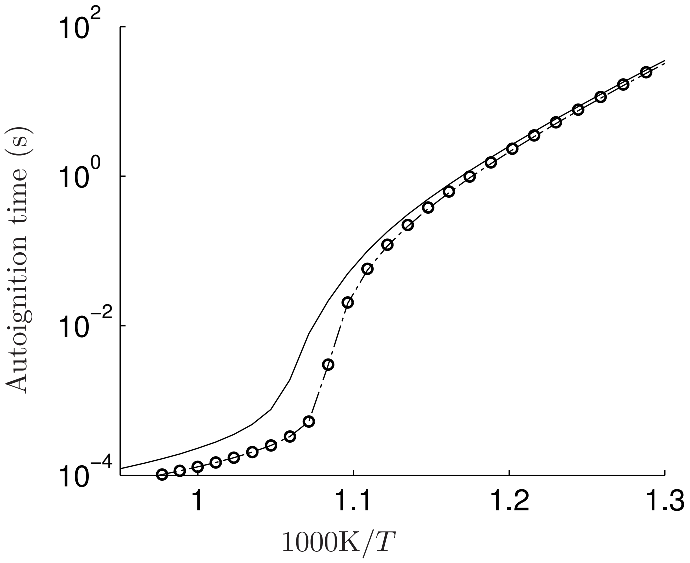

Figure 7.3: The variation of induction time with initial temperature for a stoichiometric mixture of H_2-air at atmospheric pressure as obtained with the detailed 21-step chemistry (solid curve), with the 3-step chemistry (7.5) including H_2O_2 with overall rates (7.6) (dot-dashed curve) and with the 3-step chemistry (7.9) with overall rates (7.11) (symbols).

Computations of flames with the three overall steps (7.9) give almost identical results when the two different set or rates (7.10) and (7.11) were employed because for flames the intermediate X is always in steady state, so that both mechanisms effectively reduce to the same two-step mechanism (7.7). This is illustrated in Fig. 7.4, which compares laminar burning rates obtained with the mechanism (7.9) for the two sets of rates with those obtained with detailed chemistry.

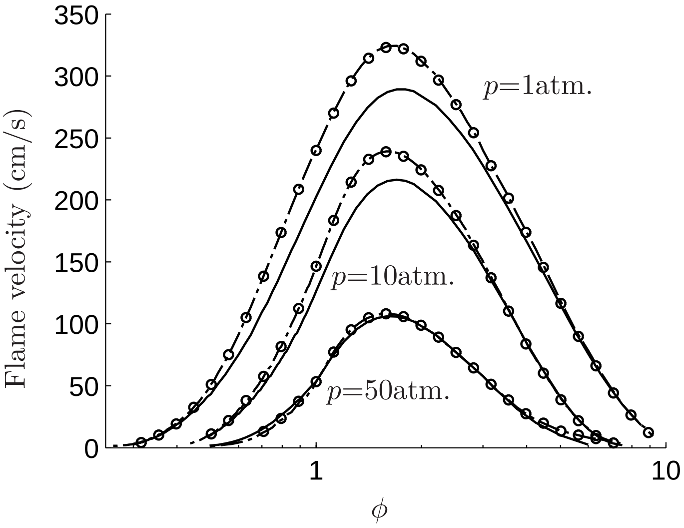

Figure 7.4: The variation with equivalence ratio of the laminar burning rate of hydrogen-air planar atmospheric deflagrations with initial temperature $T_u = 300$ K as obtained with the detailed 21-step chemistry (solid curves), with the 3-step chemistry (7.9) with overall rates $\omega^+_{\text{I,II,III}}$ (dashed-dotted curves) and with overall rates $\omega^-_{\text{I,II,III}}$ (symbols).

7.2.2 Criterion for selection of overall rates

The three overall steps displayed in (7.9) involve two chemical intermediates X and H. Two different sets of rates, given in (7.10) and (7.11), are found to apply depending on the combustion conditions. The results in Fig. 7.4 suggest that we may focus on autoignition only in seeking a criterion to decide which one of the two sets of overall rates applies, since the selection is inconsequential for flame descriptions. In general, one wishes to use (7.10) when high-temperature ignition is occurring and (7.11) when low-temperature ignition is occurring, but a computational criterion is needed to enforce the choice.

To identify places where the rates (7.11) apply, an obvious choice is to simply evaluate whether the local temperature is below crossover. This criterion is poor, however, in that it leads to severe disparities in resulting ignition times in neighboring points of the flow field as the conditions vary from slightly above to slightly below crossover (see the homogeneous ignition results given in Fig. 7.2). As an alternative, the selection criterion may take advantage of the observation, made in Chapter 6, that during low-temperature autoignition processes, H radicals are found in steady state after a short initial period of radical build up, whereas this species remains always out of steady state during high-temperature autoignition. A better criterion, then, may be to use (7.11) when H is in steady state.

To evaluate the steady state for H atoms, reactions important in low-temperature ignition are used to write the production rate

$$\omega_P = \omega_{6b} + \omega_{11f} + 2\omega_{12f} + 2\omega_{1f} \tag{7.12}$$

and the consumption rate

$$\omega_C = \omega_{4f}, \tag{7.13}$$

so that the net chemical production rate is found as the difference, $\dot{C}_{\mathrm{H}} = \omega_P - \omega_C$. The reaction rate ω_{12f} appearing in (7.12) may be evaluated as $k_{12f} C_{\mathrm{X}} C_{\mathrm{M}_{12}}$, since X is H_2O_2 under these conditions, whereas the HO_2 concentration, needed for computing ω_{11f}, is obtained from the steady-state expression

$$C_{\mathrm{HO}_2} = \frac{k_{11f} C_{\mathrm{H}_2} \alpha/(1-\alpha) + \sqrt{k_{11f}^2 C_{\mathrm{H}_2}^2 \alpha^2/(1-\alpha)^2 + 8 k_{10f} k_{6b} (2-\alpha)/(1-\alpha)}}{2 k_{10f}}, \tag{7.14}$$

with α defined in (6.4), which, unlike (6.5), includes the rate of the elementary reaction $11f$, for increased accuracy near crossover.

The condition $(\omega_P - \omega_C) \ll \omega_P$, satisfied in places where the H atom is in steady state, can be based on a small threshold value ε, such that if $(\omega_P - \omega_C)/\omega_P < \varepsilon$ the rates (7.11) should be used, whereas (7.10) applies otherwise. Using the elementary rates above to rewrite $(\omega_P - \omega_C)/\omega_P < \varepsilon$ leads to a condition on the concentration of H atoms,

$$C_{\mathrm{H}}[(1+\varepsilon) k_{4f} C_{\mathrm{M}_4} - 2k_{1f}] C_{\mathrm{O}_2} > k_{6b} C_{\mathrm{H}_2} C_{\mathrm{O}_2} + k_{11f} C_{\mathrm{H}_2} C_{\mathrm{HO}_2} + 2 k_{12f} C_{\mathrm{X}} C_{\mathrm{M}_{12}}, \tag{7.15}$$

so that the low-temperature rates (7.11) are to be used if (7.15) is satisfied. The results are essentially independent of the value of $\varepsilon \ll 1$ utilized to measure the steady-state condition, provided a sufficiently small value is employed.

Note that the above criterion requires two different conditions to be simultaneously satisfied, namely, that the temperature be below crossover, for $[(1+\varepsilon) k_{4f} C_{\mathrm{M}_4} - 2k_{1f}]$ to be positive with $\varepsilon \ll 1$, and that the H-atom concentration be above a given threshold value

$$C_{\mathrm{H}}^* = \frac{k_{6b} C_{\mathrm{H}_2} C_{\mathrm{O}_2} + k_{11f} C_{\mathrm{H}_2} C_{\mathrm{HO}_2} + 2 k_{12f} C_{\mathrm{X}} C_{\mathrm{M}_{12}}}{[(1+\varepsilon) k_{4f} C_{\mathrm{M}_4} - 2k_{1f}] C_{\mathrm{O}_2}}. \tag{7.16}$$

In autoignition below crossover, the initial H-atom concentration is zero, so that the high-temperature rates (7.10) automatically are selected initially by this criterion, and, in fact, they reproduce the correct H rates that apply initially, prior to H achieving a steady state. Below crossover, the computed H-atom concentration increases with time and reaches the criterion (7.15) for use of the low-temperature chemistry, which then is employed until temperatures above crossover are reached. Direct use of (7.15) with $\varepsilon \ll 1$ thus is both better and computationally simpler than using (7.11) all the time below crossover, although the predicted ignition times are only slightly different.

Figure 7.5 shows the evolution of the H radical during an autoignition process at an initial temperature of 800K, well below crossover at atmospheric pressure, as obtained using detailed chemistry, and the three-step chemistry with hypothesized species X, using both sets of rates. It is seen that there is a two-stage process, and during the first stage, the level of H is better predicted by the mechanism using the high-temperature set of rates, as stated above. This is because, for this period, HO_2 is key to the process, being a product of the only initiation step of importance: $H_2 + O_2 \rightarrow HO_2 + H$. The second stage, however, is not predicted by the high-temperature set of rates, which provoke an earlier ignition, by almost two orders of magnitude in this illustrative case. In that second stage, as indicated in Chapter 6, the process is better captured by putting H_2O_2 out of steady-state, and HO_2 may be assumed to be in steady state, so that it is essential to use the low-temperature set of rates during this second stage.

We thus introduce here a hybrid three-step chemistry description, making use of the three overall steps involving H_2, O_2, H_2O, H and X, with the overall rates $\omega^{+}_{\mathrm{I,\,II,\,III}}$ where (7.15) is not satisfied and $\omega^{-}_{\mathrm{I,\,II,\,III}}$ where it is. Figure 7.5 includes the H evolution as obtained with this hybrid description: it shows that after HO_2 has played its role in the induction chemistry, allowing the H consumption rate to nearly reach its production rate, a smooth transition to the low-temperature set of rates is obtained, thereby correcting the early autoignition calculated using only the high-temperature set of rates.

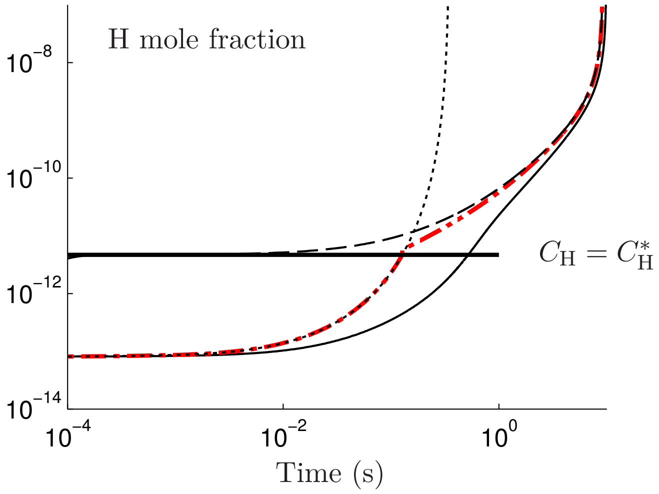

Figure 7.5: The evolution with time of H mole fraction, in a homogeneous H_2-air mixture with $\phi = 1$ and p=1atm, initially at 800K. The solid curve is the prediction using the detailed chemistry. The two sets of broken curves correspond to the three-step description using the rates $\omega^+_{\mathrm{I,\,II,\,III}}$ (dotted line), and $\omega^-_{\mathrm{I,\,II,\,III}}$ (dashed line). The dashed-dotted curve corresponds to the chemistry using both sets of rates, based on the criterion presented here, equivalent to switching when C_{H} reaches C^*_{H}, illustrated by the horizontal line.

Using such a criterion in choosing the appropriate set of rates for the three overall steps leads to continuous predictions of the variation of induction time with the initial temperature, with predictions being better than either one of the separate three-step descriptions. Figure 7.6 illustrates this point, showing the variation of the induction-time predictions with the detailed chemistry, with the two three-step descriptions (making exclusive use of either the high-temperature or the low-temperature sets of rates), and with the hybrid chemistry. The gray bars show the period of time during which the low-temperature set of rates are used, that is, the hybrid description switches from using the high-temperature set of rates to the low-temperature set of rates at the bottom of the gray area. At the top end of the gray area the hybrid description switches back to using the high-temperature set of rates. It is seen that for each homogeneous ignition history, the computation starts with the high-temperature set of rates and continues to use them until H nearly reaches a steady state, which occurs shortly before the ignition time predicted by this set of rates. The low-temperature set of rates is then used until ignition, occupying most of the ignition time at low temperatures, but then when the temperature reaches the crossover temperature, the criterion automatically switches the high-temperature set of rates back on. As expected, the lower the temperature is, the more use is made of the low-temperature set of rates, so that induction times are predicted with reasonable accuracy over the whole range of temperature, making use of the best of each set of rates.

7.3 Results

Figure 7.7 compares induction times of homogeneous mixtures as obtained with the detailed chemistry, the three-step hybrid description, and the four-step mechanism, for three different pressures. Comparison of induction times as obtained with the four-step mechanism and with the detailed chemistry show an outstanding agreement over the entire range of temperature, even in conditions close to crossover. The three-step hybrid also lead to excellent predictions of induction times, with small departures for conditions in the vicinity of crossover. The agreement obtained by this hybrid procedure should be sufficient for most computational purposes.

Predictions for laminar premixed flames are indistinguishable from those included in Fig. 7.4 for both

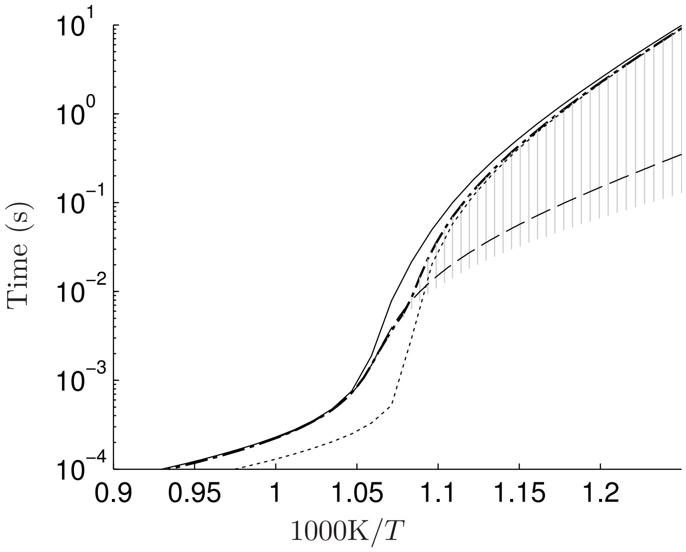

Figure 7.6: The variation with initial temperature of the ignition time at a pressure of 1 atm as obtained for a stoichiometric H_2-air mixture by numerical integration of the conservation equations with 21-step chemistry (solid curve), with the 3-step chemistry descriptions making use of the high-temperature set of rates (dahed line), and the low-temperature set of rates (dotted line), and with the hybrid description (dashed-dotted curve). The gray bars shade the region where use is made of the low-temperature set of rates in the hybrid scheme.

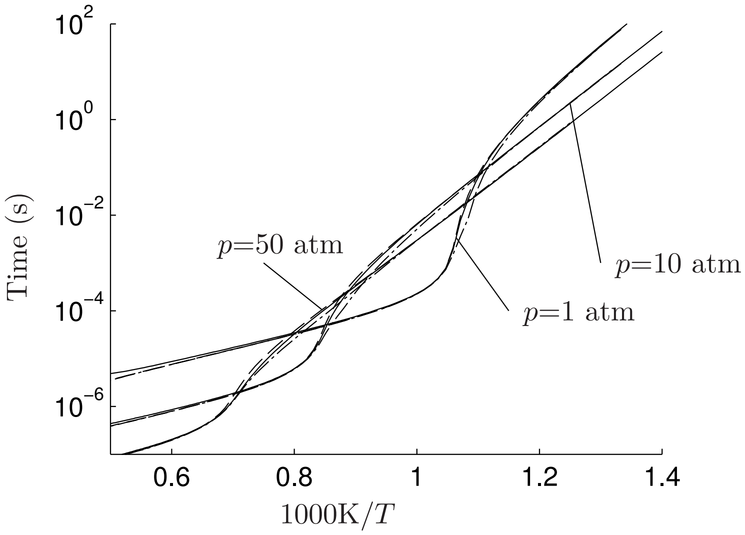

Figure 7.7: The variation with initial temperature of the ignition time for three different pressures as obtained for a stoichiometric H_2-air mixture by numerical integration of the conservation equations with 21-step chemistry (solid curves) with the 4-step chemistry (dashed curves), and with the 3-step chemistry, making use of separate set of rates for high and low temperature autoignition (dashed-dotted curves).

the 4-step and the 3-step hybrid descriptions, since they all reduce to the 2-step chemistry derived in Chapter 2. The steady-state assumptions for HO_2 and H_2O_2 have, in fact, no effect on the laminar flame speed obtained with the reduced chemistries. To improve these results, it would be necessary to reconsider the O and OH steady-state approximations. Trial computations with the hybrid scheme for more complex flows also suggest success.

7.4 Conclusions

In this chapter, we have been looking for "universal" reduced chemistries for H_2-air combustion, which may be seen as the ultimate objective of this dissertation. By universal, we mean reduced chemistries that may be used for computational purposes in all conditions of practical interest, including premixed and non-premixed combustion over the whole range of flammability, and also autoignition, whether the initial conditions place the system above or below the second explosion limit. Two options should be retained, which can find utility in different applications involving computation of flames and autoignition processes. For applications in which autoignition has to be reproduced with high fidelity, in conditions placing the system just below the second explosion limit, a four-step reduced chemistry, including H, HO_2 and H_2O_2 out of steady state should be retained, as being the only reduced description found to accurately describe autoignition in this regime. Two separate three-step reduced chemistry descriptions were then derived, having applicability for flames and autoignition in one of the two regimes (above or below the second explosion limit), but not qualifying as universal in the sense intended in this chapter. A hybrid three-step reduced chemistry, making use of the best of these two mechanism, was, however, proposed, yielding reasonable accuracy for most conditions, with small departures for induction times predictions at conditions very close to but below the second explosion limit. This three-step hybrid description was found to be accurate in premixed and non-premixed combustion, as well as in autoignition configurations, both above and below the second explosion limit.

CHAPTER 8

Conclusions and Future Prospects

8.1 Conclusions

Most numerical studies of hydrogen or syngas combustion aim at predicting temperatures, pressures and concentrations of major species as functions of space and time. For hydrogen oxidation, the detailed chemistry involves only 21 reversible elementary steps among 8 chemical species, resulting, in view of the two atom-conservation equations, in a mechanism which in principle should involve only 6 overall steps [4, 28], but even this mechanism often is too large to be handled in a convenient manner, neither computationally nor analytically, so that simplified kinetic descriptions are needed.

Historically, chemistry reduction methods based on steady-state approximations were derived and optimized for describing a single combustion process, e.g. structure and extinction of diffusion flames [10]. For general computational approaches, however, it is of interest to employ sufficiently accurate reduced chemistry that encompasses all of the combustion processes because it is not known a priori in exactly what manner the combustion will take place. Contributing to develop such multi-purpose reduced descriptions has been the main objective of the work presented here. Thus, rather than focussing on simplifying to the extreme the chemistry in order to reproduce accurately a specific combustion process, this dissertation derives reduced mechanisms valid for a wide range of combustion problems, so that the resulting descriptions can be used directly by research groups focussing on numerical simulations, reducing computational costs associated with the chemistry integration. A summary of the different mechanisms derived and their associated conditions of applicability is presented in Tab. 8.1.

Chapter 2 begins by identifying the minimum set of elementary reactions that is needed to describe all of the combustion processes that may be encountered in a reactive flow computation, namely, premixed and non-premixed flames, autoignition and detonations. The resulting 12-step short mechanism extends previous schemes [29, 30], developed for atmospheric combustion, to high-pressure conditions by accounting for additional chemical steps involving hydrogen peroxide [45]. Steady-state assumptions for intermediates are introduced in reducing the chemistry further. In particular, a two-step description with H as the only radical out of steady state is derived from the short chemistry. The difference with previously published two-step mechanisms lies in the overall rates, which incorporate contributions that become fundamental for describing high-pressure combustion and high-temperature equilibrium conditions. While the two-step mechanism provides sufficient accuracy for flames, it is however found to be inaccurate for the description of autoignition processes, including induction regions in detonations. A three-step mechanism, with HO_2 taken out of steady state is seen to improve accuracy somewhat, but not to a sufficiently satisfactory extent. Further improvements necessitate consideration of O and OH departures from steady state, especially under lean conditions. A careful analysis of the autoignition history for temperatures above crossover, given in Chapter 3 and Appendix A, suggests a modification to the reaction rates that improves significantly autoignition time predictions without giving up the simplification associated with the steady-state assumptions.

Reduced chemistry	reactive species	ignition processes		premixed flames	non-premixed flames	detonations	reference
H_2-air	H_2, O_2, H_2O,	$T < T_c$	$T > T_c$				
4-step	H, HO_2, H_2O_2	X	X	X	X	X	Chapter 7
3-step hybrid	H, X	X	X	X	X	X	Chapter 7
3-step	H, HO_2		X	X	X	X	Chapter 3
3-step	H, H_2O_2	X		X	X		Chapter 7
2-step	H			X	X		Chapter 2
Syngas	H_2, O_2, H_2O, CO,						
4-step	H, HO_2		X	X	X	X	Chapter 5

Table 8.1: A summary of the reduced chemistry descriptions for H_2-air combustion derived in this dissertation, with their applicability.

The modified three-step mechanism is thoroughly tested and is employed in Chapter 4 for the computation of supersonic, autoignition-stabilized, lifted flames. The simulation proves the efficiency of the proposed rate modification in improving predictions of flame lift-off heights requiring a correct description of the autoignition process responsible for the stabilization. As an additional outcome of the study, a method was proposed to analytically detect the domain where autoignition is occurring in turbulent reacting flows, to be used in computations jointly with methods tracking the autoignition front.

A four-step reduced mechanism, constructed from the three-step mechanism by addition of a CO-oxidation step, is proposed in Chapter 5 for the description of syngas combustion. The validations include comparisons of computed flame propagation velocities and ignition times with experimental data available in the literature, showing good agreement for all conditions tested. Even though the four-step chemistry was not validated under turbulent conditions, it is expected that the resulting accuracy would be comparable to that observed with the three-step mechanism in the hydrogen computations of Chapter 4.

Ignition below crossover is addressed in Chapter 6, which includes development of a two-step reduced mechanism and its application in analytical studies of homogeneous ignition histories. An explicit theoretical prediction is derived for the ignition time, giving results in excellent agreement with those of numerical simulations employing detailed chemistry.

Chapter 7 investigates extensions of the three-step mechanism derived in Chapter 3 to incorporate the low-temperature ignition developed in Chapter 6. A four-step mechanism with H, HO_2 and H_2O_2 out of steady state is thoroughly tested to give satisfactory results under all conditions. Similarities in the molecular diffusivity of HO_2 and H_2O_2 motivate consideration of a single representative radical for these two species, with their two overall steps being replaced by a single step, thereby reducing the description to a three-step reduced mechanism. The validated exercise attempted show promising results for different laminar test cases, although computations in turbulent environments are still needed for full validation.

8.2 Future prospects

Hydrogen is central in many “green” combustion applications because it is a clean energy carrier with water vapor as the main by-product that can be produced from any primary energy source, including renewable sources. New processes for low-cost hydrogen production, currently being developed, will facilitate the widespread utilization of hydrogen in the foreseable future, whether in fuel-cell applications or for gas-turbine and reciprocating-engine combustion.

Understanding and describing accurately autoignition processes will be crucial for future hydrogen use. The study presented in Chapters 3 and 6 may serve as a basis for further investigations. The next generation of liquid hydrogen fueled rocket engines (e.g. Vinci), under development, will be required to reignite up to five times, in order to facilitate satellite positioning. The extensive program of investigation of ignition processes under extreme conditions launched recently may benefit from fundamental knowledge of combustion kinetics, as the one developed here. The dynamics of the flame front in gas-turbine combustion chambers is believed to be largely influenced by autoignition processes. Autoignition-aided flashback can be also an important issue in that respect. Another source of concern is the safety of hydrogen tanks, usually pressurized to make up for the low density of hydrogen. A leak may lead to an accidental explosion. Understanding further the processes of autoignition both above and below the second explosion limit is therefore essential to minimize the risks associated with hydrogen storage in the growing hydrogen industry.

The gas-turbine industry shows an increasing interest in syngas combustion studies. There is a lot to be done in this field, as the subject is relatively recent. Studies of fuel-lean combustion at high pressures, accounting for preferential diffusion effects and water-vapor and carbon-dioxide radiation, are needed in order to guide designs of combustion chambers. Also, autoignition of this fuel in high-pressure conditions, typically below the second explosion limit, should be investigated by extending to CO-H_2 mixtures the work presented in Chapter 6.

A common drawback of reduced chemistry descriptions based on steady states assumptions, such as the ones presented in this dissertation, is that they are often found to overpredict equilibrium temperatures (e.g. in Chapter 4) because the enthalpies of formation of the steady-state species are not properly accounted for in the energy balance. This is particularly critical in detonation computations, for which the radical content at equilibrium is significant, so that the steady-state errors translate in nonnegligible overpredictions of heat release and, therefore, also overpredictions of propagation velocities. Inclusion of corrections to the enthalpy source terms, accounting for the heat of formation of the species assumed to be in steady-state, should be investigated in the future.

Clearly, much remains to be learnt concerning H_2 combustion. Studies of reduced kinetics as the one presented here can serve in that respect both to facilitate analytical developments and to reduce computational costs in numerical simulations.

References

[1] F. E. Marble, Flame theory and combustion technology, Journal of the Aeronautical Sciences 23 (5) (1956) 462–468.

[2] G. Millán, T. Von Kármán, Aerothermochemistry, United States Air Research and Development Command, INTA, 1958.

[3] F. A. Williams, Combustion Theory, 2nd edn., Benjamin Cummings, 1985.

[4] P. Saxena, F. A. Williams, Testing a small detailed chemical-kinetic mechanism for the combustion of hydrogen and carbon monoxide, Combustion and Flame 145 (1-2) (2006) 316–323.

[5] J. Buckmaster, P. Clavin, A. Liñán, M. Matalon, N. Peters, G. Sivashinsky, F. A. Williams, Combustion theory and modeling, Proceedings of the Combustion Institute 30 (1) (2005) 1–19.

[6] W. Bush, F. Fendell, Asymptotic analysis of laminar flame propagation for general Lewis numbers, Combustion Science and Technology 1 (6) (1970) 421–428.

[7] T. von Kármán, S. Penner, Selected Combustion Problems: Fundamentals and Aeronautical Application, Butterworths Scientific, London, 1954, Ch. Fundamental approach to laminar flame propagation.

[8] T. Von Kármán, The present status of the theory of laminar flame propagation, Symposium (International) on Combustion 6 (1) (1957) 1–11.

[9] J. Hirschfelder, C. Curtiss, D. Campbell, The theory of flame propagation. IV, The Journal of Physical Chemistry 57 (4) (1953) 403–414.

[10] A. Liñán, A. Crespo, An asymptotic analysis of unsteady diffusion flames for large activation energies, Combustion Science and Technology 14 (1) (1976) 95–117.

[11] K. Seshadri, N. Peters, F. A. Williams, Asymptotic analyses of stoichiometric and lean hydrogen-air flames, Combustion and Flame 96 (1994) 407–407.

[12] S. H. Sohrab, A. Liñán, F. A. Williams, Asymptotic theory of diffusion-flame extinction with radiant loss from the flame zone, Combustion Science and Technology, 27 (1982) 143–154.

[13] P. Libby, A. Liñán, F. A. Williams, Strained premixed laminar flames with nonunity Lewis numbers, Combustion Science and Technology, 34 (1983) 257–293.

[14] P. Clavin, Dynamic behavior of premixed flame fronts in laminar and turbulent flows, Progress in Energy and Combustion Science 11 (1) (1985) 1–59.

[15] S. Richard, O. Colin, O. Vermorel, A. Benkenida, C. Angelberger, D. Veynante, Towards large eddy simulation of combustion in spark ignition engines, Proceedings of the Combustion Institute 31 (2) (2007) 3059–3066.

[16] O. Vermorel, S. Richard, O. Colin, C. Angelberger, A. Benkenida, D. Veynante, Multi-cycle LES simulations of flow and combustion in a PFI SI 4-valve production engine, SAE Technical Paper (2007) 01–0151.

[17] G. Staffelbach, L. Gicquel, G. Boudier, T. Poinsot, Large eddy simulation of self excited azimuthal modes in annular combustors, Proceedings of the Combustion Institute 32 (2) (2009) 2909–2916.

[18] N. Peters, Turbulent combustion, Cambridge Univ. Press, London/New York, 2000.

[19] N. Peters, Multiscale combustion and turbulence, Proceedings of the Combustion Institute 32 (1) (2009) 1–25.

[20] A. Kolmogorov, The local structure of turbulence in incompressible viscous fluid for very large reynolds numbers, in: Doklady Akademii Nauk SSSR, Vol. 30, 1941, pp. 9–13.

[21] R. Courant, K. Friedrichs, H. Lewy, On the partial difference equations of mathematical physics, IBM Journal of Research and Development 11 (2) (1967) 215–234.

[22] S. Pope, Computationally efficient implementation of combustion chemistry using in situ adaptive tabulation, Combustion Theory and Modelling 1 (1) (1997) 41–63.

[23] O. Gicquel, N. Darabiha, D. Thévenin, Laminar premixed hydrogen/air counterflow flame simulations using flame prolongation of ILDM with differential diffusion, Proceedings of the Combustion Institute 28 (2) (2000) 1901 – 1908.

[24] J. V. Oijen, L. D. Goey, Modelling of premixed laminar flames using flamelet-generated manifolds, Combustion Science and Technology 161 (1) (2000) 113–137.

[25] U. Maas, S. Pope, Simplifying chemical kinetics: intrinsic low-dimensional manifolds in composition space, Combustion and Flame 88 (3-4) (1992) 239–264.

[26] S. Lam, D. Goussis, The CSP method for simplifying kinetics, International Journal of Chemical Kinetics 26 (4) (1994) 461–486.

[27] W. Jones, S. Rigopoulos, Rate-controlled constrained equilibrium: Formulation and application to nonpremixed laminar flames, Combustion and Flame 142 (3) (2005) 223–234.

[28] F. A. Williams, Detailed and reduced chemistry for hydrogen autoignition, Journal of Loss Prevention in the Process Industries 21 (2) (2008) 131–135.

[29] F. Mauss, N. Peters, B. Rogg, F. A. Williams, Reduced Kinetic Mechanisms for Premixed Hydrogen Flames, in: Reduced Kinetic Mechanisms for Applications in Combustion Systems, (N. Peters and B. Rogg, Eds.), Springer-Verlag, Heidelberg, 1993, pp. 29–43.

[30] D. Fernández-Galisteo, A. L. Sánchez, A. Liñán, F. A. Williams, One-step reduced kinetics for lean hydrogen–air deflagration, Combustion and Flame 156 (5) (2009) 985–996.

[31] D. Fernández-Galisteo, A. L. Sánchez, A. Liñán, F. A. Williams, The hydrogen–air burning rate near the lean flammability limit, Combustion Theory and Modelling 13 (4) (2009) 741–761.

[32] E. Fernández-Tarrazo, A. L. Sánchez, A. Liñán, F. A. Williams, The structure of lean hydrogen-air flame balls, Proceedings of the Combustion Institute 33 (1) (2011) 1203 – 1210.

[33] E. Fernández-Tarrazo, A. L. Sánchez, A. Liñán, F. A. Williams, Flammability conditions for ultra-lean hydrogen premixed combustion based on flame-ball analyses, International Journal of Hydrogen Energy In Press, doi:10.1016/j.ijhydene.2011.10.037.

[34] E. Gutheil, G. Balakrishnan, F. A. Williams, Structure and Extinction of Hydrogen-Air Diffusion Flames, in: Reduced Kinetic Mechanisms for Applications in Combustion Systems, (N. Peters and B. Rogg, Eds.), Springer-Verlag, Heidelberg, 1993, pp. 177–195.

[35] G. Balakrishnan, M. Smooke, F. A. Williams, A numerical investigation of extinction and ignition limits in laminar nonpremixed counterflowing hydrogen-air streams for both elementary and reduced chemistry, Combustion and Flame 102 (3) (1995) 329–340.

[36] A. Ruiz, L. Selle, B. Cuenot, T. Poinsot, Stabilization of a supercritical hydrogen/oxygen flame behind a splitter plate, in: Highly Resolved Experimental and Numerical Diagnostics for Turbulent Combustion Conference, Rouen, 2011.

[37] G. Del Álamo, F. A. Williams, A. L. Sánchez, Hydrogen-oxygen induction times above crossover temperatures, Combustion Science and Technology 176 (10) (2004) 1599–1626.

[38] T. Lu, C. Yoo, J. Chen, C. Law, Three-dimensional direct numerical simulation of a turbulent lifted hydrogen jet flame in heated coflow: a chemical explosive mode analysis, Journal of Fluid Mechanics 652 (1) (2010) 45–64.

[39] Y. Mizobuchi, S. Tachibana, J. Shinio, S. Ogawa, T. Takeno, A numerical analysis of the structure of a turbulent hydrogen jet lifted flame, Proceedings of the Combustion Institute 29 (2) (2002) 2009–2015.

[40] E. Mastorakos, Ignition of turbulent non-premixed flames, Progress in Energy and Combustion Science 35 (1) (2009) 57–97.

[41] H. Yamashita, M. Shimada, T. Takeno, A numerical study on flame stability at the transition point of jet diffusion flames, Symposium (International) on Combustion 26 (1) (1996) 27–34.

[42] T. Echekki, J. Chen, Direct numerical simulation of autoignition in non-homogeneous hydrogen-air mixtures, Combustion and Flame 134 (3) (2003) 169–191.

[43] P. Domingo, L. Vervisch, D. Veynante, Large-eddy simulation of a lifted methane jet flame in a vitiated coflow, Combustion and Flame 152 (3) (2008) 415–432.

[44] R. G. Gilbert, K. Luther, J. Troe, Theory of thermal unimolecular reactions in the fall-off range. II. Weak collisions rate constants, Berichte der Bunsengesellschaft für physikalische Chemie 87 (1983) 169–177.

[45] C. Treviño, Ignition phenomena in H_2-O_2 mixtures, Progress in Astronautics and Aeronautics, AIAA 131 (1991) 19–43.

[46] Version 2.0.7, Rotexo-Softpredict-Cosilab Gmbh & Co. KG, http://www.SoftPredict.com (2007).

[47] A. L. Sánchez, A. Liñán, F. A. Williams, Chain-branching explosions in mixing layers, SIAM Journal on Applied Mathematics 59 (4) (1999) 1335–1355.

[48] M. Baum, T. J. Poinsot, D. C. Haworth, N. Darabiha, Direct numerical simulation of $H_2/O_2/N_2$ flames with complex chemistry in two-dimensional turbulent flows, Journal of Fluid Mechanics 281 (1994) 1–32.

[49] R. Knikker, A. Dauptain, B. Cuenot, T. Poinsot, Comparison of computational methodologies for ignition of diffusion layers, Combustion Science and Technology 175 (10) (2003) 1783–1806.

[50] C. Treviño, F. Solorio, Asymptotic analysis of the high-temperature ignition of $CO/H_2/O_2$ mixtures, Combustion and Flame 86 (3) (1991) 285–295.

[51] P. Boivin, C. Jiménez, A. L. Sánchez, F. A. Williams, An explicit reduced mechanism for H_2-air combustion, Proceedings of the Combustion Institute 33 (1) (2011) 517–523.

[52] T. Cheng, J. Wehrmeyer, R. Pitz, O. Jarrett Jr, G. Northam, Raman measurement of mixing and finite-rate chemistry in a supersonic hydrogen-air diffusion flame, Combustion and Flame 99 (1) (1994) 157–173.

[53] T. Schönfeld, M. Rudgyard, Steady and unsteady flows simulations using the hybrid flow solver AVBP, AIAA Journal 37 (11) (1999) 1378–1385.

[54] A. Dauptain, B. Cuenot, L. Gicquel, Large eddy simulation of stable supersonic jet impinging on flat plate, AIAA Journal 48 (2010) 2325–2338.

[55] A. Cook, W. Cabot, Hyperviscosity for shock-turbulence interactions, Journal of Computational Physics 203 (2) (2005) 379–385.

[56] H. Möbus, P. Gerlinger, D. Brüggemann, Comparison of Eulerian and Lagrangian Monte Carlo PDF methods for turbulent diffusion flames, Combustion and Flame 124 (3) (2001) 519–534.

[57] P. Gerlinger, K. Nold, M. Aigner, Influence of reaction mechanisms, grid spacing, and inflow conditions on the numerical simulation of lifted supersonic flames, International Journal for Numerical Methods in Fluids 62 (12) (2010) 1357–1380.

[58] J. Izard, A. Mura, Stabilization of non-premixed flames in supersonic reactive flows, Comptes Rendus Mécanique 337 (6-7) (2009) 362–372.

[59] Z. Gao, C. Lee, A flamelet model for turbulent diffusion combustion in supersonic flow, Science China Technological Sciences 53 (12) (2010) 3379–3388.

[60] R. Baurle, S. Girimaji, Assumed PDF turbulence-chemistry closure with temperature-composition correlations, Combustion and Flame 134 (1-2) (2003) 131–148.

[61] H. Möbus, P. Gerlinger, D. Brüggemann, Scalar and joint scalar-velocity-frequency Monte Carlo PDF simulation of supersonic combustion, Combustion and Flame 132 (1-2) (2003) 3–24.

[62] W. Jones, S. Navarro-Martínez, Large eddy simulation of autoignition with a subgrid probability density function method, Combustion and Flame 150 (3) (2007) 170–187.

[63] Z. Luo, C. Yoo, E. Richardson, J. Chen, C. Law, T. Lu, Chemical explosive mode analysis for a turbulent lifted ethylene jet flame in highly-heated coflow, Combustion and Flame In Press, doi:0.1016/j.combustflame.2011.05.023.

[64] P. Boivin, A. Dauptain, C. Jiménez, B. Cuenot, Simulation of a supersonic hydrogen-air autoignition-stabilized flame using reduced chemistry, submitted to Combustion and Flame.

[65] D. Kalitan, J. Mertens, M. Crofton, E. Petersen, Ignition and oxidation of lean CO/H_2 fuel blends in air, Journal of Propulsion and Power 23 (6) (2007) 1291–1303.

[66] H. Sun, S. Yang, G. Jomaas, C. Law, High-pressure laminar flame speeds and kinetic modeling of carbon monoxide/hydrogen combustion, Proceedings of the Combustion Institute 31 (1) (2007) 439–446.

[67] I. C. McLean, D. B. Smith, S. C. Taylor, The use of carbon monoxide/hydrogen burning velocities to examine the rate of the CO+OH reaction, Symposium (International) on Combustion 25 (1) (1994) 749 – 757.

[68] C. Dong, Q. Zhou, Q. Zhao, Y. Zhang, T. Xu, S. Hui, Experimental study on the laminar flame speed of hydrogen/carbon monoxide/air mixtures, Fuel 88 (10) (2009) 1858–1863.

[69] J. Natarajan, Y. Kochar, T. Lieuwen, J. Seitzman, Pressure and preheat dependence of laminar flame speeds of $H_2/CO/CO_2/O_2/He$ mixtures, Proceedings of the Combustion Institute 32 (1) (2009) 1261–1268.

[70] J. Natarajan, T. Lieuwen, J. Seitzman, Laminar flame speeds of H_2/CO mixtures: Effect of CO_2 dilution, preheat temperature, and pressure, Combustion and Flame 151 (1-2) (2007) 104–119.

[71] M. Chaos, F. Dryer, Syngas combustion kinetics and applications, Combustion Science and Technology 180 (6) (2008) 1053–1096.

[72] S. Medvedev, G. Agafonov, S. Khomik, B. Gelfand, Ignition delay in hydrogen-air and syngas-air mixtures: Experimental data interpretation via flame propagation, Combustion and Flame 157 (7) (2010) 1436–1438.

[73] D. Cavaliere, M. Joannon, P. Sabia, M. Sirignano, A. D'Anna, A comprehensive kinetic modeling of ignition of syngas–air mixtures at low temperatures and high pressures, Combustion Science and Technology 182 (4) (2010) 692–701.

[74] E. Petersen, D. Kalitan, A. Barrett, S. Reehal, J. Mertens, D. Beerer, R. Hack, V. McDonell, New syngas/air ignition data at lower temperature and elevated pressure and comparison to current kinetics models, Combustion and Flame 149 (1-2) (2007) 244–247.

[75] P. Boivin, C. Jiménez, A. L. Sánchez, F. A. Williams, A four-step reduced mechanism for syngas combustion, Combustion and Flame 158 (6) (2011) 1059 – 1063.

[76] G. Schott, J. Kinsey, Kinetic studies of hydroxyl radicals in shock waves. II. induction times in the hydrogen-oxygen reaction, The Journal of Chemical Physics 29 (1958) 1177–1182.

[77] R. Kushida, The reaction of hydrogen and oxygen at high temperature, National Engineering Science Company, Air Force Contract No. AF3396160-8606.

[78] T. Asaba, W. Gardiner, R. Stubbeman, Ignition delays in H_2–O_2–Ar mixtures, Proceedings of the Combustion Institute 10 (1965) 295–302.

[79] R. Craig, A shock tube study of the ignition delay of hydrogen-air mixtures near the second explosion limit, Tech. rep., DTIC Document, Report AFAPL-TR-66-74 (1966).

[80] F. Just, F. Schmalz, Measurements of ignition delays of hydrogen air mixtures under simulated conditions of supersonic combustion chambers, Tech. rep., AGARD CP No. 34, Part 2, Paper 19 (1968).

[81] F. L. Dryer, M. Chaos, Ignition of syngas/air and hydrogen/air mixtures at low temperatures and high pressures: Experimental data interpretation and kinetic modeling implications, Combustion and Flame 152 (1-2) (2008) 293 – 299.

[82] S. P. Medvedev, G. L. Agafonov, S. V. Khomik, B. E. Gelfand, Ignition delay in hydrogen–air and syngas–air mixtures: Experimental data interpretation via flame propagation, Combustion and Flame 157 (7) (2010) 1436 – 1438.

[83] B. Varatharajan, F. A. Williams, Ignition times in the theory of branched-chain thermal explosions, Combustion and Flame 121 (3) (2000) 551–554.

[84] P. Boivin, A. L. Sánchez, F. A. Williams, Explicit analytic prediction for hydrogen-oxygen ignition times at temperatures below crossover, Combustion and Flame In Press, doi:10.1016/j.combustflame.2011.08.019.

APPENDIX A

Analytic expression for ignition times above crossover

This appendix presents the derivation of an explicit expression for the induction time of hydrogen-oxygen mixtures for conditions above the second explosion limit.

A.1 Radical growth above crossover

It was shown in chapter 3 that autoignition processes for systems initially at temperatures above crossover can be described with reactant consumption and heat release neglected by integrating the linearized form of the time-dependent conservation equations for the radicals O, OH and H

$$\frac{d}{dt}\bar{C} = \mathbf{A}.\bar{C} + \bar{\epsilon} \quad \text{where} \quad \bar{C} = \begin{bmatrix} C_{\mathrm{H}} \\ C_{\mathrm{O}} \\ C_{\mathrm{OH}} \end{bmatrix}, \tag{A.1}$$

with initial condition $\bar{C} = 0$ at $t = 0$. The components of the 3x3 matrix

$$\mathbf{A} = \begin{bmatrix} -(k_{1f}C_{\mathrm{O}_2} + k_{4f}C_{\mathrm{O}_2}C_{\mathrm{M}_4}) & k_{2f}C_{\mathrm{H}_2} & k_{3f}C_{\mathrm{H}_2} \\ k_{1f}C_{\mathrm{O}_2} & -k_{2f}C_{\mathrm{H}_2} & 0 \\ k_{1f}C_{\mathrm{O}_2} & k_{2f}C_{\mathrm{H}_2} & -k_{3f}C_{\mathrm{H}_2} \end{bmatrix} \tag{A.2}$$

represent the reciprocal of the characteristic times associated with reactions 1–4. The constant

$$\bar{\epsilon} = \begin{bmatrix} k_{6b}C_{\mathrm{O}_2}C_{\mathrm{H}_2} \\ 0 \\ 0 \end{bmatrix} \tag{A.3}$$

corresponds to the initial production of radicals through the initiation step $6b$, essential to trigger the branched-chain explosion since all reaction rates for $1f$, $2f$, $3f$ and $4f$ are initially zero.

The solution of this linear system can be expressed as

$$\bar{C} = a_1\bar{V}_1e^{\lambda_1 t} + a_2\bar{V}_2e^{\lambda_2 t} + a_3\bar{V}_3e^{\lambda_3 t} + \bar{C}_0, \tag{A.4}$$

where $\bar{V}_i$ are the dimensionless eigenvectors associated with the eigenvalues λ_i of matrix $\mathbf{A}$, a_i are constants of integration with dimensions of a concentration, determined by imposing a zero initial radical concentration

$$\bar{C} = a_1\bar{V}_1 + a_2\bar{V}_2 + a_3\bar{V}_3 + \bar{C}_0 = 0, \tag{A.5}$$

and

$$\bar{C}_0 = -\frac{k_{6b}C_{\mathrm{H}_2}}{2k_{1f} - k_{4f}C_{\mathrm{M}_4}} \begin{bmatrix} 1 \\ \frac{k_{1f}C_{\mathrm{O}_2}}{k_{2f}C_{\mathrm{H}_2}} \\ \frac{2k_{1f}C_{\mathrm{O}_2}}{k_{3f}C_{\mathrm{H}_2}} \end{bmatrix} \tag{A.6}$$

is the particular solution obtained from $\mathbf{A} \cdot \bar{C}_0 + \bar{\epsilon} = 0$. The eigenvalues λ_i are determined as the solution of the characteristic equation

$$\det(\lambda \mathbf{I} - \mathbf{A}) = \lambda^3 + l_2\lambda^2 + l_1\lambda - l_0 = 0, \tag{A.7}$$

where

$$\begin{aligned} l_2 &= k_{1f}C_{\mathrm{O}_2} + k_{2f}C_{\mathrm{H}_2} + k_{3f}C_{\mathrm{H}_2} + k_{4f}C_{\mathrm{O}_2}C_{\mathrm{M}_4}, \\ l_1 &= k_{2f}k_{3f}C^2_{\mathrm{H}_2} + (k_{2f} + k_{3f})k_{4f}C_{\mathrm{H}_2}C_{\mathrm{O}_2}C_{\mathrm{M}_4}, \\ l_0 &= (2k_{1f}C_{\mathrm{O}_2} - k_{4f}C_{\mathrm{O}_2}C_{\mathrm{M}_4})k_{2f}k_{3f}C^2_{\mathrm{H}_2}. \end{aligned} \tag{A.8}$$

It should be remarked that $l_0 = 0$ at crossover, where $2k_{1f}C_{\mathrm{O}_2} = k_{4f}C_{\mathrm{O}_2}C_{\mathrm{M}_4}$, making the matrix singular. On the other hand, the eigenvector $\bar{V}_i$ associated with λ_i for matrix $\mathbf{A}$ can be normalized according to

$$\bar{V}_i = \begin{bmatrix} 1 \\ f(\lambda_i) \\ g(\lambda_i) \end{bmatrix} \tag{A.9}$$

where

$$f(\lambda_i) = \frac{k_{1f}C_{\mathrm{O}_2}}{k_{2f}C_{\mathrm{H}_2} + \lambda_i} \tag{A.10}$$

$$g(\lambda_i) = \frac{k_{1f}C_{\mathrm{O}_2}(2k_{2f}C_{\mathrm{H}_2} + \lambda_i)}{(k_{2f}C_{\mathrm{H}_2} + \lambda_i)(k_{3f}C_{\mathrm{H}_2} + \lambda_i)} \tag{A.11}$$

are functions of the corresponding eigenvalue λ_i. It is easy to prove that these two functions tend to zero when the mixture becomes sufficiently rich, for which the radical pool is dominated entirely by the H radical, while the concentrations of O and OH are negligibly small. This explains the accuracy of the predicted autoignition times of fuel-rich mixtures obtained in the introduction of Chapter 3 with the uncorrected three-step reduced chemistry, which assumes steady states for both O and OH.

A.2 An explicit analytic expression for the induction time.

Above crossover, $\mathbf{A}$ has three real eigenvalues, λ_1, λ_2 and λ_3, only one of which is positive, λ_1. This is seen in Fig. A.1, which shows the variation with the equivalence ratio ϕ of the three eigenvalues, λ_1, $-\lambda_2$ and $-\lambda_3$ at atmospheric pressure for a temperature of 1100K. The figure also shows the accompanying variation of the main characteristic chain-branching times appearing in $\mathbf{A}$. As can be seen, λ_2 and λ_3 are both negative, and much larger in norm than λ_1, implying that, after a very short time, the solution for the radical pool growth (A.4) reduces to

$$\bar{C} = a_1\bar{V}_1 e^{\lambda_1 t} + \bar{C}_0 \tag{A.12}$$

Expressions for a_1 and λ_1 are needed in (A.12) to close the description of the radical growth history. The value of a_1 follows from (A.5). After elimination of a_2 and a_3 by linear combination of the three equations, the expression

$$a_1 = \frac{k_{6b}C_{\mathrm{H}_2}}{2k_{1f} - k_{4f}C_{\mathrm{M}_4}} \frac{\lambda_2\lambda_3(k_{2f}C_{\mathrm{H}_2} + \lambda_1)(k_{3f}C_{\mathrm{H}_2} + \lambda_1)}{k_{2f}k_{3f}C^2_{\mathrm{H}_2}(\lambda_1^2 + \lambda_2\lambda_3 - \lambda_1(\lambda_2 + \lambda_3))} \tag{A.13}$$

is found, which can be rewritten as

$$a_1 = \frac{k_{6b}C_{\mathrm{H}_2}C_{\mathrm{O}_2}(k_{2f}C_{\mathrm{H}_2} + \lambda_1)(k_{3f}C_{\mathrm{H}_2} + \lambda_1)}{2\lambda_1^3 + l_2\lambda_1^2 + l_0}. \tag{A.14}$$

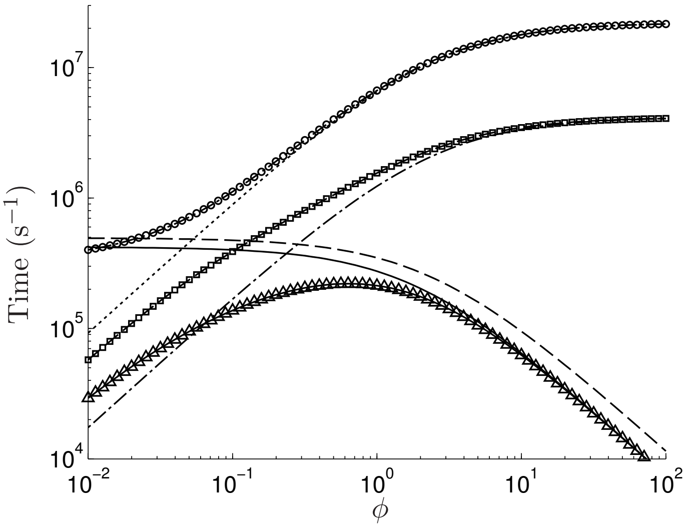

Figure A.1: The variation with equivalence ratio of the the three eigenvalues λ_1 (triangles), $-\lambda_2$ (squares), and $-\lambda_3$ (circles) and of the reaction rates $(2k_{1f} - k_{4f}C_{M_4})C_{O_2}$ (solid curve), $2k_{1f}C_{O_2}$ (dashed curve), $k_{2f}C_{H_2}$ (dot-dashed curve), and $k_{3f}C_{H_2}$ (dotted curve) as obtained for p =1 atm, T = 1100K.

in terms of the unknown branching rate λ_1.

As previously mentioned, λ_1 can be determined as the root of the cubic polynomial (A.7). The solution leads to a fairly complicated expression [37] that can be however simplified by noting that l_2 is always much greater than λ_1, so that in computing this eigenvalue the cubic term in (A.7) can be neglected in the first approximation. This is illustrated in Fig. A.1, which shows that for any mixture fraction, λ_1 is much smaller than at least one of the rate terms $k_{1f}C_{O_2}$, $k_{2f}C_{H_2}$ and $k_{3f}C_{H_2}$ that appear in the expression for l_2. The resulting quadratic equation for λ can be solved explicitly to give

$$\lambda_1 \approx \lambda = \frac{\sqrt{l_1^2 + 4l_0l_2} - l_1}{2l_2}. \tag{A.15}$$

The approximation for the eigenvalue $\lambda_1 \approx \lambda$ is validated in Figs. A.2 and A.3, where the analytical expression given above is compared to the numerical solution of (A.7). The agreement obtained between

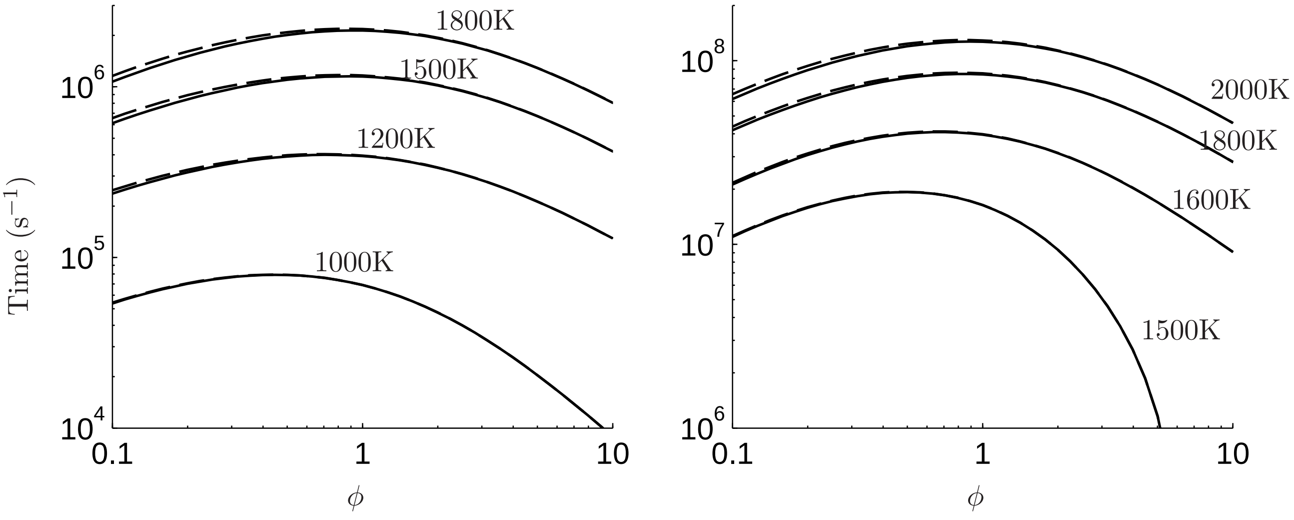

(a) p =1 atm.

(b) p =50 atm.

Figure A.2: The variation with the equivalence ratio of λ_1, obtained numerically (solid lines), and λ as given by (A.15) (dashed lines), for different pressures and temperatures.

the exact and approximate values is excellent for all of the conditions tested, both for atmospheric and elevated pressure.

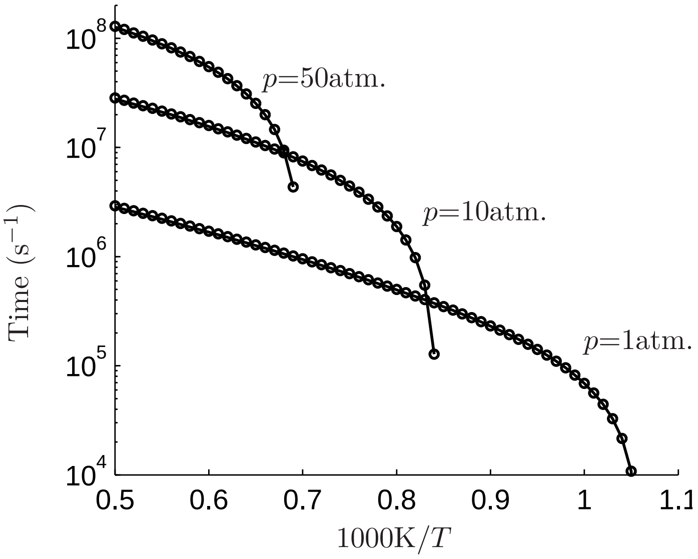

Figure A.3: The variation with the temperature of λ_1, obtained numerically (solid lines), and λ as given by (A.15) (symbols), for a stoichiometric mixture of H_2 and air at different pressures.

The exponential solution for the radical growth, given in (A.12) describes an infinite monotonous increase of the radical pool with increasing time. This is a major difference from low-temperature autoignition, which was shown in chapter 6 to be characterized by a thermal runaway at a finite time, providing a precise definition of the ignition time. For autoignition above the second explosion limit, however, in the simplified description given above the ignition time needs to be associated with a finite level of a selected progress variable. We choose here to identify ignition as the instant for which the H_2O concentration reaches a value equal to the initial concentration of the limiting reactant, i.e., $t = t_i$ when $C_{\mathrm{H_2O}} = \min(C_{\mathrm{O_2}}/2, C_{\mathrm{H_2}})$.

For the ignition chemistry considered here, water vapor is produced by reaction $3f$ according to

$$\frac{dC_{\mathrm{H_2O}}}{dt} = k_{3f} C_{\mathrm{H_2}} C_{\mathrm{OH}}, \tag{A.16}$$

which, after having replaced C_{OH} by the third component of $\bar{C}$, given in (A.12), reads

$$\frac{dC_{\mathrm{H_2O}}}{dt} = k_{3f} C_{\mathrm{H_2}} \Big(a_1 g(\lambda_1) e^{\lambda_1 t} - \frac{2k_{1f} C_{\mathrm{O_2}}}{k_{3f} C_{\mathrm{H_2}}} \frac{k_{6b} C_{\mathrm{H_2}}}{2k_{1f} - k_{4f} C_{\mathrm{M_4}}} \Big). \tag{A.17}$$

Integration with initial condition $C_{\mathrm{H_2O}}(0) = 0$ yields, for large times

$$C_{\mathrm{H_2O}} = k_{3f} C_{\mathrm{H_2}} a_1 g(\lambda_1) e^{\lambda_1 t} / \lambda_1, \tag{A.18}$$

which can be used to give

$$t_i = \frac{1}{\lambda_1} \ln \Big(\frac{\min(C_{\mathrm{O_2}}/2, C_{\mathrm{H_2}}) \lambda_1}{k_{3f} C_{\mathrm{H_2}} a_1 g(\lambda_1)} \Big) \tag{A.19}$$

as the induction time, for which $C_{\mathrm{H_2O}} = \min(C_{\mathrm{O_2}}/2, C_{\mathrm{H_2}})$.

A.3 Validation of the analytic formula for the induction time

The comparison of the induction time obtained analytically in (A.19), and the integration of the 21-step detailed chemistry is presented in Figs. A.4 and A.5 for different conditions of pressure, temperature

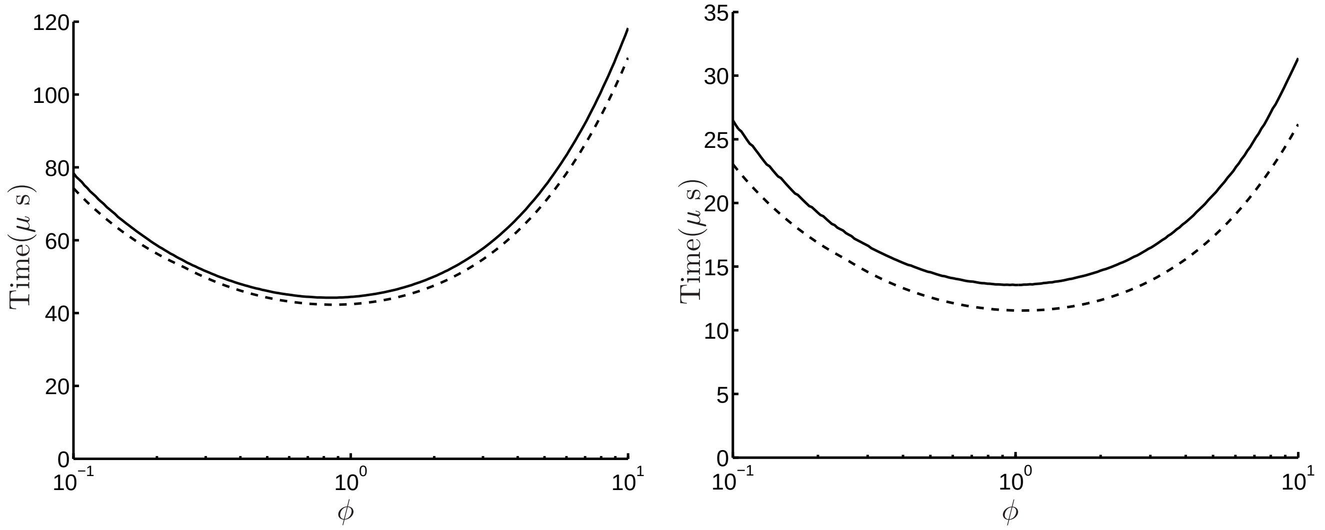

(a) T=1200K, p=1atm.

(b) T=1500K, p=1atm.

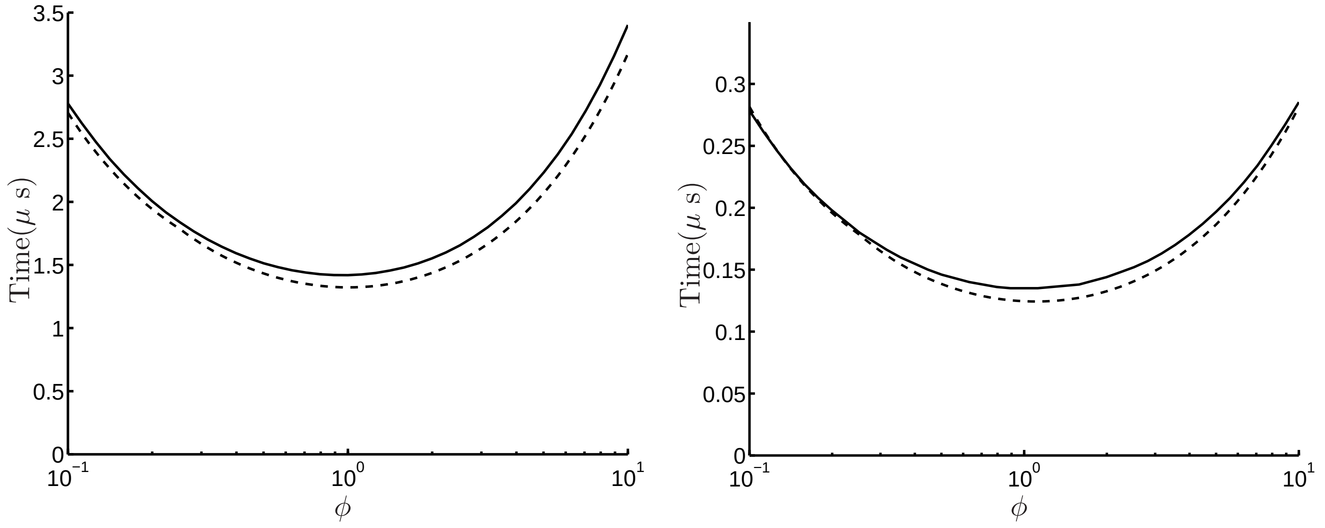

(c) T=1500K, p=10atm.

(d) T=1800K, p=50atm.

Figure A.4: The variation with equivalence ratio of the ignition time as obtained by numerical integration of the conservation equations with 21-step chemistry (solid curves) and by evaluation of (A.19) (dashed curves) for H_2-air mixtures at different conditions of pressure and initial temperature.

and composition. The results show that a very good agreement exists between the numerical and analytic predictions, especially at high temperature. Note that the results in Fig. A.4 correspond to conditions sufficiently far from crossover. As illustrated in Fig. A.5, the accuracy of the analytic prediction degrades as the initial temperature approaches the crossover value, a consequence of the assumption of negligible heat release used in deriving (A.19). To show more clearly the origin of the departures, dashed lines were included in the plots of Fig A.5 to represent results of detailed-chemistry integrations obtained with the additional assumption of constant temperature. As can be seen, the results lie very close to the analytic predictions, confirming that for near-crossover conditions the reaction-rate enhancement associated with the chemical heat release can no longer be neglected in deriving an expression for the induction time. As shown by [45], the modified problem accounting for heat release requires a more elaborate analysis based on the large activation energy of the branching reactions.

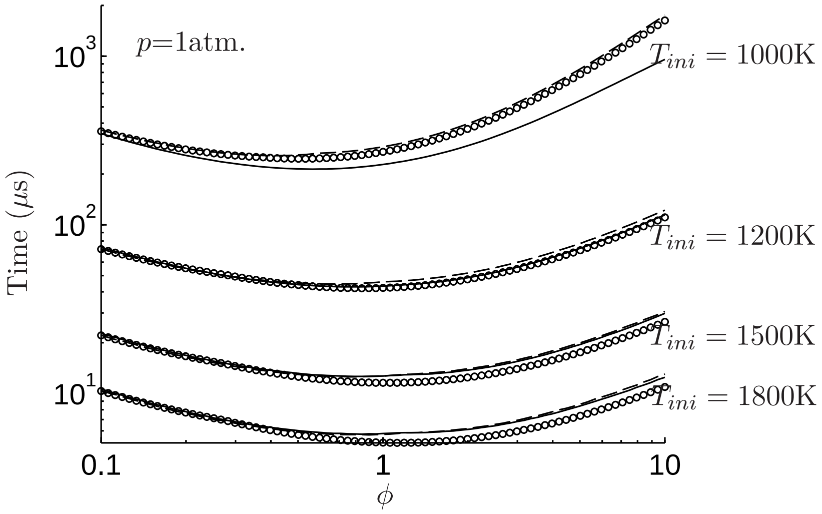

Figure A.5: Induction times obtained with the numerical integration of the full detailed chemistry (plain line), numerical integration of the reactions, neglecting the temperature variation (dashed line), and the induction time given by (A.19) (symbols).